A Numerical Analysis of Electromagnetic Scattering from Two-Dimensional Edge Terminations

B.E. Gray, A.K. Dominek and N. Wang

The Ohio State University

ElectroScience Laboratory

Department of Electrical Engineering
Columbus, Ohio   43212

NOTICES

When Government drawings, specifications, or other data are used for any purpose other than in connection with a definitely related Government procurement operation, the United States Government thereby incurs no responsibility nor any obligation whatsoever, and the fact that the Government may have formulated, furnished, or in any way supplied the said drawings, specifications, or other data, is not to be regarded by implication or otherwise as in any manner licensing the holder or any other person or corporation, or conveying any rights or permission to manufacture, use, or sell any patented invention that may in any way be related thereto.

.

50272-101

REPORT DOCUMENTATION PAGE	1. REPORT NO.	2.	3. Recipient's Accession No.

4. Title and Subtitle	5. Report Date
A Numerical Analysis of Electromagnetic Scattering	December 1995
from Two-Dimensional Edge Terminations	6.

7. Author(s)	8. Performing Org. Rept. No.
B.E. Gray, A.K. Dominek and N. Wang	731507-2

9. Performing Organization Name and Address	10. Project/Task/Work Unit No.
The Ohio State University	
ElectroScience Laboratory	11. Contract(C) or Grant(G) No.
1320 Kinnear Road	(C)
Columbus, OH 43212	(G) NAG3-1785

12. Sponsoring Organization Name and Address	13. Report Type/Period Covered
NASA Lewis Research Center	Technical Report
21000 Brookpark Rd.	14.
Cleveland, OH 44135	

15. Supplementary Notes

16. Abstract (Limit: 200 words)

Several techniques that influence the low frequency scattering from penetrable edge terminations are evaluated using a hybrid finite element and boundary element method code. The edge terminations consist of a dielectric skin forming an exterior shape with an internal conducting bulkhead. Some of the techniques considered are bulkhead shaping, internal material loading, placement of resistive cards, and the placement of lossy dielectric material rods. The intent of the various treatments is to find a combination or combinations that influence(s) the backscattered field to acceptable levels over a range of frequencies for both transverse magnetic and transverse electric polarizations.

17. Document Analysis a. Descriptors

    MODELING

    RCS

    SCATTERING

b. Identifiers/Open-Ended Terms

c. COSATI Field/Group

18. Availability Statement	19. Security Class (This Report)	21. No. of Pages
A. Approved for public release;	Unclassified	115
Distribution is unlimited.	20. Security Class (This Page)	22. Price
	Unclassified	

(See ANSI-Z39.18)   *See Instructions on Reverse*   OPTIONAL FORM 272 (4-77)

Department of Commerce

Contents

List of Figures

List of Tables

Chapter 1

Introduction

It is the intent of this report to investigate possible treatments for a two-dimensional (2D) edge termination based upon both physical and electromagnetic constraints. In the context used here, an edge termination is a leading or trailing portion of an aerodynamic airfoil. The shape of the airfoil is largely controlled by aerodynamic constraints. However, the use of penetrable materials allows electromagnetic constraints to be simultaneously realized. A variety of computational methods are available to evaluate electromagnetic scattering from two-dimensional edge terminations. These techniques are continuously being improved in method, speed, and efficiency.

A traditional numerical approach is a method of moments (MoM) technique [1]. This technique can be efficiently applied to perfectly conducting or homogeneous penetrable structures since the unknowns can be limited to the perimeter of the structure. However, when the structure is inhomogeneous, the entire internal region of the structure has to be expanded with unknowns. This expansion causes the MoM approach to become exhaustive in terms of the computer resources and computation time required for generation and solution of the resulting linear system of equations.

An alternate numerical approach is a hybrid combination of both the finite element method (FEM) and the MoM [2]. This hybrid method still requires the expansion of the internal region, with the difference being that a sparse matrix is generated through the use of the FEM. The internal fields of the FEM solution are then coupled to the unbounded free space region through an integral equation formulation commonly called the boundary element method (BEM).

1

An unfortunate consequence of electromagnetic analysis for realistic structures is that a significant amount of input information is required. This input information is a discretization of the geometry under consideration, i.e., a (2D) FEM mesh. In addition, the design of a satisfactory edge termination is a problem that involves many material and structural parameters. As a computational means of searching for and keeping track of parameter combinations with desirable performance, an optimization method is used that is termed *genetic algorithm* (GA) [3]. This type of algorithm, which is based upon a self learning scheme, has many advantages over traditional optimization methods. Two advantages are that no derivative information is required and multiple solutions with different parameter combinations are possible. This GA technique is adapted for this investigation to provide ease of integration between the optimizer and an internally developed geometry mesher.

Chapter 2 presents a description of the theory and implementation of two types of triangular mesh generation schemes: Delaunay triangulation and the advancing front method. A description of these techniques and their implementation is provided. Chapter 3 presents an overview of the basic terminology and concepts of GAs. A GA software package called GENESIS [4] is applied to two problems. The results of the two problems are discussed and interpreted.

Chapter 4 contains the results of an investigation using a variety of treatments that can be applied to edge terminations. Among these treatments are conducting bulkhead orientation and shaping, variation of dielectric and/or conducting wedge angle(s), internal material loadings, placement of resistive cards, and the nulling effects of material rods. Chapter 5 uses selected results of Chapter 4 as a guide in searching for edge terminations that demonstrate desirable performance over the frequency range of interest for both transverse magnetic and transverse electric polarizations. The GA is also applied to the treatments of Chapter 4 to assist in improving current designs, as well as to explore yet unconsidered designs. All of the FEM calculations in Chapters 4 and 5 are either swept frequency (echo width versus frequency) or pattern (echo width versus angle) calculations. Additionally, time domain information pertaining to the downrange scattering characteristics of the structure is obtained

from swept frequency domain calculations. The document concludes with Chapter 6 providing a summary of the edge treatments found to be most effective.

Chapter 2

Automatic Two Dimensional Triangular Mesh Generation

2.1 Initial Considerations

2.1.1 Mesh Generation Topics

Three topics encountered when considering mesh generation are: mesh generation in two and three dimensions; mesh generation techniques using either quadrilateral/cubic or triangular/tetrahedral element meshes; and manual and semi-automatic mesh generation. For the purposes of the Finite Element Method (FEM) calculations that are performed for this report, an automatic two dimensional triangular mesh generation scheme is desired. Once this type of mesh generation is chosen, two triangulation concepts are found that are the most popular: Delaunay triangulation, and the advancing front method.

Delaunay triangulation is desirable since it insures that small included angles within each element are avoided. An efficient method of computing the Delaunay triangulation using Watson's [5] algorithm is described, complete with a FORTRAN source code, in [6]. This triangulation method can be incorporated into a mesh generation code, with two disadvantages: only convex polygonal regions can be properly triangulated and, due to this fact, concave geometries have to be broken into convex polygonal regions before meshing.

The advancing front method is desirable in that it can create meshes in convex *and* concave polygonal regions, and that the method can be used to mesh geome-

tries containing voids. Lo [7] provides a straightforward method of implementing the advancing front method, as well as a general nodal generation scheme.

2.1.2 Basic Mesh Generation Components

A basic mesh generator creates and provides a set of points to be connected (in this case triangulated), as well as the nodal connectivity of the points specifying the elements (triangles). Additionally, a mesh generator must define geometry information concerning mesh boundaries, imposed boundary conditions, and material geometry parameters.

The sections of this chapter will address mesh generation considerations and implementation with the last section providing illustrations of several meshed geometries.

2.2 Desirable Mesh Generation Characteristics

A good summary of desired characteristics of a mesh generation procedure is found in [8]:

- The algorithm should be able to handle arbitrary geometries in a fully automatic manner and with minimum user intervention.

- The input data should be reduced to a computerized geometric representation of the domain to be discretized.

- The approach followed should provide control over the spatial variation of element size and shape through the domain.

- Adaptive methods should be incorporated into the process, with the objective of producing the most accurate approximation of the solution for a given number of points.

The first two characteristics listed here are accommodated by the implemented algorithm and are described in the remainder of this chapter. Spatial variation of elements and adaptive methods are more advanced mesh generation topics. Since

the main focus of the work presented here is not mesh generation, a constant spatial variation of elements with no adaptive methods is used. When possible, FEM results calculated using this mesh generation scheme are compared with previous calculations, eigenfunction solutions, and moment method solutions to guarantee the solution accuracy (Several reference curves can be found in [2]). Adaptive methods can, however, be incorporated into the algorithm in the future should the need arise.

2.3   Mesh Generation Philosophy

Mesh generation can be divided into two steps: nodal generation and element creation. However, before these steps can take place, an adequate geometry definition is needed. The following sections describe the information contained in the geometry file, as well as the algorithms used for nodal definition and element creation.

2.3.1   Geometry Definition

For the geometries that will be defined in Chapter 4, a complete geometry file contains:

- The number of vertices in the geometry.

- Each vertex's X and Y coordinates.

- The number of regions in the geometry.

- The number of boundary segments for each region.

- Each boundary segment's type: line or arc. If the segment is an arc, the vertex number of its center and the arc's direction of rotation must be specified (clockwise or counterclockwise).

- The vertex numbers of each boundary segment's endpoints.

- Each boundary segment's enforced boundary condition, which can be one of the following:

  1. No enforced boundary condition

6

2. Perfect Electric Conductor (PEC) - Transverse Magnetic (TM)

3. Perfect Electric Conductor (PEC) - Transverse Electric (TE)

4. Resistive

If a segment is resistive, a reference number is added following the boundary condition specification. The reference number corresponds to an impedance value contained in the material file.

2.3.2   Nodal Generation

Nodal generation consists of three parts:

1. Generation of nodes on region boundaries.

2. Compression of region boundary nodes to eliminate doubly defined nodes.

3. Generation of nodes interior to region boundaries.

Once all nodes are adequately defined, they are triangulated.

2.3.3   Triangulation

Triangular mesh elements were selected over quadrilateral elements. In general, triangular meshes are used most often as they are able to mesh any polygonal region exactly. Once the decision is made to use triangular elements, a method of triangulation is chosen. The two most popular methods of triangulation are Delaunay triangulation and the advancing front method. Both methods have been implemented and will be presented here. The Delaunay triangulation method is implemented with details and source code given in [6]. Additionally, an advancing wavefront algorithm is implemented based upon Lo's [7] algorithm.

2.4   Two Dimensional Mesh Generation Implementation

Two complete mesh generation programs have been written in FORTRAN. The difference between the two codes is in their method of triangulation. The logic used in

the remaining sections of the two codes (excluding triangulation) is equivalent, with only slight differences in the logic's implementation. The equivalent sections of code are:

- ASCII interface,

- Geometry specification and

- Nodal generation.

Once a geometry has been meshed, the necessary information is written to a file in either ASCII or binary format.

2.4.1 ASCII Interface

The user interface to control the mesh is provided through the follow ASCII screen description:

```
*********** INPUT PARAMETERS ********************
1-SPECIFY GEOMETRY FILE NAME: strip3
2-ENTER NODAL SPACING: 0.1000000
3-SPECIFY OUTPUT FILE NAME (ROOT): strip3
4-OUTPUT FORMAT (T,F:BINARY,ASCII)  T
5-PLOT GRID: (n,s,h) h
*************************************************

ANY CHANGES? (INPUT ROW # OR 0=NO):
```

The required inputs are self-explanatory. The units for the nodal spacing are the same as the units used to describe the geometry in the input geometry file. Specifying the output format concatenates an extension of ".bin" or".asc" to the end of the output file name. Graphical output can be obtained through one of two means. Specifying an "s" generates a UNIX plot file while an "h" generates a postscript file. An "n" produces no graphical information.

2.4.2 Geometry Specification

The sample geometry considered is shown in Figure 2.1. The actual geometry input set, which is provided below, begins with the number of vertices in the geometry on

8
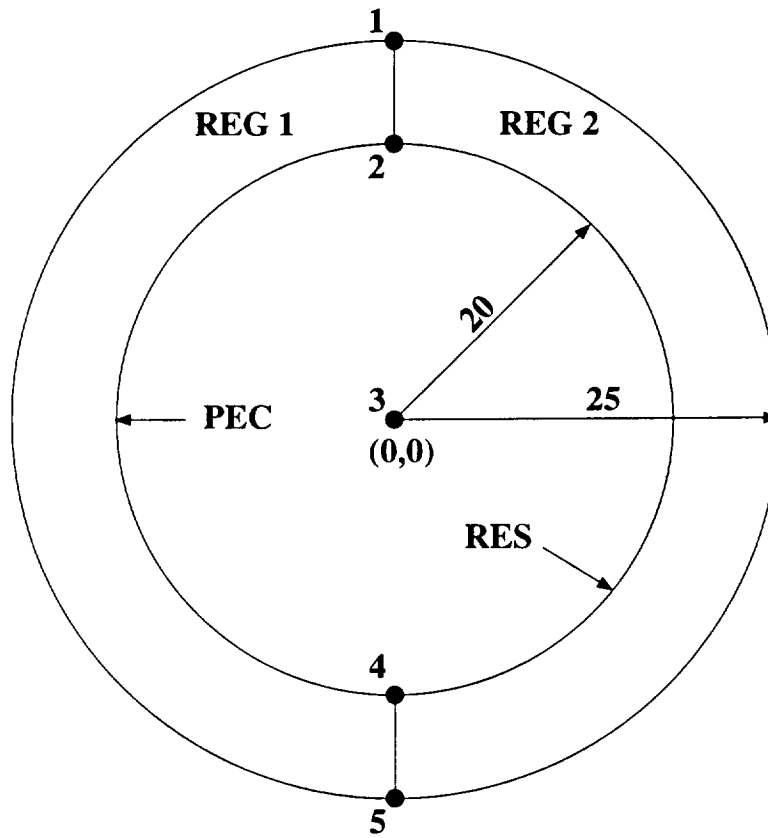
Figure 2.1: Sample geometry illustrating data file.

the first line of the data file, followed by a corresponding list of X/Y coordinate pairs for each vertex. Next, the number of regions in the geometry is listed. Finally, for each region of the geometry, there is a corresponding set of information. The number of boundary segments in the region is given at the beginning of the region information. The remaining region information contains each line segment's type: 'arc' or 'line'; each segment's endpoints listed in terms of their corresponding vertex numbers; and each segment's enforced boundary condition: 'none' - normal, 'pectm' or 'pecte' - perfect electric conductor, TM or TE, 'res' - resistive card. If the segment is an arc, the next line contains the arc's center vertex number and direction of rotation: 'cw' or 'ccw'. If the segment's boundary condition is resistive, a complex number corresponding to the segment's impedance (the actual impedance is stored in an external material file) is added on the line following the line or arc segment information. Each region's boundary segments should be defined in a counterclockwise manner.

9

It should be noted that the code that utilizes Delaunay triangulation was written to triangulate convex polygonal regions, with region boundaries made up only of straight line segments. Therefore the 'arc'/'line' distinction as well as the arc center and arc rotation direction information are not included in the geometry file when using the Delaunay triangulation code.

```
5                           ! 5 vertices
0 25                        ! vertex coordinates
0 20
0 0
0 -20
0 -25
2                           ! 2 regions
4                           ! Reg 1, 4 segments
'line' 2 1 'none'           !    straight seg, no BC
'arc' 1 5 'none'            !    arc seg, no BC
3 'ccw'                     !    center point, rotation direction
'line' 5 4 'none'           !    straight seg, no BC
'arc' 4 2 'res'            !    arc seg, resistive
3 'cw'                      !    center point, rotation direction
(-3,0)                      !    material file index number
4                           ! Reg 2, 4 segments
'line' 1 2 'none'           !    straight seg, no BC
'arc' 2 4 'pectm'          !    arc seg, PEC TM
3 'cw'                      !    center point, rotation direction
'line' 4 5 'none'           !    straight seg, no BC
'arc' 5 1 'none'           !    arc seg, no BC
3 'ccw'                     !    center point, rotation direction
```

2.4.3 Nodal Generation

Nodal Creation on Domain Boundaries

The first step of the code(s) is the creation of region boundary nodes. Each segment's length is computed, and nodes are then created along the region boundary based upon the user input nodal spacing. It is important to note that region boundaries should be created in a manner such that all common boundaries have the same vertices as endpoints. This boundary creation method insures that common boundary nodes will be created at the same locations between vertices.

Figure 2.2: Creation of boundary nodes.

Due to the method by which the region boundaries are defined, the nodal "compression" algorithm is straightforward. The code creates a list of compressed nodes, separate from the "uncompressed" boundary node list, beginning with the unique boundary nodes from the first region. The code then compares the boundary nodes of the remaining regions to the compressed node list, adding only uniquely defined nodes to the compressed list (see Figures 2.2 and 2.3). Additionally, the compression algorithm tracks and maintains a list of global node information: PEC TM, PEC TE, and RES global node numbers and their corresponding values. No nodal compression is necessary if the geometry contains a single region.

Nodal Creation Interior to Domain Boundaries

The method used for internal node creation can be summarized by the following steps [7] (see Figure 2.4):

11

Figure 2.3: Compression of boundary nodes
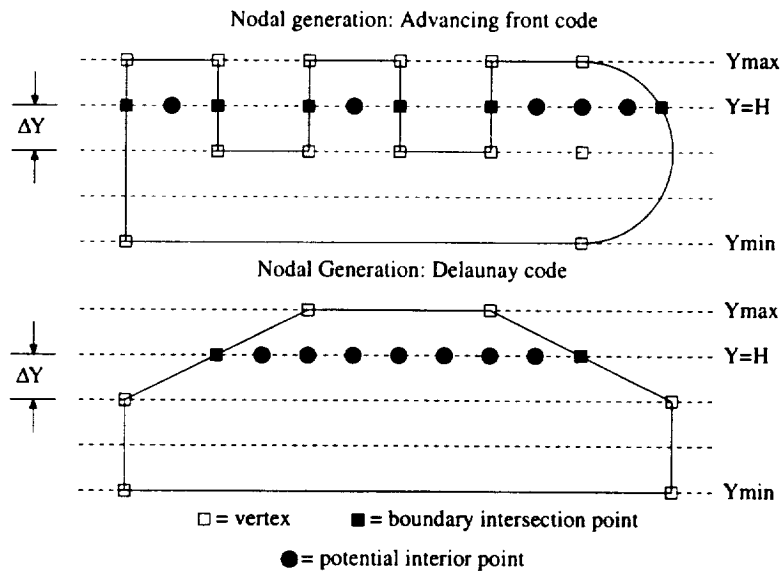
Figure 2.4: Steps for interior node creation

1. Determine the minimum and maximum Y value of the region.

2. Adjust the average element spacing for the region based upon the Y_{min} and Y_{max} values of the region and the user-input nodal spacing.

3. Make imaginary horizontal cuts at Y values determined from 1) and 2) above.

4. For each horizontal cut, determine the intersection point X coordinates by cycling through region boundary segments and determining which segments are intersected. Each boundary segment has endpoints (X1,Y1) and (X2,Y2). The imaginary line drawn at Y=H intersects a straight line segment if:

(a) $(Y1 - H)(Y2 - H) < 0$ or

(b) $(Y1 - H)(Y2 - H) = 0$ and $(H > Y1$ or $H > Y2)$

If intersection of the imaginary horizontal line with a straight line segment occurs, the X-value of the intersection point can be found from:

$$X_{\text{inter}} = X_1 + \frac{(H - Y_1)(X_2 - X_1)}{(Y_2 - Y_1)} \tag{2.1}$$

To determine whether or not intersection occurs between the imaginary horizontal line and an arc segment, consider the equation of a circle:

$$(X - X_c)^2 + (Y - Y_c)^2 = R^2 \tag{2.2}$$

The intersection points of the imaginary horizontal line (Y=H) with an arc segment are then given by:

$$X_{\text{inter}} = X_c \pm \sqrt{R^2 - (H - Y_c)^2} \tag{2.3}$$

Intersection occurs if:

(a) $R^2 - (H - Y_c)^2 \geq 0$ and

(b) The arc segment passes through X_{inter} given above.

13

5. Node creation is considered on the horizontal line of 3) between intersection points found in 4). Since the code that uses Delaunay triangulation is designed to mesh only convex polygonal regions, just two intersection points will be found in 4). The code that uses the advancing front method computes and considers 2n intersection points two at a time, with potential nodes located between each set of points (see Figure 2.4). Whether or not a node is finally created is determined by whether or not the potential internal node is sufficiently spaced apart from all region boundary nodes. If (X, Y) is a potential nodal location, (P_i, Q_i) is a boundary node, and C is a constant which is dependent on the average element size D of the region, usually defined as $.7D$, then a new node will be created if:

$$(X - P_i)^2 + (Y - Q_i)^2 < C^2 \qquad (2.4)$$

The logic used to compute intersection points in 4) above has the disadvantage that intersection points will be computed for each segment, possibly resulting in a redundant list of points. Thus, some "post processing" is implemented to sort out the correct pair(s) of intersection points between which new nodes may be created.

When nodal creation is complete for a region, the list of X and Y coordinates for nodes in the region are passed to the triangulation section of the code.

2.4.4 Triangulation

Delaunay Triangulation

This section presents Watson's [5] algorithm as described and implemented in [6]:

1. Sort the N points to be triangulated in ascending sequence of their x coordinate.

2. Define the vertices of the "supertriangle" in a counter-clockwise manner. The supertriangle is the initial Delaunay triangulation consisting of a single triangle. The size and shape of the supertriangle can be arbitrary, but should contain all of the points to be triangulated. The supertriangle should begin a list of triangles formed and flagged as incomplete.

14

3. Introduce a new point (X_{new}, Y_{new}) from the list of sorted points.

4. For each incomplete triangle, perform steps 5 to 9. (see Figure 2.6 for an illustration of terms defined in steps 5-9.)

5. Compute the coordinates of the triangle's circumcentre (X_c, Y_c) and the square of the triangle's circumcircle radius R^2. An illustration of a triangle's circumcircle radius is provided in Figure 2.5.

6. Compute the square of the distance in the x direction from the new point to the triangle's circumcentre: $D_x^2 = (X_c - X_{new})^2$.

7. If $D_x^2 \geq R^2$ then the circumcircle of the triangle cannot be intersected by any of the remaining points. Flag this triangle as complete and skip steps 8 and 9.

8. Compute the square of the distance from the new point to the triangle's circumcentre: $D^2 = D_x^2 + (y_c - y_{new})^2$.

9. If $D^2 < R^2$ then the new point intersects the circumcircle of the triangle. Remove this triangle from the list of triangles formed and store three sets of vertices defining the triangle's edges on a list of edges. If $D^2 \geq R^2$, the new point lies outside the triangle's circumcircle and the triangle remains unmodified.

10. Search the list of edges and remove all edges which occur twice in the list. This step will remove all edges which are interior to the polygon formed by the intersected triangles.

11. Form new triangles with vertices in a counter-clockwise fashion using the new point combined with the vertices of each edge of the list of edges (see Figure 2.7). Flag each new triangle as incomplete.

12. Repeat steps 3-11 until all remaining nodal points have been introduced.

13. Complete the Delaunay triangulation by removing all triangles which contain one or more of the supertriangle vertices.
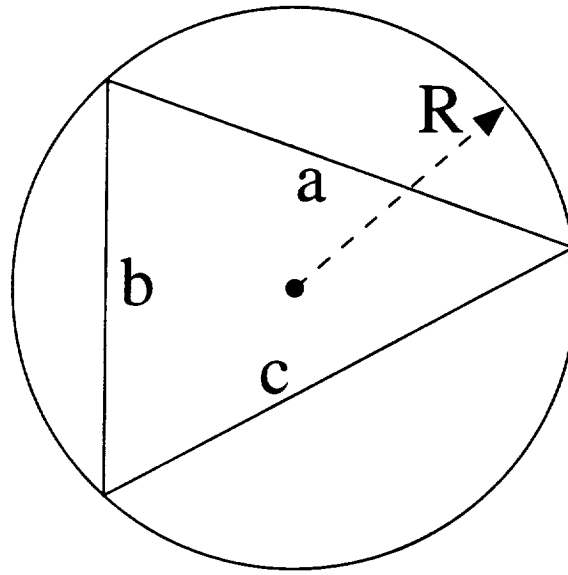
Figure 2.5: Illustration of circumcircle radius.

● = (Xnew,Ynew)

□ = triangle circumcentre (Xc,Yc)

○ = nodal points

R= circumcircle radius
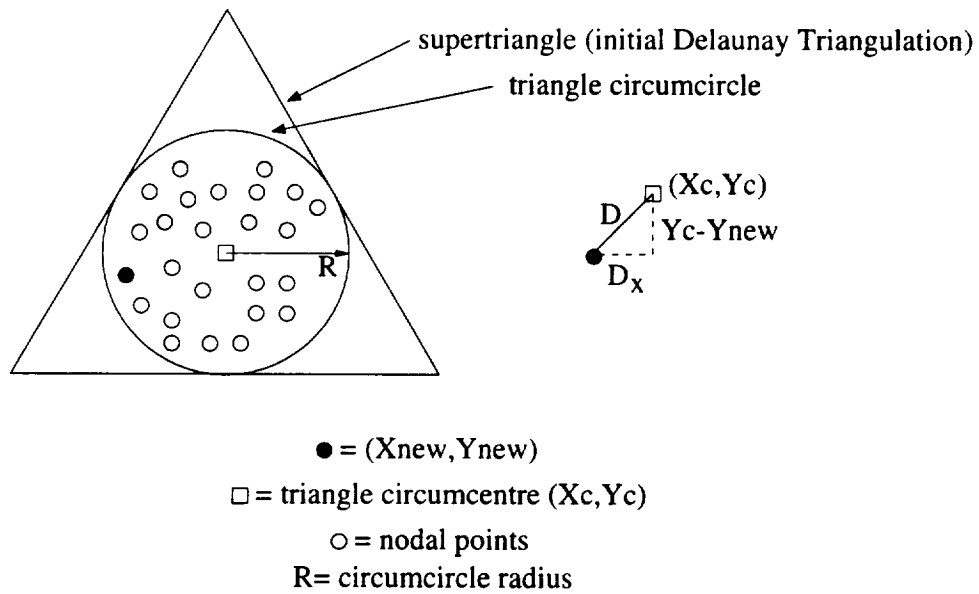
Figure 2.6: Illustration of Delaunay triangulation geometry.

New vertex D

List of edges:
AB,BC,CA

Incomplete triangles:
ABC,ABD,BCD,CAD
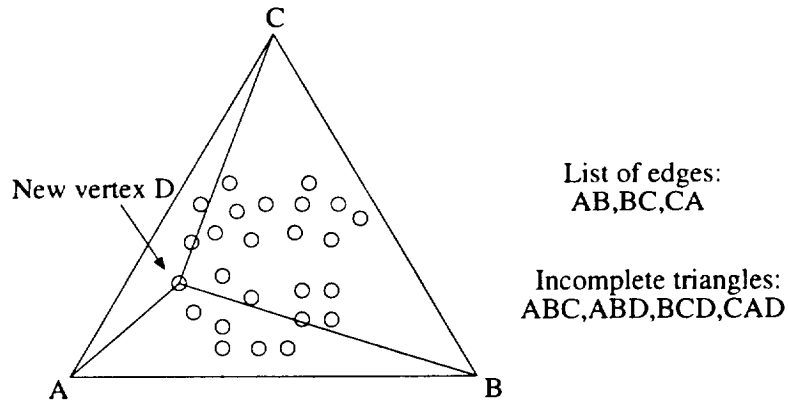
Figure 2.7: Delaunay triangulation: Formation of new triangles.

initial generation front
AB - current segment
suitable points C1 & C2

C1 = best point C
AB de-activated
BC de-activated
AC activated

best point C chosen
AB de-activated
AC activated
CB activated

■ = current active segment
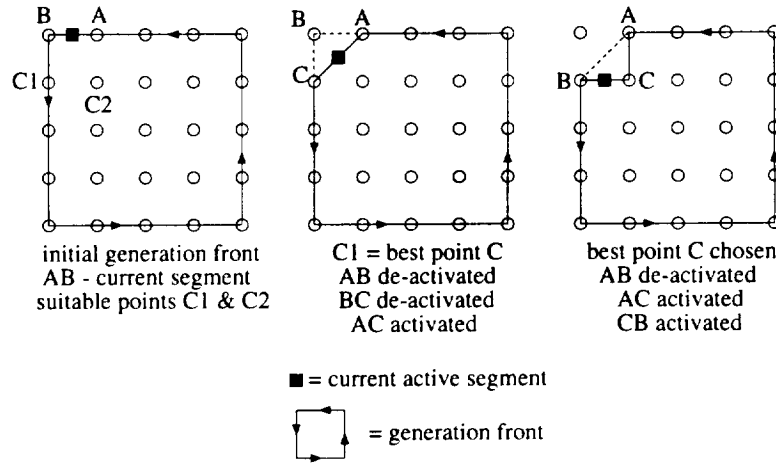
⌐⌐⌐ = generation front

Figure 2.8: Generation front illustration.

Advancing Front Triangulation Implementation

This section will describe details needed for numerical implementation of an advancing wavefront triangulation algorithm based upon a classic paper by Lo [7].

A term that needs introduction is "generation front". In the advancing wavefront method, the generation front is the collection of line segments which are available to form a new triangular element. The generation front changes continuously as each new element is created. (see Figure 2.8). Triangulation terminates when no segments remain in the generation front.

Steps that need to be executed prior to triangulation are described by the following:

17

1. Define the generation front for the current region. Initially it is the collection of boundary segments of the region listed in a counter clockwise fashion (see Figure 2.8).

2. Activate the generation front segments. Activation of the segments amounts to defining a flag to indicate which segments of a list of segments are part of the generation front.

3. Define the list of nodes to be triangulated. Maintain a link between local (referenced to the current region) node numbers and global (referenced to the entire geometry) node numbers. Nodes are classified as generation front nodes or interior nodes. A point that is suitable for triangulation with the current segment must be either a generation front or an interior node, eliminating the possibility of overlapping elements.

Triangulation then proceeds as follows:

1. Define the current active segment (CAS), segment A-B, from the list of generation front segments.

2. Find a set of potential triangulation points that have the smallest norms. The size of this set of points is dependent upon the user and is set as a program parameter. If C is a potential triangulation point, then the norm is written as $[AC^2 + CB^2]$, and defined by:

$$[AC^2 + CB^2] = [(X_A - X_C)^2 + (Y_A - Y_C)^2] + [(X_B - X_C)^2 + (Y_B - Y_C)^2] \quad (2.5)$$

3. Since the generation front is defined in a counterclockwise manner, all valid triangulation points will be situated to the left of the CAS. Points found from the previous step are flagged as valid or invalid based upon whether they are to the left or to the right (or co-linear) to the CAS, respectively. The two points to the left of the CAS with the smallest norms, defined as C_1 and C_2, are considered the best potential triangulation points and are compared in the next step.

18
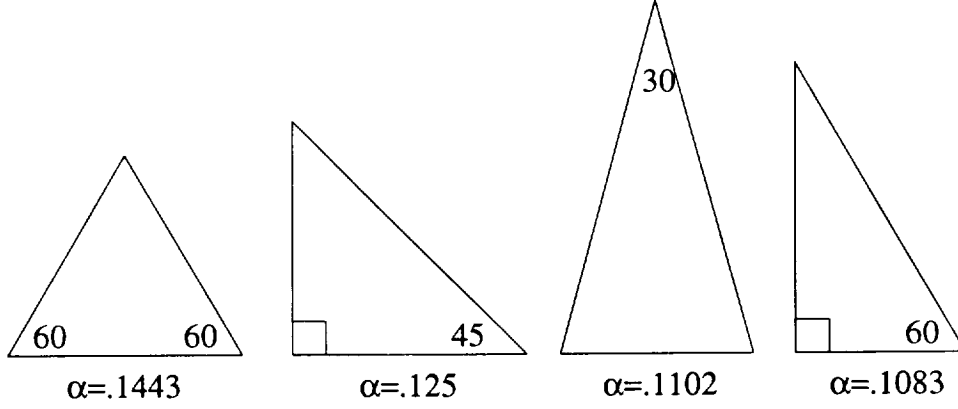
Figure 2.9: Triangle quality examples.

4. The quality of triangles C_1 and C_2 are computed from the following relations, where $\triangle ABC =$ the area of triangle ABC:

$$\alpha_1 = \frac{\triangle ABC_1}{AB^2 + BC_1^2 + C_1A^2} \tag{2.6}$$

$$\beta_1 = \frac{\triangle C_1BC_2}{C_1B^2 + BC_2^2 + C_1C_2^2} \tag{2.7}$$

$$\delta_1 = \frac{\triangle AC_1C_2}{AC_1^2 + C_1C_2^2 + C_2A^2} \tag{2.8}$$

$$\lambda_1 = max(\beta_1, \delta_1) \tag{2.9}$$

$$\alpha_2 = \frac{\triangle ABC_2}{AB^2 + BC_2^2 + C_2A^2} \tag{2.10}$$

$$\beta_2 = \frac{\triangle C_2BC_1}{C_2B^2 + BC_1^2 + C_1C_2^2} = -\beta_1 \tag{2.11}$$

$$\delta_2 = \frac{\triangle AC_2C_1}{AC_2^2 + C_2C_1^2 + C_1A^2} = -\delta_1 \tag{2.12}$$

$$\lambda_2 = max(\beta_2, \delta_2) \tag{2.13}$$

C_1 is chosen if $\alpha_1\lambda_1 > \alpha_2\lambda_2$, otherwise C_2 is chosen. Some examples of computed triangle quality are shown in Figure 2.9. The larger the α value, the more suitable the element for the finite element method. Details of triangle quality criterion given by the above equations should be referenced to [7].

19

5. To insure that the new element ABC does not overlap an existing element, it should be verified that the most suitable point C is either on the generation front or an interior point.

6. Add the new element to the list of elements for the current region.

7. De-activate the current edge.

8. Activate and de-activate segments accordingly. The three cases that can occur are illustrated in Figures 2.8 and 2.10 and are described as follows:

   (a) De-activate old segments AB and BC, activate new segment AC.

   (b) De-activate old segment AB, activate new segments AC and CB.

   (c) De-activate old segments AB, BC, and CA (corner element).

   The logic used for the appropriate activation and de-activation of segments is illustrated with the following pseudo-code:

```
De-activate current segment AB
If segment AC is already active, flag AC as old
If segment CB is already active, flag CB as old
If AC is not old then
  Activate AC
  Add AC to active segment list
end
If CB is not old then
  Activate CB
  Add CB to active segment list
end
If one or more new segments are added then
  Point to last added segment
  If only one new segment is added then
    De-activate old segment
    Decrement active segment counter
  end
else (corner element logic)
  Find new active segment by decrementing generation
  front pointer
end
```

9. Find the new CAS by pointing to the last active segment in the generation front segment list.

corner element
encountered

AC de-activated
BC de-activated
CA de-activated
new active segment found

■ = current active segment

= generation front

Figure 2.10: Corner element logic.

10. If three or more active generation front segments remain, return to step 2) and continue the triangulation process.

2.5   Meshed Geometries

Three meshed geometries are shown in Figures 2.11 through 2.13. The meshes correspond to a PEC cylinder, two PEC cylinders, and a semicircular PEC cylinder with dielectric skin. The files used to create the geometries are given in Figures 2.14 through 2.16.

Figure 2.11: Meshed single cylinder geometry.
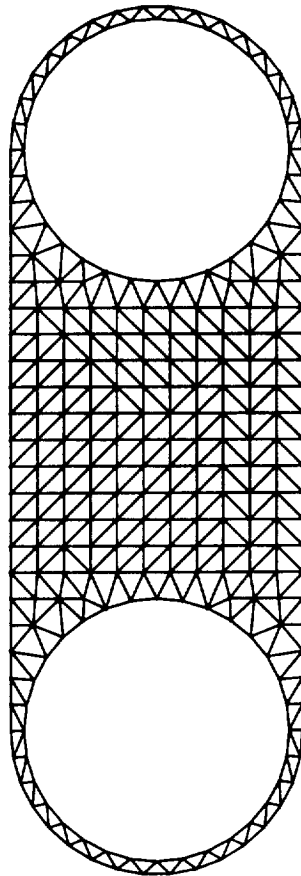
Figure 2.12: Meshed dual cylinder geometry.
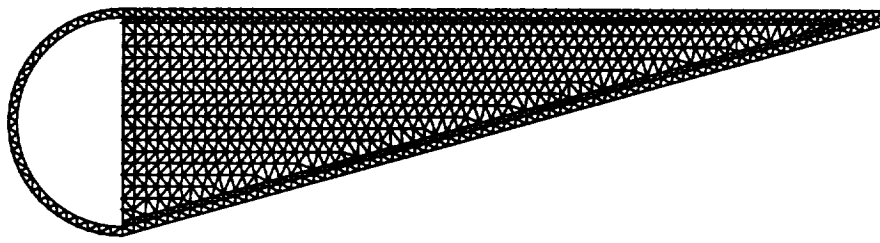
Figure 2.13: Meshed semicircular cylinder with material skin geometry.

```
5
0 70
0 60
0 0
0 -60
0 -70
2
4
'line' 2 1 'none'
'arc' 1 5 'none'
3 'ccw'
'line' 5 4 'none'
'arc' 4 2 'pectm'
3 'cw'
4
'line' 1 2 'none'
'arc' 2 4 'pectm'
3 'cw'
'line' 4 5 'none'
'arc' 5 1 'none'
3 'ccw'
```

Figure 2.14: Single PEC cylinder geometry input file.

```
10
-11 22
-10 22
0 22
10 22
11 22
-11 -22
-10 -22
0 -22
10 -22
11 -22
3
8
'line' 10 5 'none'
'line' 5 4 'none'
'arc' 4 2 'pectm'
3 'cw'
'line' 2 1 'none'
'line' 1 6 'none'
'line' 6 7 'none'
'arc' 7 9 'pectm'
8 'cw'
'line' 9 10 'none'
4
'arc' 5 1 'none'
3 'ccw'
'line' 1 2 'none'
'arc' 2 4 'pectm'
3 'cw'
'line' 4 5 'none'
4
'line' 10 9 'none'
'arc' 9 7 'pectm'
8 'cw'
'line' 7 6 'none'
'arc' 6 10 'none'
8 'ccw'
```

Figure 2.15: Dual PEC cylinder geometry input file.

```
11
0.000000 0.000000
0.000000 0.500000
0.000000 0.829775
0.000000 6.850000
0.000000 12.882500
0.000000 13.200000
0.000000 13.700000
42.931801 12.882500
45.237396 13.200000
45.737396 12.840371
45.737396 13.700000
4
7
'line' 10 11 'none'
'line' 11 7 'none'
'line' 7 6 'none'
'line' 6 9 'none'
'line' 9 2 'none'
'line' 2 1 'none'
'line' 1 10 'none'
6
'line' 2 9 'none'
'line' 9 6 'none'
'line' 6 5 'pectm'
'line' 5 8 'none'
'line' 8 3 'none'
'line' 3 2 'pectm'
3
'line' 8 5 'none'
'line' 5 3 'pectm'
'line' 3 8 'none'
4
'line' 6 7 'none'
'arc' 7 1 'none'
4 'ccw'
'line' 1 2 'none'
'arc' 2 6 'pectm'
4 'cw'
```

Figure 2.16: Semicircular PEC cylinder geometry with dielectric skin geometry file.

Chapter 3

Genetic Algorithms

Genetic algorithms (GAs) [3], as applied to numerical optimization problems, attempt to imitate the concept of "survival of the fittest" in nature by simulating the processes of genetic reproduction, recombination, mutation, and evolution. A description of the basic concepts and terms related to GAs as well as some simple applications will be presented in the following sections.

3.1   Basic Theory and Terms

Each parameter of a problem of interest is constrained to fall within a specified range. The range for each parameter is discretized into a set of equally spaced values. The set size is defined using a power of two, allowing each parameter value to be encoded as a binary sequence. Each of these binary sequences is termed a gene. As an illustration of a gene, see Figure 3.1. In this example, the parameter that is discretized is the separation distance between a PEC plate and a resistive card. The upper and lower bounds of this parameter are defined as 8 cm and 1 cm, respectively, with the chosen discretization being defined by 2^3 or 8 values. Thus, the granularity for this parameter is 1 cm. In theory, a GA parameter can be defined using any range, and discretized using any power of two.

Each of n genes of a set are appended together to form a chromosome. As an illustration, consider the geometry shown in Figure 3.2. A chromosome is simply a single binary number encoded to represent a specific value of each of the n parameters

PEC   R-card

d

1 cm   8 cm

parameter: separation distance d
min: 1 cm
max: 8 cm
discretization: 8 (2^3)

gene code	parameter value
000	1 cm
001	2 cm
010	3 cm
011	4 cm
100	5 cm
101	6 cm
110	7 cm
111	8 cm
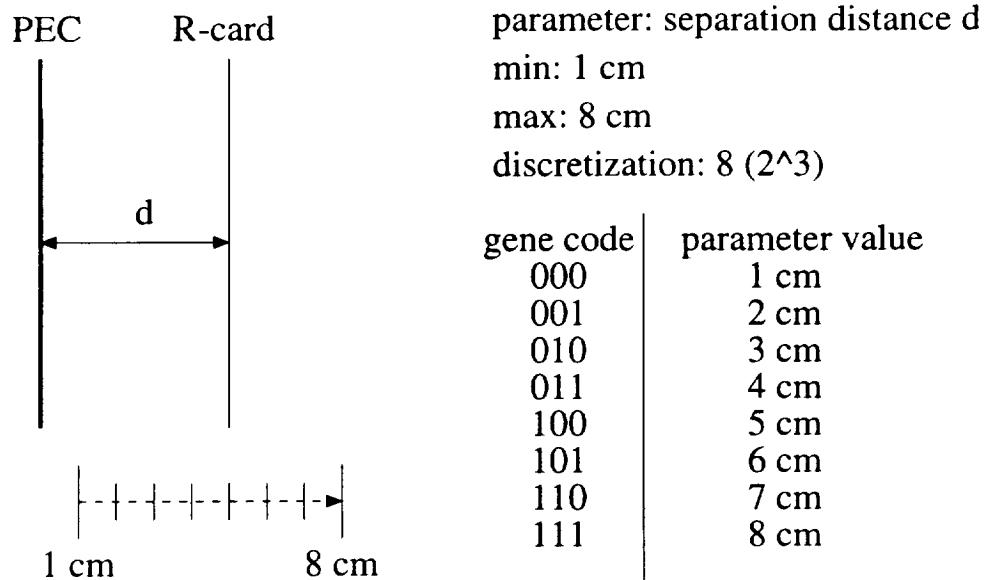
Figure 3.1: Illustration of a gene.

simultaneously. In this example, the two parameters represented by a chromosome are separation distance and resistive sheet value.

Once the concepts of gene and chromosome have been introduced, it is useful to reference a flowchart similar to that of Figure 3.3 to help describe the main processes of a GA. A collection of chromosomes is termed a population. Initially, a population is created by generating a random collection of chromosomes. Once an initial population is created, the "fitness" of each member chromosome is computed. A chromosome's fitness, in general, can be thought of as a numerical assessment of some user-defined "quality" measure based upon the given set of input parameters. After an initial random population has been generated, the creation of a new population begins. The original population is altered by implementing, in a probabilistic manner, the concepts of crossover, mutation, and reproduction.

Crossover involves selecting, based on fitness, two chromosomes or "parents" of the current population and combining some part of the first parent's string information with the complementary part of second parent's string information. A crossover point is randomly selected, with a pair of offspring resulting from "splicing" the binary information from both parents together. See Figure 3.4.

PEC   R-card

parameter 1: seperation distance d   parameter 2: R-card value RES
min: 1 cm   d   min: 100 Ω/□
max: 8 cm   max: 800 Ω/□
discretization: 8 (2^3)   discretization: 8 (2^3)

gene 1	d value	gene 2	RES value	Chromosome examples:
000	1 cm	000	100 Ω/□	010 + 110 = 010110 : d=3, RES=700
001	2	001	200	101 + 001 = 101001 : d=6, RES=200
010	3	010	300	111 + 000 = 111000 : d=8, RES=100
011	4	011	400	
100	5	100	500	genes chromosomes
101	6	101	600	
110	7	110	700	
111	8	111	800	

Figure 3.2: Illustration of a chromosome.

Mutation involves the toggling of a small percentage of bits in the population of chromosomes. Increasing the number of mutations allows a GA more freedom to search for solutions outside the present population. Goldberg [9] states:

> That the mutation operator play a secondary role in the simple GA, we simply note that the frequency of mutation to obtain good results in empirical genetic algorithm studies is on the order of one mutation per thousand bit (population) transfers. Mutation rates are similarly small (or smaller) in natural populations, leading us to conclude that mutation is appropriately considered as a secondary mechanism of genetic algorithm adaptation... when used sparingly with reproduction and crossover, it is an insurance policy against premature loss of important notions.

Reproduction involves selecting an individual chromosome based upon its fitness as compared to others within the current population. Once this chromosome has been selected, it is merely copied and placed into the new population.

Crossover, mutation, and reproduction continue until a new population is completed. A complete population is termed a generation. After each new generation

30

Gen := 0

Create Initial
Random population

Termination
Criterion Satisfied? —— Yes —→ Designate
Result

No

Evaluate Fitness of Each
Individual in Population

End

i := 0

Gen := Gen + 1 ←— Yes —— i = M?

No

Select One
Individual
Based on Fitness

P_r

Select Genetic Operation
Probabalistically

P_m

Select One
Individual
Based on Fitness

Perform Reproduction

P_c

Select Two Individuals
Based on Fitness

Perform Mutation

Copy into New
Population

i := i + 1

Insert Mutant into
New Population

Perform
Crossover

Insert Two
Offspring
into New
Population

i := i + 1

Figure 3.3: Flowchart of a conventional genetic algorithm.

31

$$\text{parent \#1: } \textbf{\textit{10101}} \,|\, 0010101$$
$$\text{parent \#2: } 11100 \,|\, \textbf{\textit{1100101}}$$

$$\text{offspring \#1: } \textbf{\textit{10101}} \,|\, \textbf{\textit{1100101}}$$
$$\text{offspring \#2: } 11100 \,|\, 0010101$$

crossover point
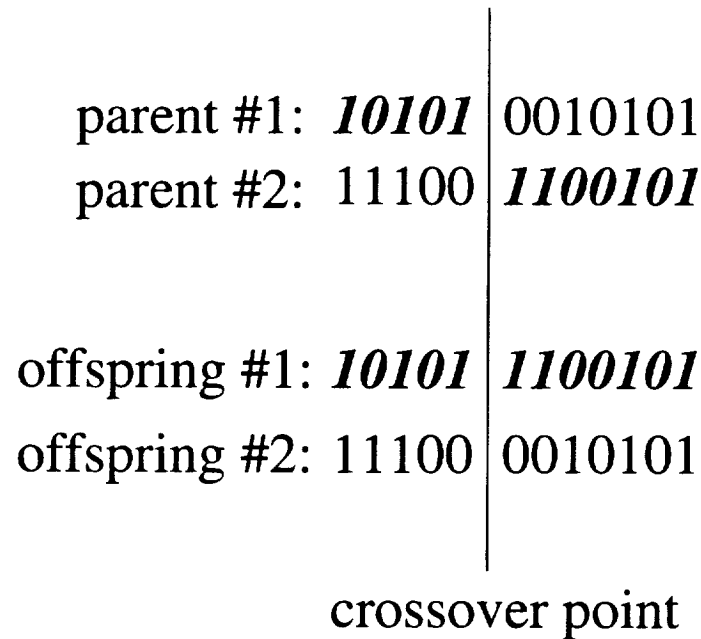
Figure 3.4: Illustration of crossover.

is created, it is analyzed to determine if a specified termination criterion has been satisfied. If the criterion have been satisfied, the algorithm is complete, otherwise new generations continue to be created.

3.2 Differences between Genetic Algorithms and Traditional Methods

Goldberg cites four main ways in which GAs are different from normal optimization and search procedures:

1. GAs work with a coding of the parameter set, not the parameters themselves.

2. GAs search from a population of points, not a single point.

3. GAs use payoff (objective function) information, not derivatives or other auxiliary knowledge.

4. GAs use probabilistic transition rules, not deterministic rules.

32

The advantage of working with a coding of the parameter set is described using the concept of the "black box". Encoding the parameter set to form a single binary number is much like using a set of binary switches as input to a black box which has a single output. The input switches are toggled to "on" or "off" in an organized fashion (initially at random), producing an output value representing the fitness of the particular binary string. This method of using only the single black box output value allows GAs to be removed from the problems associated with the internal workings of the box. (Some examples of the "problems" that may be associated with the black box are continuity, existence of derivatives, etc.)

An important example that illustrates the advantages of using information from a population of points, as opposed to information from a single point, is a search space that contains many peaks. This multi-peak situation is where many optimization methods will locate false peaks, due to their lack of global information. Since GAs use information from many points simultaneously, their probability of finding an incorrect peak is greatly reduced in comparison with point to point methods.

Another characteristic of GAs that makes them desirable over traditional methods is the fact that are essentially independent of auxiliary information. They rely only upon the previously discussed fitness information. Goldberg points out that:

> ... the refusal to use specific knowledge when it does exist can place an upper bound on the performance of an algorithm when it goes head to head with methods designed for that problem.

One final difference discussed here is that GAs use probabilistic methods. GAs initially use random search to create a broad collection of candidate solutions. Once a variety of candidate solutions exist, GAs use crossover, reproduction, and mutation to lead the search towards unchartered regions of the solution space where improvement is likely. This form of search guidance is possible due to the fact that each new population helps to bias the search based upon what has worked best so far. A search that guides itself based upon known information is more effective than a purely

random search which may contain a very large number of possible solutions, and has no specific direction to its search.

3.3 Example Applications

3.3.1 Infinite Geometry

As an example of an application of a GA, consider a TM polarized plane wave incident upon an infinite PEC plate with resistive sheet geometry as shown in Figure 3.5. Suppose a search is desired to find the best combination of resistance and separation distance to minimize the reflected field. Keeping this goal in mind, the experiment proceeds as follows. Let the frequency of interest be 0.3 GHz such that the free space wavelength is 1 m. Additionally, let d be the separation distance between the PEC and the resistive sheet in m, and RES be the resistive value of the sheet in $\Omega/\square$. Initially the minimum, maximum, and granularity of d are set to .1, 1.0, and $2^6 = 64$ parameter levels ($\Delta d \simeq 1.43$cm), respectively. Likewise, the minimum, maximum, and granularity of RES are set to 10, 1280, and $2^7 = 128$ parameter levels ($\Delta RES \simeq 10\Omega/\square$), respectively. The total number of possible parameter combinations in this example is thus $2^{13} = 8192$.

A search was performed, using the parameters described above, using the GA software GENESIS [4]. (Specific details about the use of GENESIS can be found in [10].) In general, a setup program is provided that acquires information about each search. The input information is recorded by two files, "in.esl" and "template.esl", where the extension "esl" can be any user defined extension name. The template file contains the pertinent information about the run, and is described below.

Total Trials Controls the number of times a numerical assessment of a chromosome is calculated.

Population Size Specifies the number of chromosomes per population.

Structure Length Specifies the number of bits per chromosome.
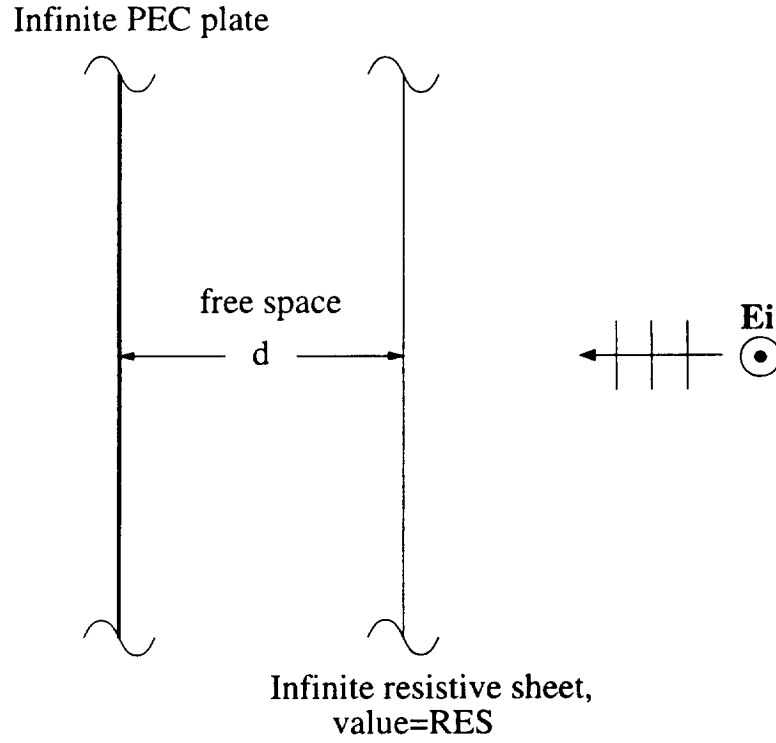
Figure 3.5: Geometry corresponding to a two parameter search for optimum distance of separation and resistive sheet value.

Crossover Rate Specifies the percentage of each population (number of genes in each population) in which crossover occurs.

Mutation Rate Specifies the percentage of bits which are mutated (toggled).

Generation Gap Specifies the fraction of the population which is replaced in each generation.

Scaling Window A brief explanation of the scaling window is given as follows:

The fitness $u(x)$ of a structure x can be defined by:

$$u(x) = f_{max} - f(x) \qquad (3.1)$$

where f_{max} is the maximum value that f(x) can take on in the given search space. Setting the scaling window W to a value greater than 0 sets f_{max} to the greatest value of $f(x)$ that has occurred in the last W generations.

35

```
         Experiments = 1
        Total Trials = 1000
     Population Size = 50
    Structure Length = 13
      Crossover Rate = .6
       Mutation Rate = .001
      Generation Gap = 1
      Scaling Window = 5
     Report Interval = 100
    Structures Saved = 10
    Max Gens w/o Eval = 2
       Dump Interval = 0
         Dumps Saved = 0
             Options = bCefgo
         Random Seed = 123456789
            Rank Min = .75
```

Figure 3.6: "in" file contents corresponding to a coarse two parameter search for optimum separation distance and resistive sheet values.

Report Interval Specifies the number of trials that occur between collection of experiment information data.

Structures Saved Specifies the number of best structures that are to be saved and placed in the ".min" file which is described later.

Max Gens w/o Eval Sets the number of consecutive generations which are permitted without any fitness evaluation.

Options Control the output and program execution which are documented in [10].

Rank Min Specifies the minimum number of offspring used in ranking and is used only if the appropriate option is set.

The contents of the "in" and "template" files for the case described above are shown in Figures 3.6 and 3.7. The user creates a subroutine to assign each parameter combination a fitness value. In this example, the magnitude of the reflected field represents the fitness of the particular combination of separation distance and resistance.

```
genes: 2

gene 0
min: 0.1
max: 1
values: 64
format: %10.4f

gene 1
min: 10
max: 1280
values: 128
format: %10.4f
```

Figure 3.7: "template" file contents corresponding to a coarse two parameter search for optimum separation distance and resistive sheet values.

Once execution of the search has terminated, a "min" file is created. This file contains the best parameter combinations encountered, each combination's fitness, and the generation and trial counters at the time of the first occurrence of the combination. The results from this run are summarized in Table 3.1.

Basic transmission line theory helps to explain the results of this search, as shown in Figure 3.8. Using impedance matching concepts, a short circuit is converted to an open circuit when transformed using a transmission line whose length is an odd multiple of $\lambda_0/4$ at the design frequency f_0. Once the short circuit is converted to an open circuit, setting R_s equivalent to the characteristic impedance of the line (in this case $\eta_0 = \sqrt{\mu_0/\epsilon_0} \simeq 377\Omega$) is sufficient to eliminate reflection. Note that, in contrast to point to point methods, two solutions were found in this search space.

An important observation should be made at this point. When discretizing continuous input parameters, it is possible that the discretization will not include a parameter level that could potentially have led to a combination with better fitness. For example, the fitness values of the two solutions found in this search are very similar, but suppose that levels of 30 dB down are not sufficient. Lower levels may be possible, but may not have been found due to better parameter values being missed by the search even if they fall between the max and min of the defined parameter window. As another experiment, it is useful to narrow the parameter search windows

37

Table 3.1: Results of coarse two parameter search for optimum distance of separation and resistive sheet value.

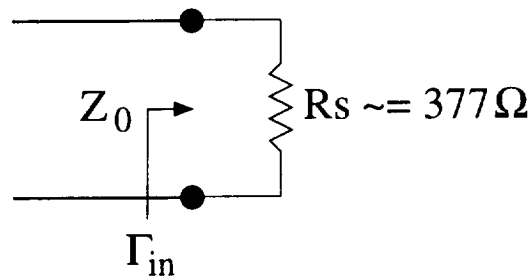| d (m)	R_s ($\Omega/\square$)	Magnitude (dB)	generation	trial
0.7429	380.0000	-3.2809e+01	11	278
0.2571	370.0000	-3.2348e+01	14	317
0.2429	380.0000	-3.2809e+01	7	201
0.2429	370.0000	-3.2348e+01	25	403
0.7571	380.0000	-3.2809e+01	9	236
0.7571	390.0000	-3.0924e+01	8	212
0.7429	390.0000	-3.0924e+01	9	241
0.2571	390.0000	-3.0924e+01	2	92
0.2429	390.0000	-3.0924e+01	6	179
0.2571	380.0000	-3.2809e+01	4	123

.

.
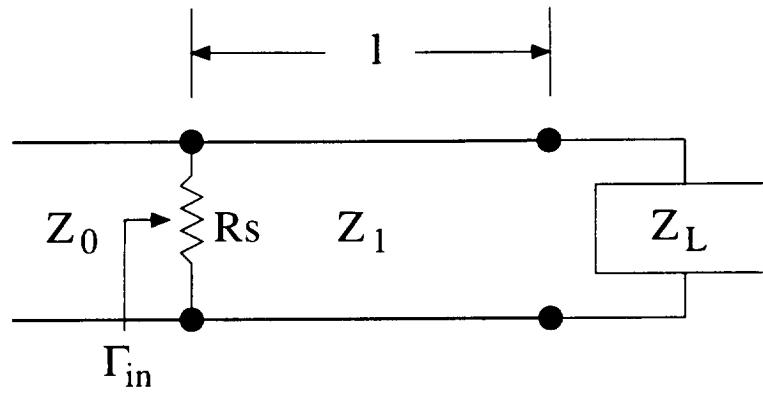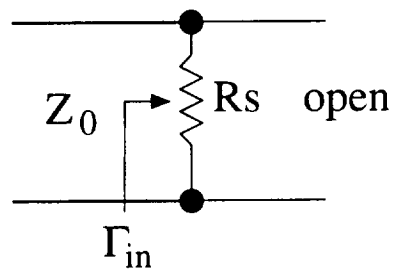
Figure 3.8: Basic transmission line theory.

```
genes: 2

gene 0
min: 0.1
max: 0.5
values: 64
format: %10.4f

gene 1
min: 10
max: 640
values: 128
format: %10.4f
```

Figure 3.9: "template" file corresponding to a finely discretized two parameter search for optimum separation distance and resistive sheet value.

while keeping the number of discretizations constant. This narrowing allows finer parameter values to be tested based upon combinations that were promising in the previous search.

As an illustration, the parameter window for d is modified to have minimum and maximum values of 0.1 and 0.5, respectively, with granularity of $2^6 = 64$ parameter levels ($\Delta d \simeq .635$cm). The parameter window for RES is also narrowed to have minimum and maximum values of 10 and 640, respectively, with granularity of $2^7 = 128$ parameter levels ($\Delta RES \simeq 4.96\Omega/\square$). The narrowing of the parameter windows in this case allows further investigation of the solution near 0.25 m and 380 $\Omega/\square$. The "template" file for this example is shown in Figure 3.9. The "in" file remains the same as in the first example. The results of this search are shown in Table 3.2. Utilizing a more narrowly defined search space, the GA is able to focus upon the minimum that occurs at $d = \lambda_0/4$ and $RES = \eta_0 \simeq 377\Omega$.

3.3.2 Semi-infinite Geometry

The previous calculations were performed using structures of infinite extent. A more practical geometry to apply a GA to is that of Figure 3.10. A two dimensional FEM analysis is used to calculate the backscatter levels of various separation and resistive

Table 3.2: Results of a finely discretized two parameter search for optimum distance of separation and resistive sheet value.

d (m)	R_s ($\Omega/\square$)	Magnitude (dB)	generation	trial
0.2524	372.1260	-4.0107e+01	7	175
0.2460	372.1260	-3.7083e+01	4	120
0.2524	382.0472	-3.9960e+01	3	93
0.2460	377.0866	-3.8083e+01	10	242
0.2460	382.0472	-3.6953e+01	7	178
0.2524	377.0866	-4.2519e+01	5	143
0.2460	367.1654	-3.4868e+01	7	168
0.2524	367.1654	-3.6399e+01	5	146
0.2460	387.0079	-3.4800e+01	2	74
0.2524	387.0079	-3.6401e+01	14	274

Finite PEC plate

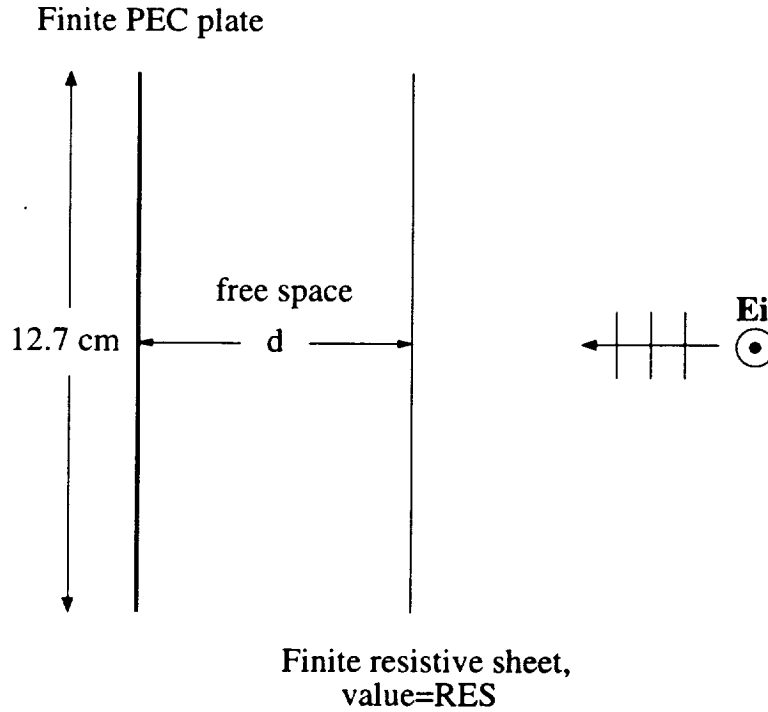Finite resistive sheet,
value=RES

Figure 3.10: Second geometry corresponding to a two parameter search for optimum distance and resistive sheet value.

sheet values with structured data scan results shown in Figure 3.11. A two dimensional GA search was performed using the parameter space defined by the "template" file contents shown in Figure 3.12. As expected, the peak was found with optimum parameter combinations given by the "min" file shown in Table 3.3. The peak levels found in the search space are not as low as obtained through the use of the structured grid. This can be contributed to discretization of continuous parameters. The peak computed by the scanned parameter set resulted from a parameter combination that was not possible based upon the parameter discretizations that were defined for this search.

3.3.3 Conclusions

The previous examples represent searches for optimum combinations of just two parameters. In these cases, it is more reasonable to search the solution space and describe the data using an illustration similar to that of Figure 3.11. There may be times where this is not practical for two reasons.
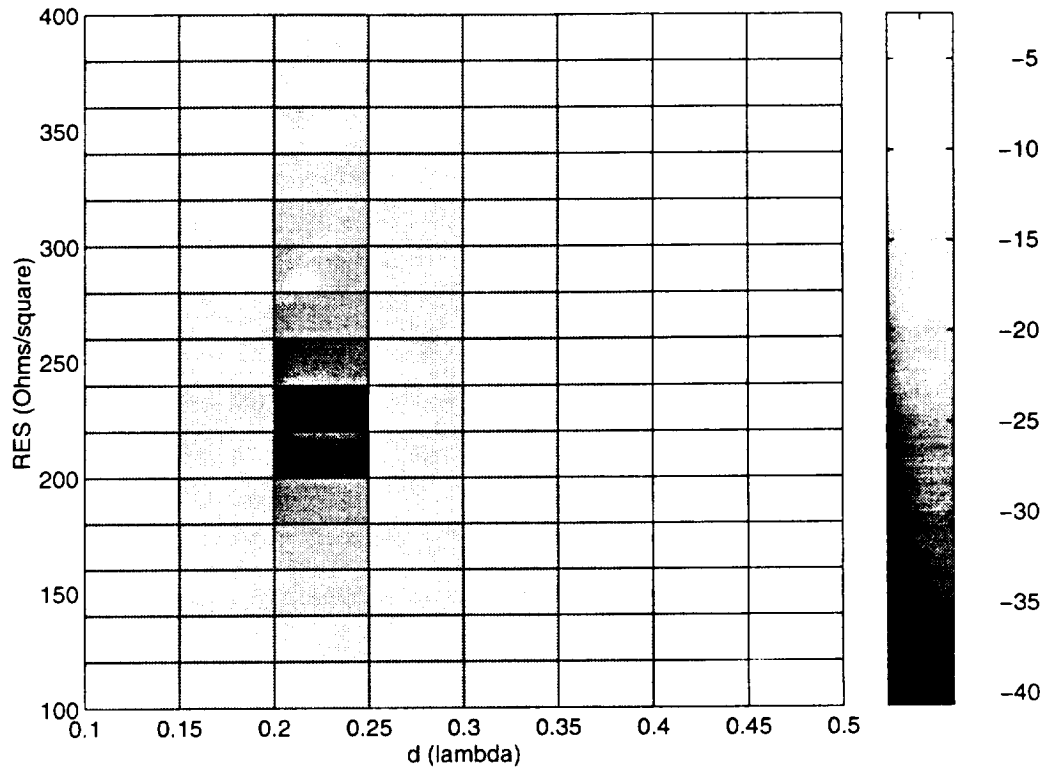
Figure 3.11: 2-D scan for minimal reflected field from a 5 inch PEC plate with one 5 inch resistive card. 0° incidence, TM polarization, $f = 1$ GHz.

```
genes: 2

gene 0
min: 100
max: 400
values: 32
format: %10.4f

gene 1
min: 0.1
max: 0.5
values: 32
format: %10.4f
```

Figure 3.12: "template" file corresponding to the search for optimum resistive sheet and separation distance values of the finite geometry.

Table 3.3: Search results for optimum resistive sheet and separation distance values of a finite geometry.

R_s ($\Omega/\square$)	d (λ)	Echo Width (dBm)	generation	trial
225.8065	0.1903	-3.3205e+01	7	180
196.7742	0.1903	-2.9238e+01	7	179
225.8065	0.2032	-3.4312e+01	4	134
235.4839	0.2032	-3.1559e+01	4	131
235.4839	0.1903	-3.0283e+01	0	42
254.8387	0.2032	-2.6644e+01	3	103
216.1290	0.2032	-3.4452e+01	6	159
245.1613	0.1903	-2.7747e+01	3	94
216.1290	0.1903	-3.4690e+01	5	141
245.1613	0.2032	-2.8836e+01	6	165

The first reason is that the computational time to create a set of data may be quite large. For example, if it is desired to create a data set of 100 distances and 100 resistance values, this represents 10,000 data points. If each data point takes 1 second to compute, this amounts to close to three hours of computation time. In this case it would be much more desirable to use a GA to search the solution space using a fraction of the number of data points.

A second and more important reason that it may not be practical to perform a parameter scan would be when more than two parameters are of interest in a search. GAs are designed in general such that they search the solution space of a single parameter problem using the same algorithm that they search the solution space of a multi-parameter problem.

Chapter 4

Scattering Reduction Techniques

The basic components of the geometry of interest are illustrated in Figure 4.1. The geometry consists of a conducting bulkhead, a dielectric skin, and a resulting internal region. The goal of this chapter is to provide an investigation of the scattering behavior of each component of the geometry separately before attempting to understand the interaction of all the components simultaneously.

4.1 Conducting Bulkhead Characterization

The conducting bulkhead of the scatterer of interest is modeled using various geometries shown in Figure 4.2. It is desired to reduce the backscatter levels of the PEC bulkhead(s) over a range of frequencies and incidence angles. The backscatter characteristics of each of these geometries are shown in Figure 4.3. Note that a conducting bulkhead with a wedge shaped PEC termination has lower backscatter levels over the frequency range of interest.
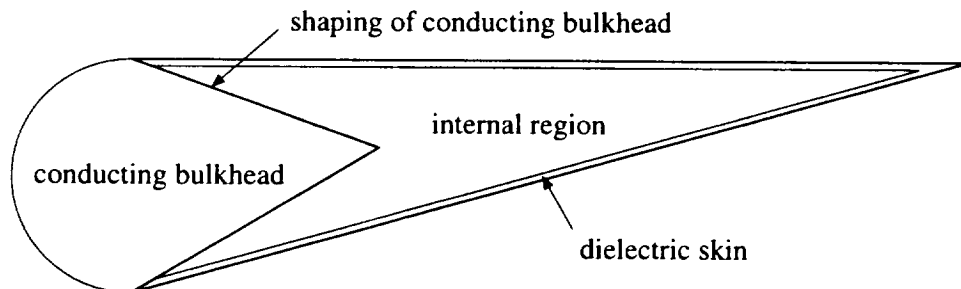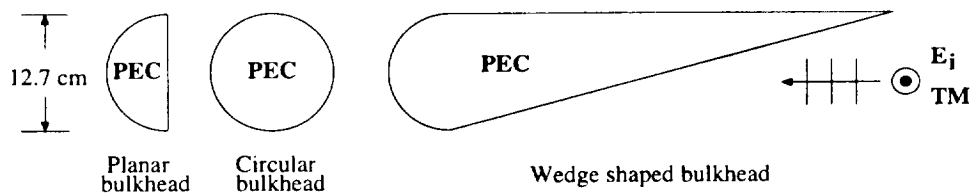

Figure 4.1: Basic geometry components.

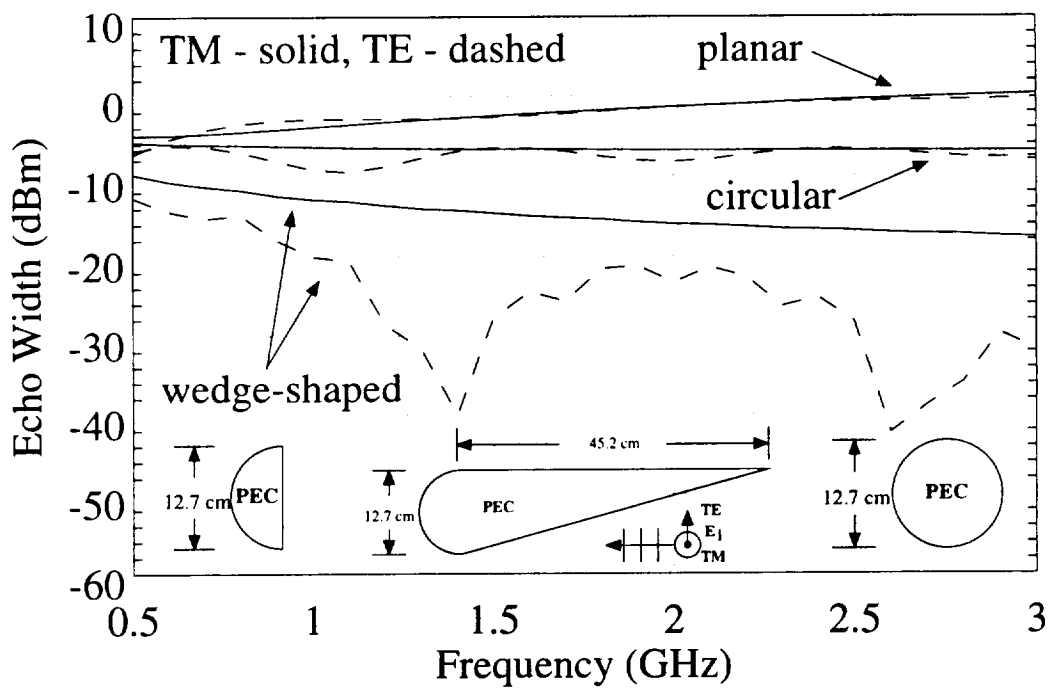Figure 4.2: Bulkhead geometries.

Figure 4.3: Echo widths for the planar, circular, and wedge shaped bulkheads.
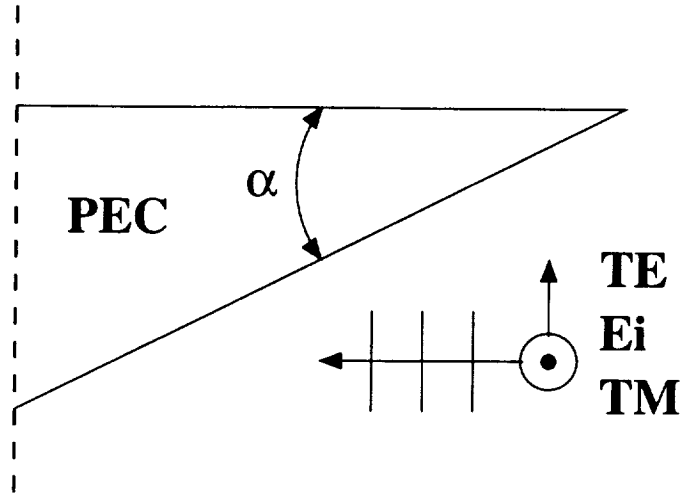
47

Figure 4.4: Infinite PEC wedge geometry.

4.2 Conducting Bulkhead Shape Considerations

4.2.1 Wedge Angle

In the previous section, it is illustrated that a wedge shaped conducting bulkhead with a wedge angle of approximately 15° has lower backscatter levels than both the circular and planar bulkheads. To further investigate the dependence of the diffracted field on wedge angle, consider the geometry shown in Figure 4.4. Using a GTD approximation [11], the diffraction characteristics of this geometry are computed and given in Figure 4.5. Additionally, Figure 4.6 illustrates the frequency response of an infinite PEC wedge. Figure 4.5 suggests that TM polarization limits how much of an effect wedge angle can have on the diffracted field. The data also suggests that variation of wedge angle has little effect on the diffracted field when the wedge angle considered remains small.

4.2.2 Planar Bulkhead Orientation

Consider the geometry shown in Figure 4.7. Figure 4.8 illustrates how the echo width level changes as the angle of incidence is varied from 0° to 30°. Note the maximum echo width level is approximately 0 dBm. This level changes with frequency, as the electrical size of the bulkhead changes. The maximum level can be used as a reference
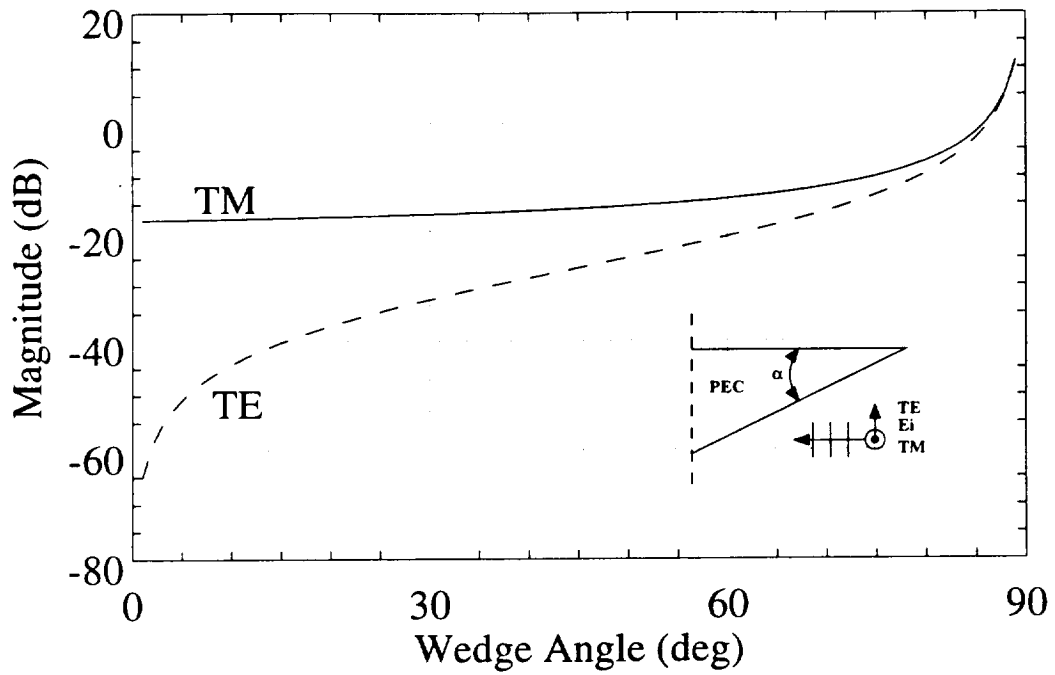
48

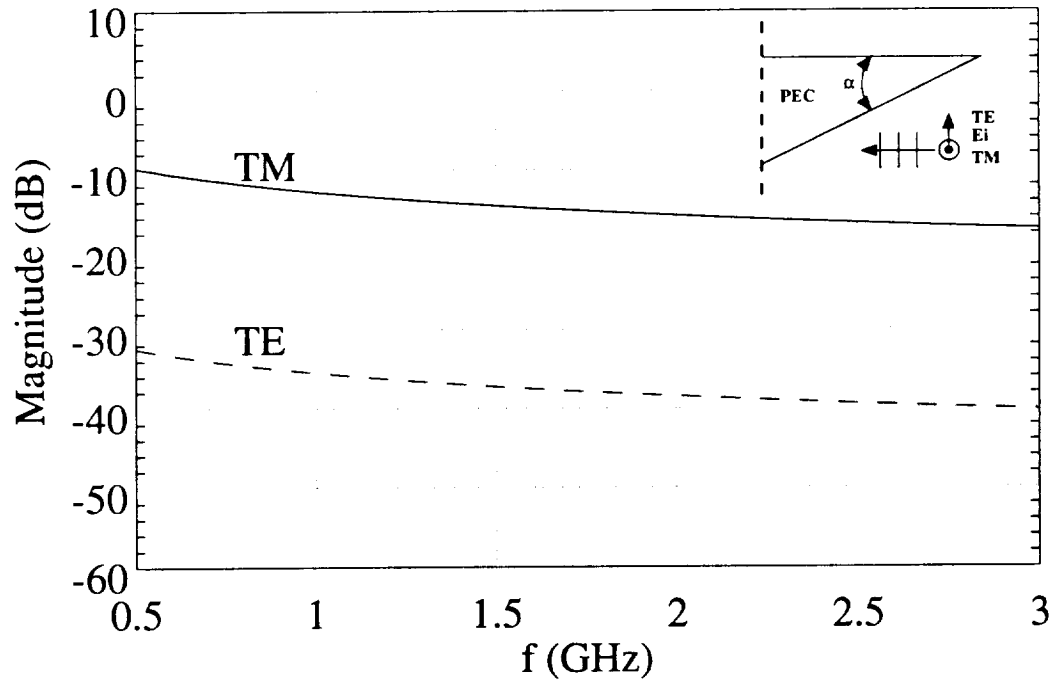Figure 4.5: Magnitude of the diffracted field of an infinite PEC wedge, $f = 3$ GHz, $0°$ incidence.

Figure 4.6: Echo Widths for an infinite PEC wedge, $15°$ wedge angle, $0°$ incidence.
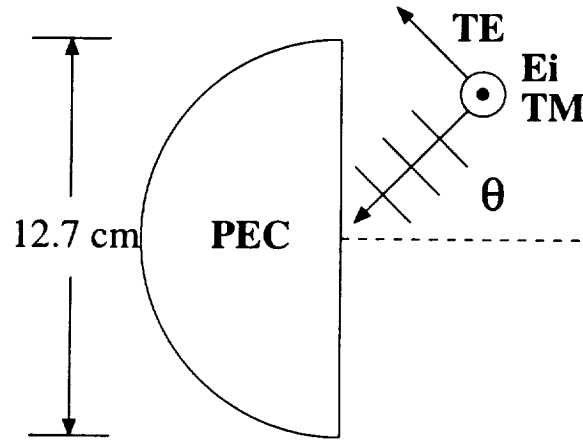
Figure 4.7: Planar bulkhead geometry illustrating angle of incidence.

when considering the effects of rotating a conducting planar bulkhead with dielectric skin.

To study the tilt angle θ_r of the planar bulkhead with dielectric skin, consider Figure 4.9. The dielectric skin has an approximate thickness of .3175 cm with $\epsilon_{r,skin} =$ 4. Figures 4.10 and 4.11 illustrate backscatter echo widths for rotation angles of $\theta_r = 10°$, $20°$, and $30°$ for TM and TE polarizations, respectively. The echo width levels are similar to the levels of the bulkhead in free space. The maximum echo width level of the rotated bulkhead geometry returns to the maximum level of the bulkhead in free space for rotation and incidence angles in the range $0°$ to $30°$. This may indicate that rotation of the bulkhead is not an effective method of reducing backscatter.

4.2.3 Bulkhead Junction Blending

In the first section of this chapter, it was shown that the wedge shaped conducting bulkhead had lower echo width levels over the frequency range of interest than did the planar or circular conducting bulkheads. These lower levels are a result of the wedge shape bulkhead providing smoother shape discontinuities than the planar and circular geometries.

Based upon these preliminary results, three junction blending techniques are considered in shaping the junction between the wedge and the bulkhead as shown in
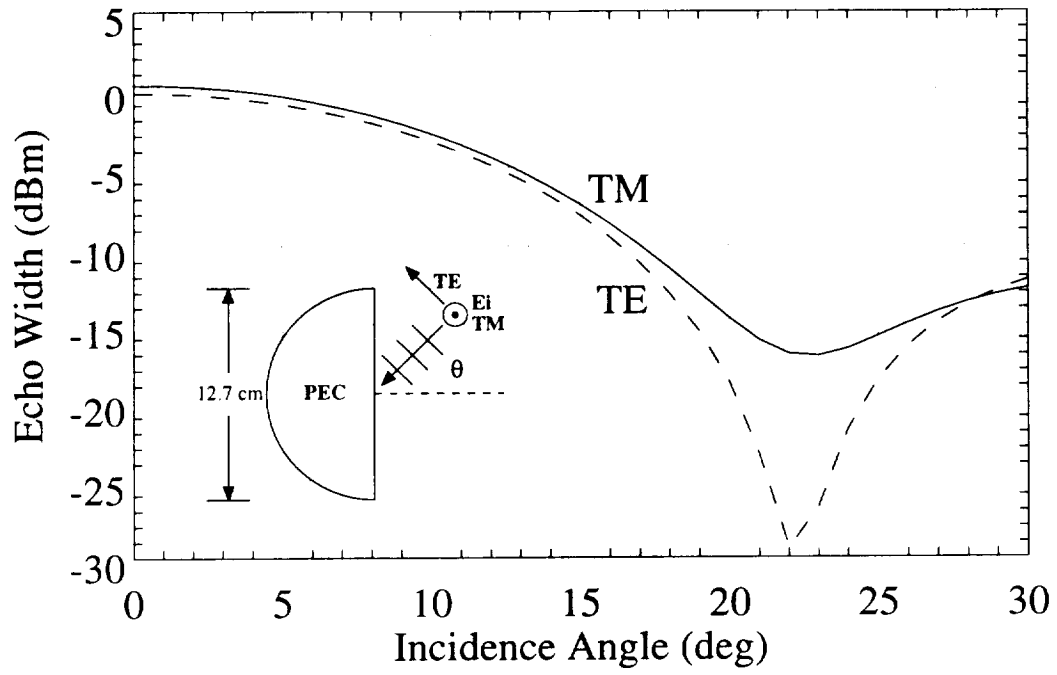
Figure 4.8: Backscatter echo widths of the planar bulkhead with respect to angle of incidence, $f = 3$ GHz.
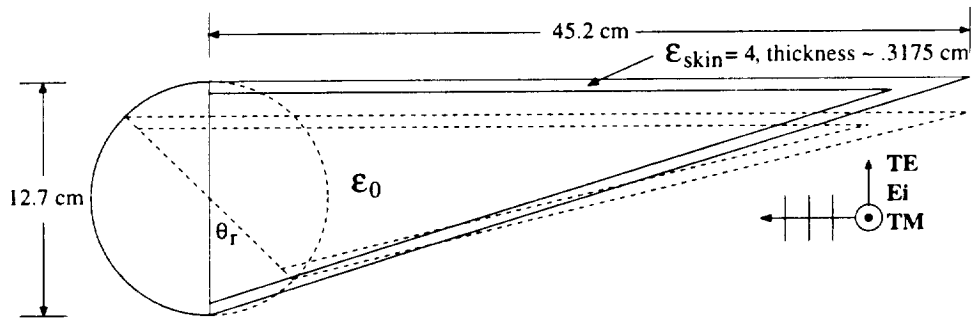

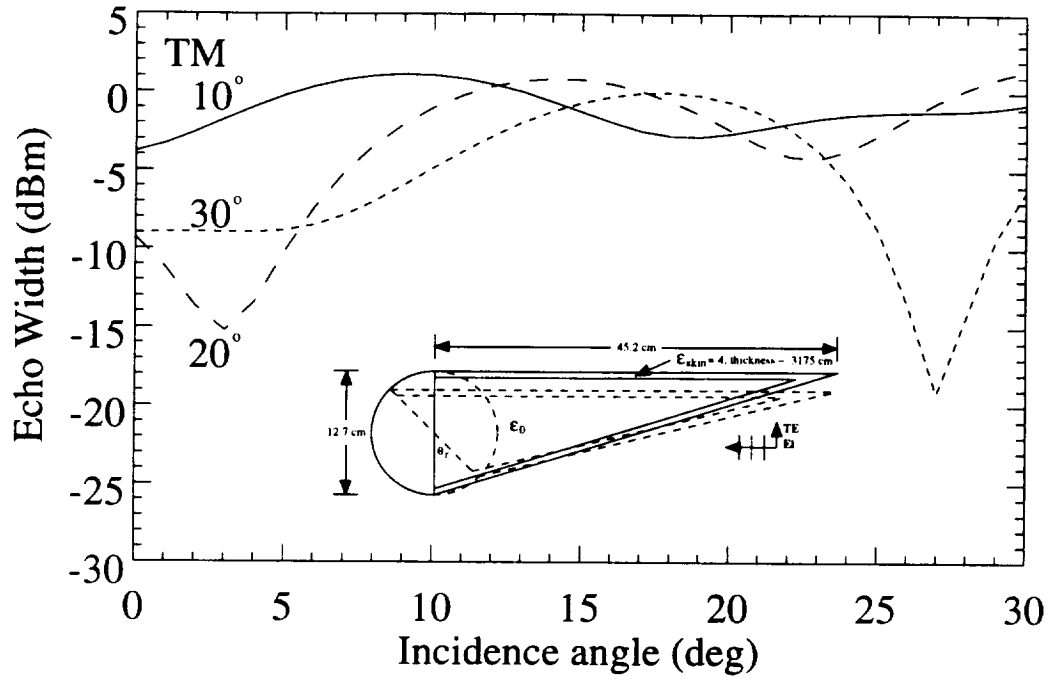Figure 4.9: Planar bulkhead geometry illustrating angle of rotation θ_r.

Figure 4.10: Echo widths of rotated planar bulkhead geometry with TM polarization. f = 3 GHz. θ_r=10° - solid, 20° - long dashed, 30° - short dashed.

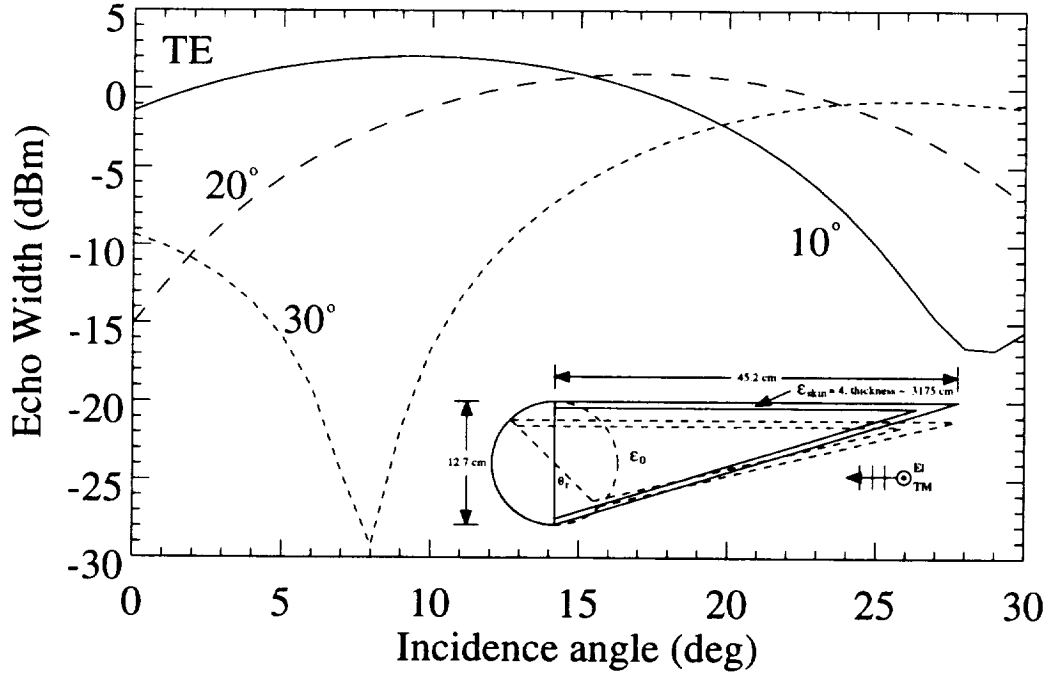Figure 4.11: Echo widths of rotated planar bulkhead geometry with TE polarization. f = 3 GHz. θ_r=10° - solid, 20° - long dashed, 30° - short dashed.
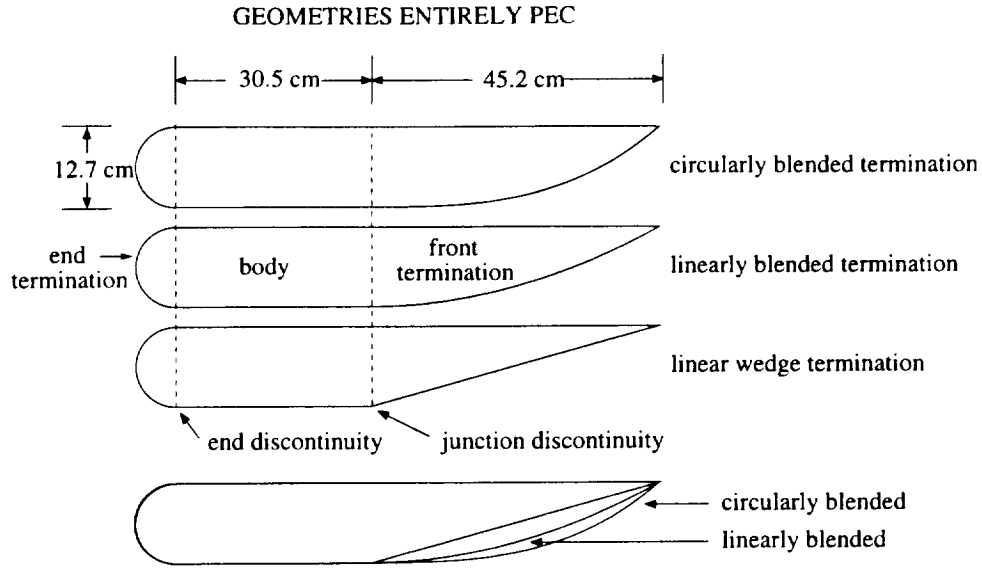
GEOMETRIES ENTIRELY PEC

Figure 4.12: Three blended termination types.

Figure 4.12. The geometry names that are used to differentiate between the three terminations tips are the circularly blended termination, the linearly blended termination, and the linear wedge termination. The geometries consist of a circular end cap, a rectangular body, and a termination tip. In each case, the body of the bulkhead is elongated so that scattering from the tip, junction, and endcap can be isolated and studied using time domain analysis.

Swept frequency calculations for each of the three geometries are shown in Figures 4.13 through 4.15. The three scattering mechanisms that appear as ripples in the transient scattering signature(s) are the front termination ($\simeq$-3 ns), the bulkhead junction (0 ns), and the end termination ($\simeq$2-4 ns).

Figures 4.16 through 4.18 contain the extracted results of the junction alone. The extracted results are useful as they provide frequency domain information of the bulkhead junction independent of other scattering mechanisms. The linearly and circularly blended junctions are more effective in providing lower scattering levels over the frequency range of interest than the linear wedge junction. This is due to the circular and linear blended junctions providing much smoother transitions between the tip and junction than the linear wedge geometry.
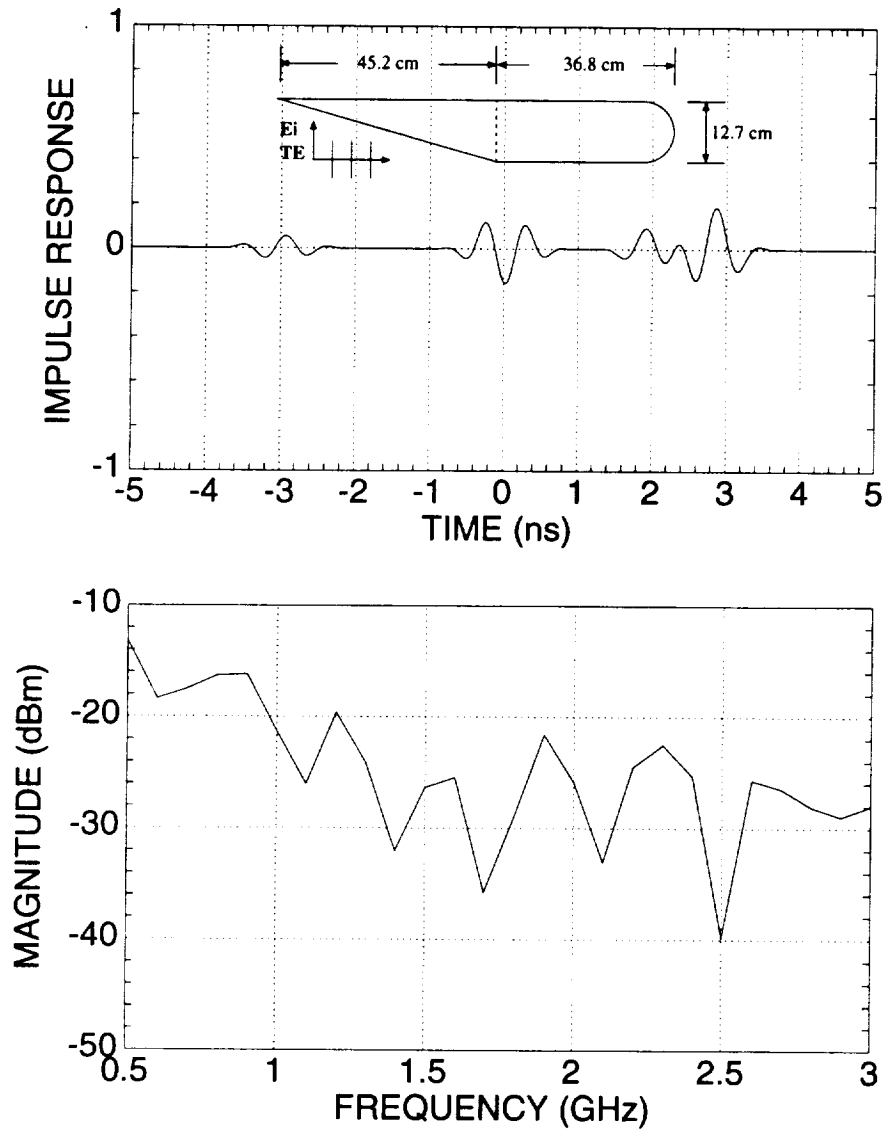
Figure 4.13: Transient and frequency domain scattering signatures for the linear wedge termination geometry with TE illumination.
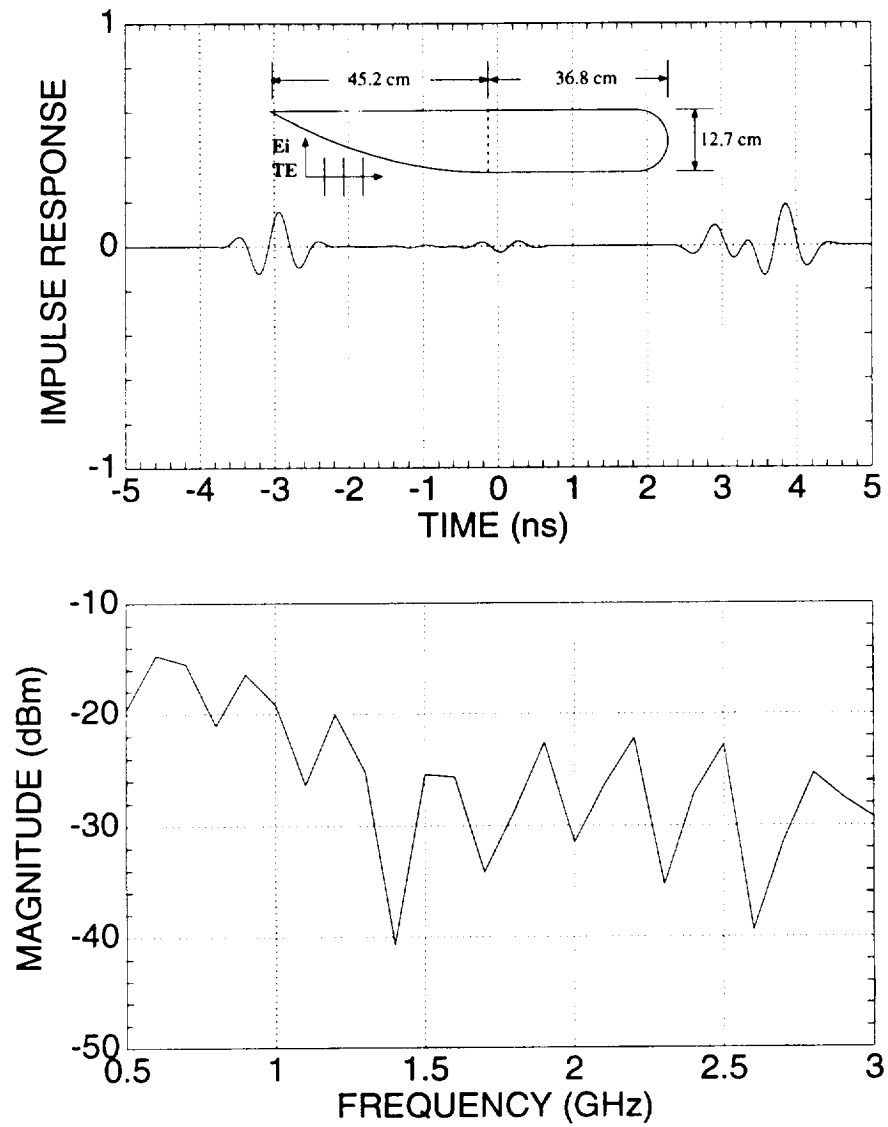
Figure 4.14: Transient and frequency domain scattering signatures for the linearly blended termination geometry with TE illumination.
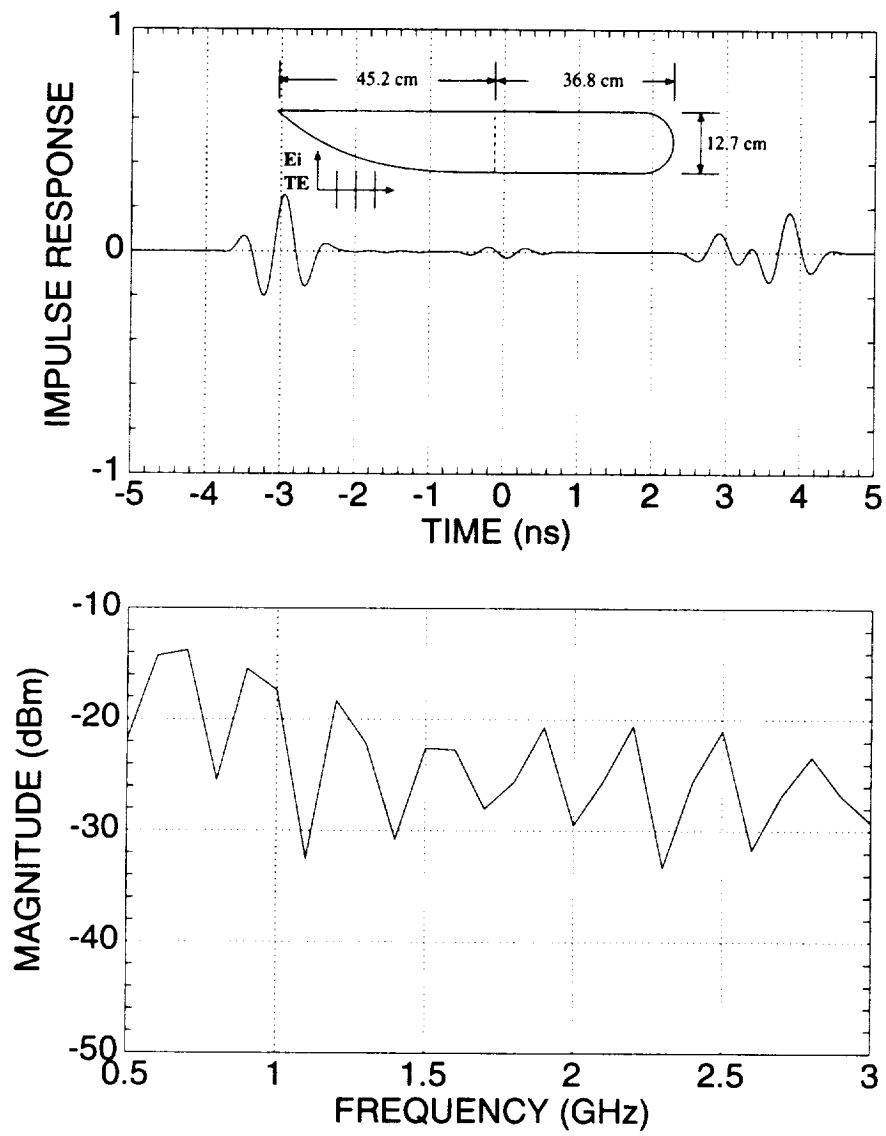
Figure 4.15: Transient and frequency domain scattering signatures for the circularly blended termination geometry with TE illumination.

Figure 4.16: Extracted tip scattering levels for the linear wedge termination junction with TE illumination.

Figure 4.17: Extracted tip scattering levels for the linearly blended termination junction with TE illumination.

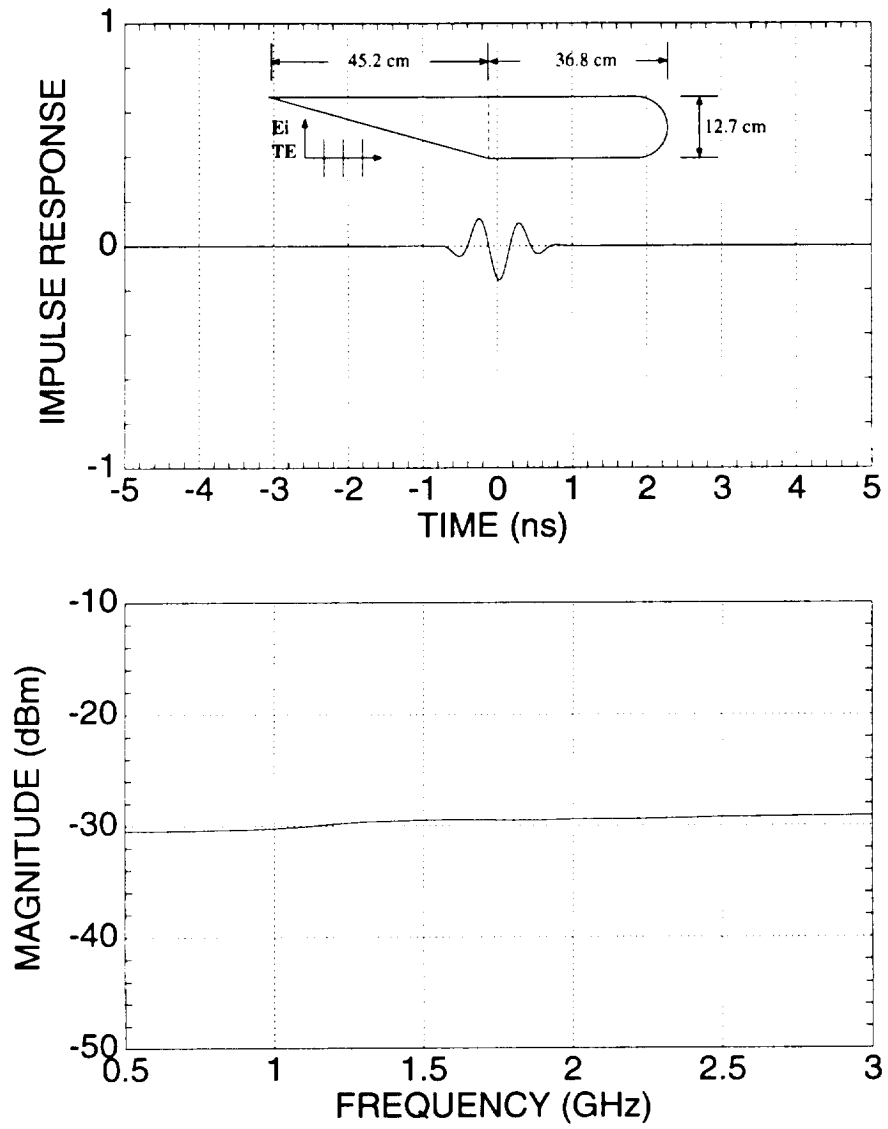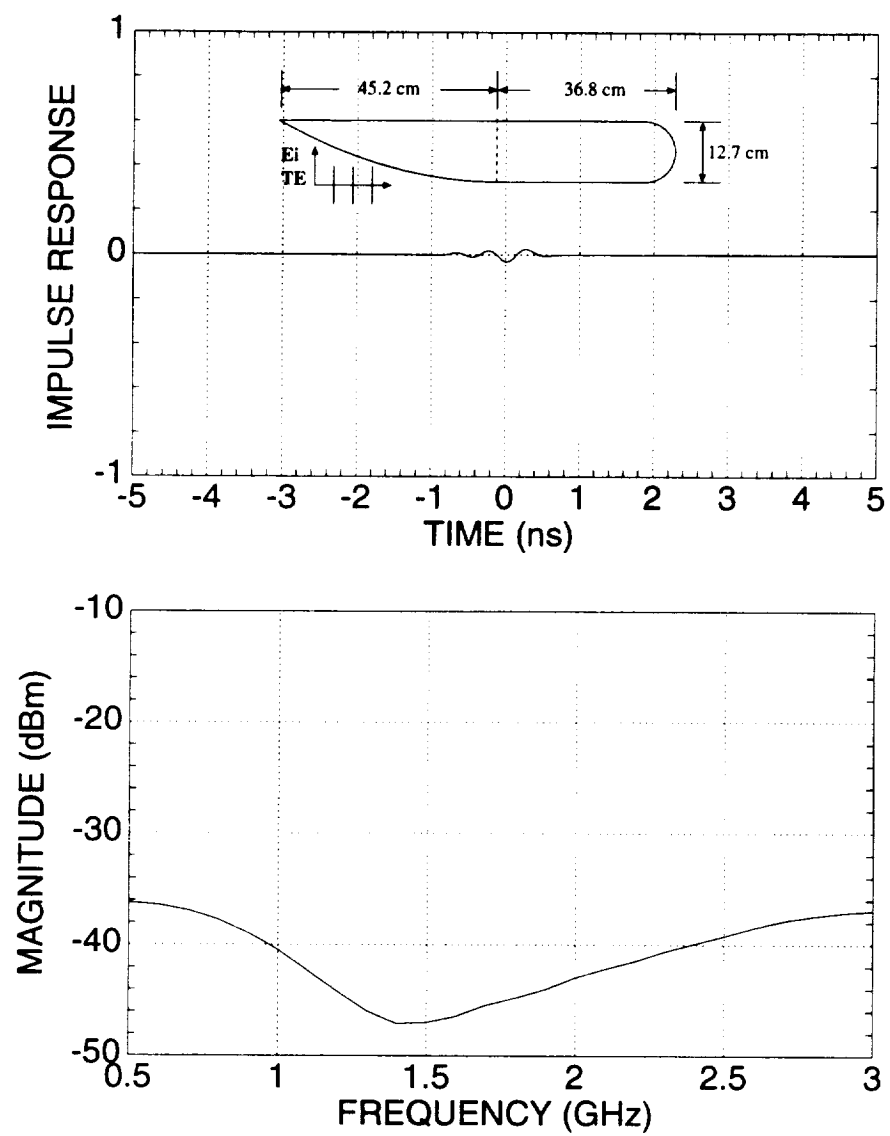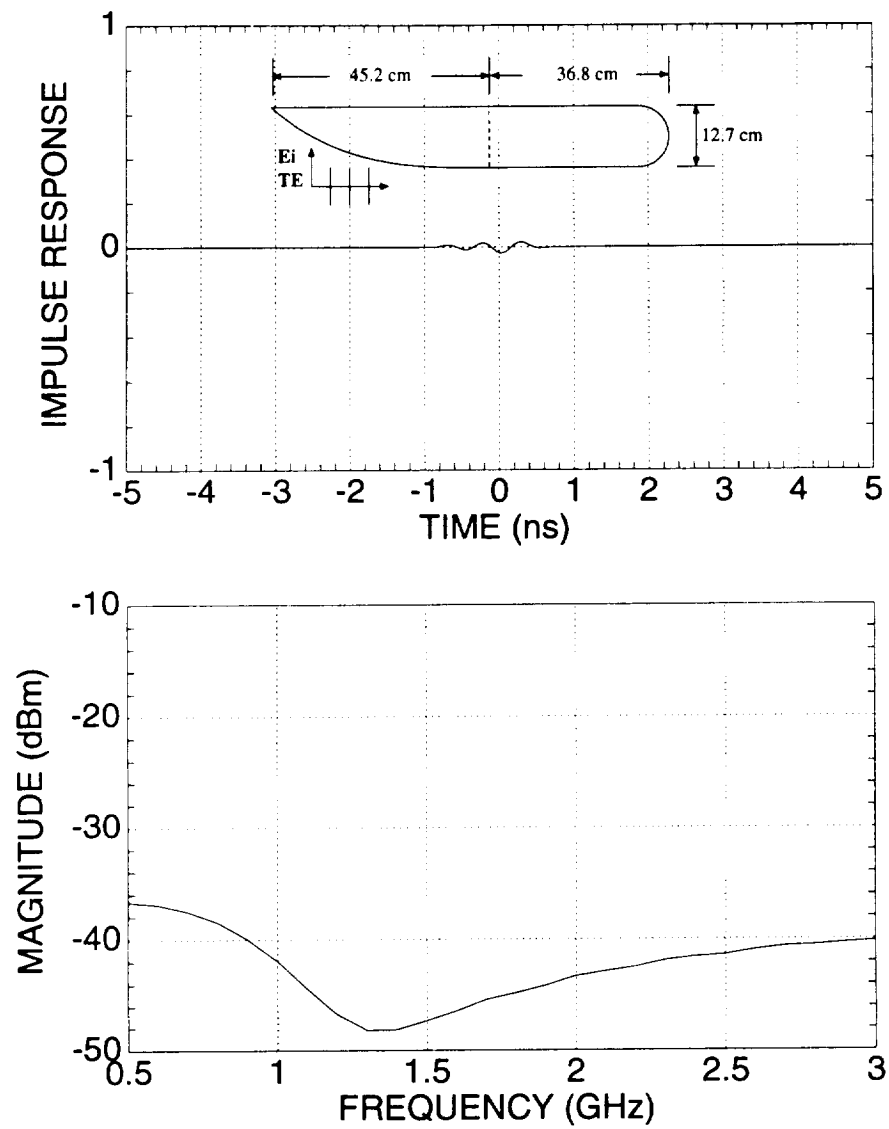Figure 4.18: Extracted tip scattering levels for the circularly blended termination junction with TE illumination.
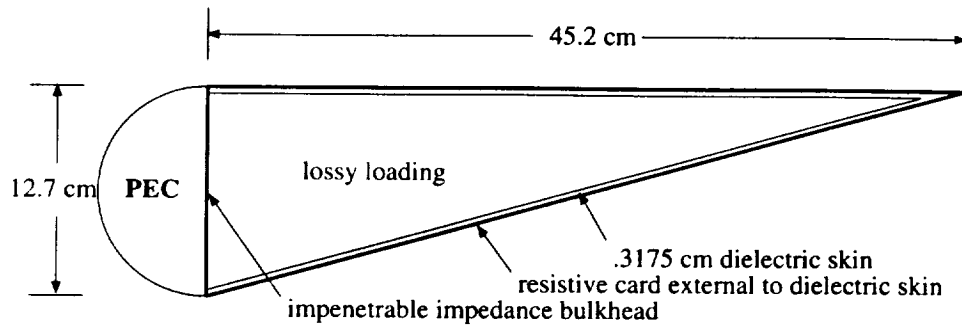
Figure 4.19: Planar conducting bulkhead geometry.

4.3 Material Considerations

The previous section explored methods of altering the conducting bulkhead geometries to lower the scattered field levels. This section will address the effects of dielectric materials and resistive cards when combined with a conducting bulkhead.

An illustration of the geometry for analysis is shown in Figure 4.19. As indicated by the figure, there are several components of the geometry that effect its scattering signature: the dielectric skin; the internal material loading; and the placement of resistive cards and impedance surfaces. Each of these components will be discussed in the following sections.

4.3.1 Dielectric Skin

Wedge Angle

¿From Figure 4.5 it was concluded that wedge angle does not significantly effect the magnitude of the diffracted field from a conducting wedge when the wedge angle remains small. When considering a penetrable dielectric tip, however, wedge angle is of greater importance as will now be demonstrated.

Figure 4.20 illustrates a model of the dielectric skin that will be incorporated with the bulkhead geometries. The size and shape of the skin may be constrained by other considerations. For now the length of the wedge formed by the skin and the thickness of the skin will be held constant to investigate the effects of varying the wedge angle. The backscatter characteristics for wedge angles of 10°, 20°, and 30°
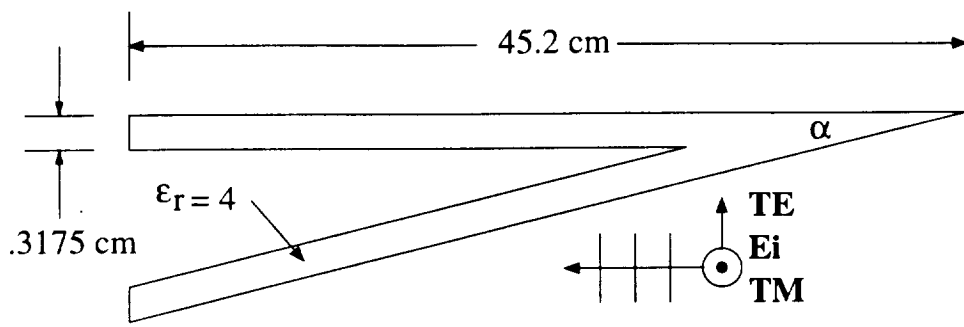
60

Figure 4.20: Dielectric skin model.

are shown in Figures 4.21 and 4.22 for TM and TE polarizations, respectively. The results indicate that it is desirable to maintain a small wedge angle when considering a penetrable termination tip to keep backscatter levels as low as possible over the desired frequency range.

Polarization and Angle of Incidence

Polarization and angle of incidence also have an effect on the return from a dielectric slab. Consider the geometry shown in Figure 4.23. Figures 4.24 and 4.25 illustrate the transmission and reflection characteristics of a dielectric slab as a function of angle of incidence for TM and TE polarization, respectively.

The transmission coefficient of the slab is of particular interest, as it is an indication of the amount of energy that penetrates the slab. The results show that, for both polarizations, as the angle of incidence approaches 90° (grazing), the slab rapidly becomes less transmissive. This is an important point. Consider Figure 4.26. The dielectric skin consists of two thin dielectric slabs combined into a wedge shape. When considering incidence angles near 0°, θ_i (see Figure 4.23) with respect to the upper slab approaches 90°, with θ_i for the lower slab having an approximate value of 75°.

Frequency and Relative Dielectric Constant

Figures 4.27 through 4.30 show the effects of varying frequency and dielectric constant. For TM polarization, the slab becomes less transmissive as the electrical thickness

61

Figure 4.21: Extracted tip scattering levels for dielectric skin geometry, $\epsilon_{r,skin} = 4$, TM polarization. $\alpha=10°$ - solid, 20° - dotted, 30° - dashed.
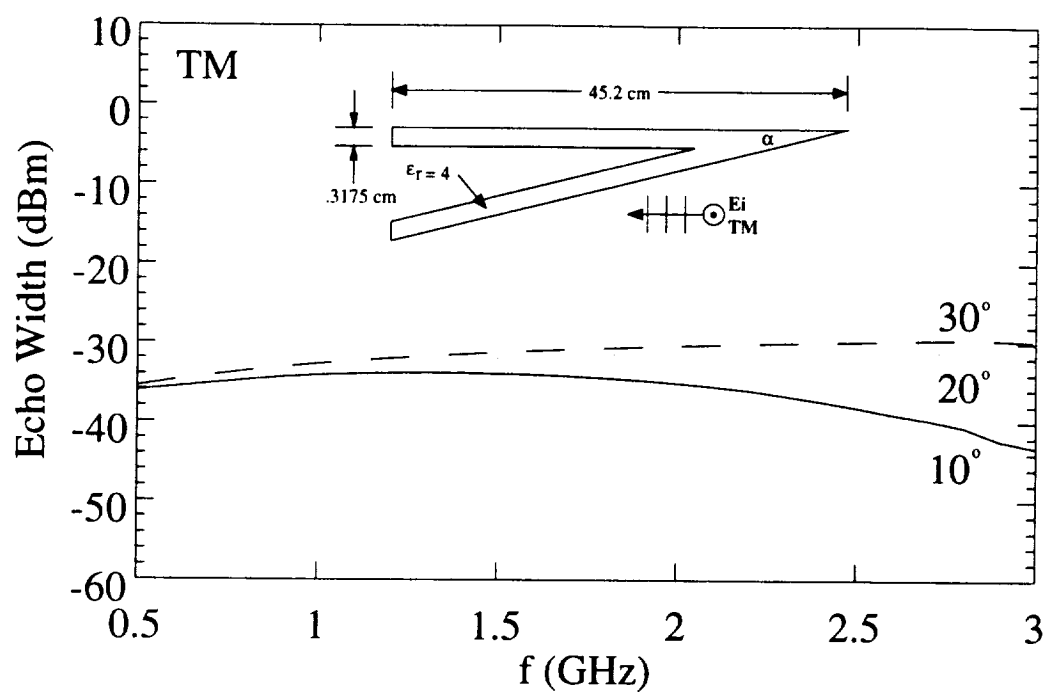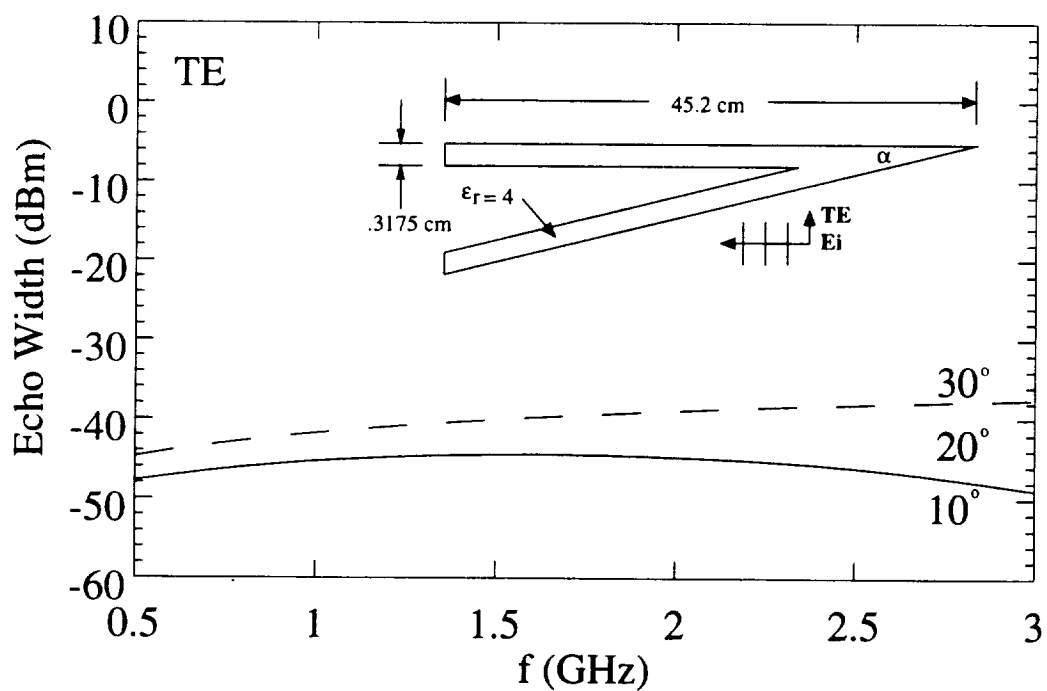

Figure 4.22: Extracted tip scattering levels for dielectric skin geometry, $\epsilon_{r,skin} = 4$, TE polarization. $\alpha=10°$ - solid, 20° - dotted, 30° - dashed.
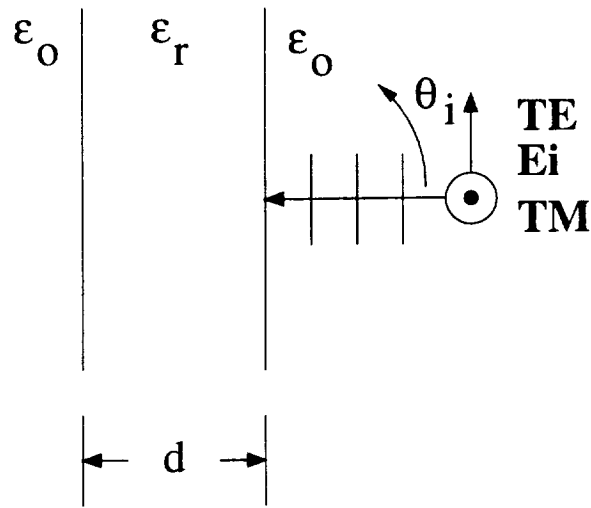
Figure 4.23: Dielectric slab geometry.
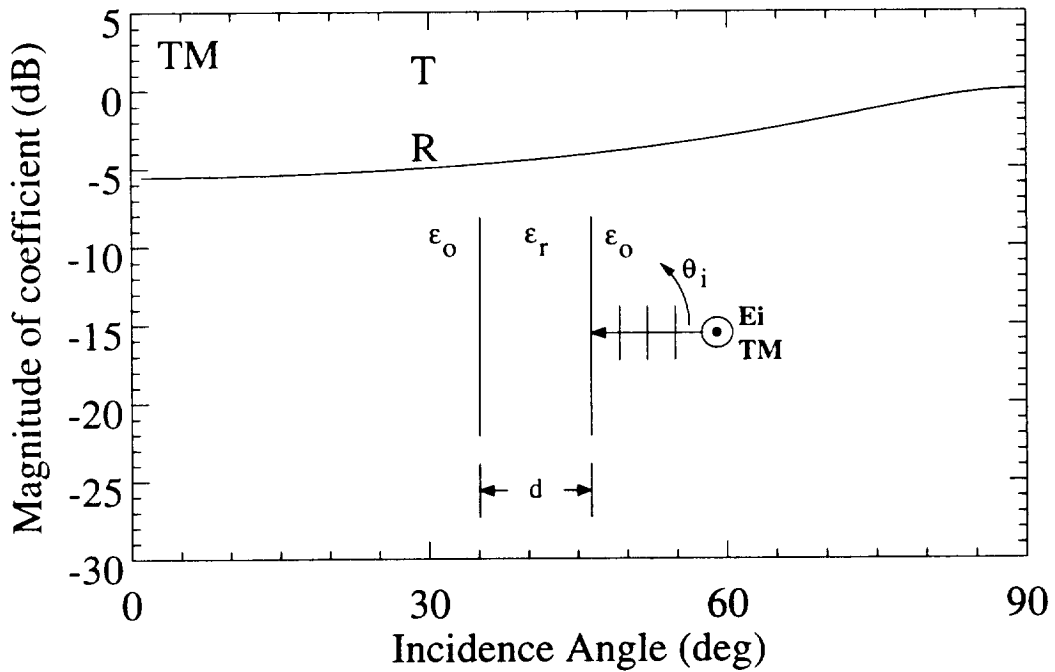
Figure 4.24: Magnitude of reflection and transmission coefficients for a .3175 cm thick dielectric slab in free space. $f = 3$ GHz, $\epsilon_{r,slab} = 4$, TM polarization.

Figure 4.25: Magnitude of reflection and transmission coefficients for a .3175 cm thick dielectric slab in free space. $f = 3$ GHz, $\epsilon_{r,slab} = 4$, TE polarization.

Figure 4.26: Dielectric skin represented as two individual dielectric slabs.

Figure 4.27: Magnitude of reflection and transmission coefficients for a .3175 cm thick dielectric slab in free space. $\epsilon_{r,slab} = 4$, TM polarization, 75° incidence.
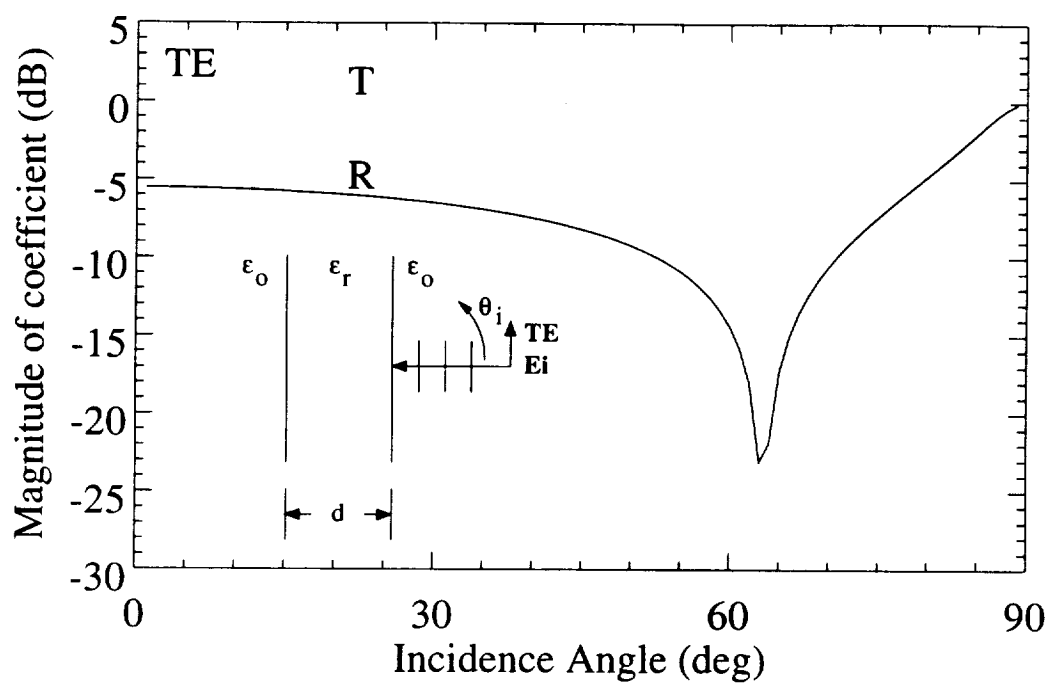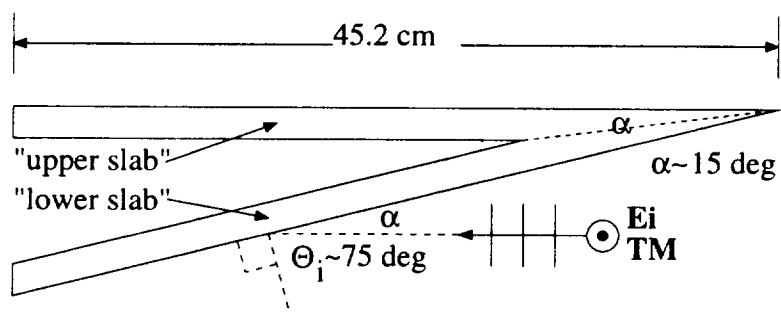
of the slab is increased. The slab also becomes less transmissive when the relative dielectric constant of the slab is increased. For TE polarization with an incidence angle of 75°, the slab remains highly transmissive in the given frequency and relative dielectric ranges. If the incidence angle of the slab approaches 90° (grazing), the magnitude of the (TE) transmission coefficient will decrease more dramatically as frequency is increased, as well as when the relative dielectric constant of the slab is increased.

The next section considers a geometry consisting of a wedge shaped dielectric skin with interior material loading combined with the conducting planar bulkhead geometry (see Figure 4.19). It is found that backscatter is significantly reduced by loading the region between the conducting bulkhead and the dielectric skin with a lossy dielectric material.

4.3.2 Internal Loading Parameters

A set of ϵ_r values of interest for use in internally loading the wedge geometry of Figure 4.19 are shown in Table 4.1. The dielectric skin is assumed to take on a value
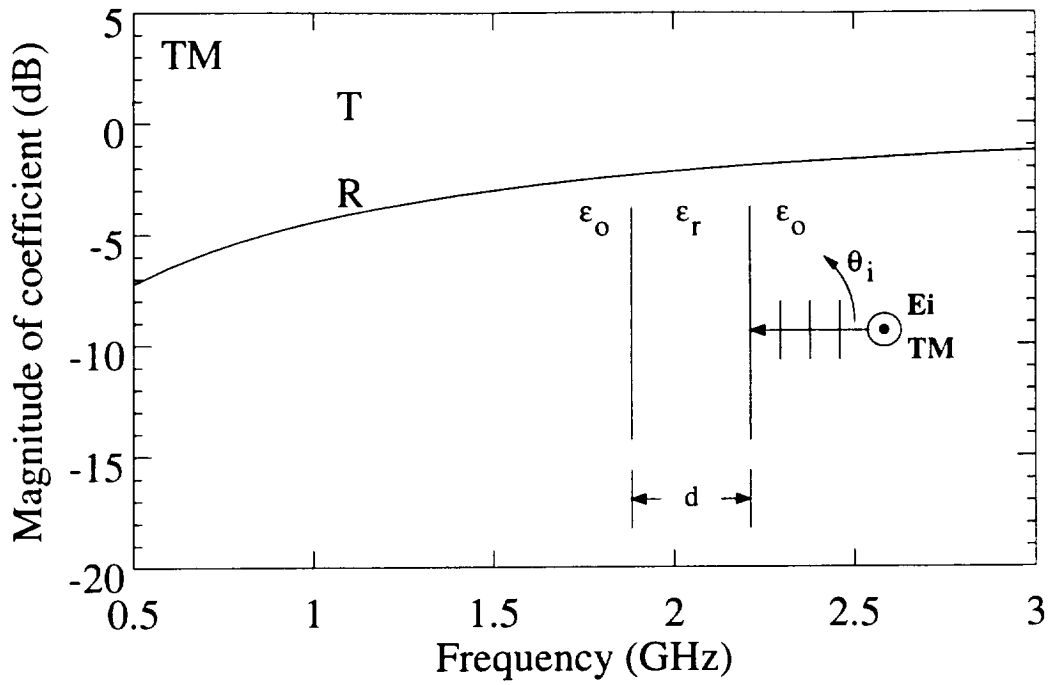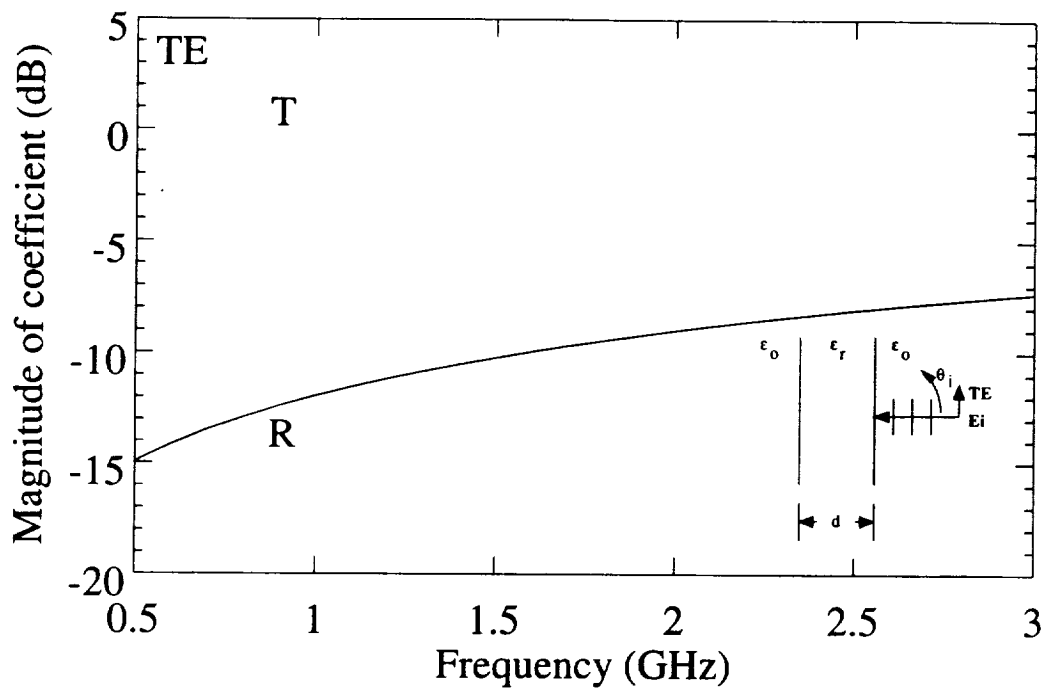
Figure 4.28: Magnitude of reflection and transmission coefficients for a .3175 cm thick dielectric slab in free space. $\epsilon_{r,slab} = 4$, TE polarization, 75° incidence.

Figure 4.29: Magnitude of reflection and transmission coefficients for a .3175 cm thick dielectric slab in free space. $f = 3$ GHz, TM polarization, 75° incidence.
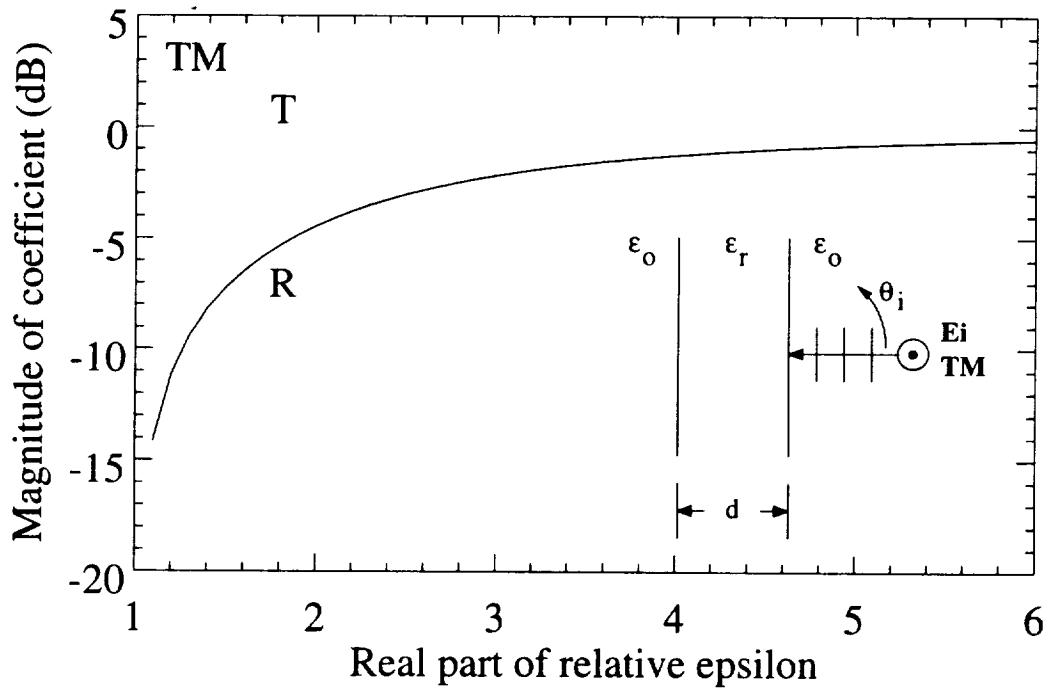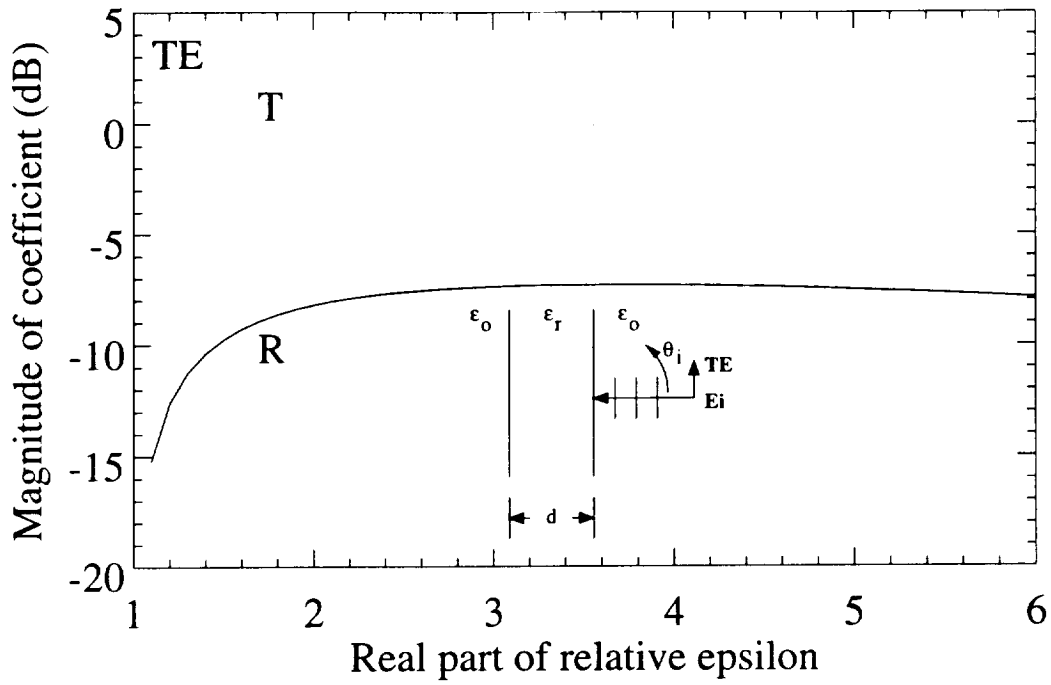
Figure 4.30: Magnitude of reflection and transmission coefficients for a .3175 cm thick dielectric slab in free space. $f = 3$ GHz, TE polarization, 75° incidence.

of $\epsilon_{r,skin} = 4$ or 6. Each internal loading parameter was evaluated for both TM and TE polarizations with each of the two values of skin dielectric constant. It was found for TM polarization that a skin dielectric constant of $\epsilon_{r,skin} = 6$ was more effective in lowering the backscatter levels over the frequency range of interest. The internal loadings with the lowest backscatter levels are illustrated in Figures 4.31 and 4.32.

To further reduce backscatter levels at low frequencies, a 500Ω impedance is applied to the flat portion of the conducting bulkhead, with results shown in Figures 4.33 and 4.34. Implementation of this impedance surface, however, may not be realistic.

Originally, it was thought that internally loading the interior wedge region with the material with the largest loss tangent would be the most effective in reducing backscatter. The previous results do not indicate that this is the case.

Two possible reasons why the material with the largest loss tangent was not the most effective material in reducing backscatter are the following. First, upon inspection of Table 4.1, materials with the largest loss tangent also have the largest value of $|\epsilon_r|$, which effects the transmission and reflection characteristics of the material.

Table 4.1: Estimated lossy foam parameters.

Re(ϵ_r)	Im(ϵ_r)	Loss tangent
23.3	-16.3	.70
18.8	-9.01	.48
14.9	-5.24	.35
11.8	-3.16	.27
7.50	-1.20	.16
6.00	-0.70	.12
4.80	-0.40	.08

Figure 4.31: Backscatter characteristics of the simple wedge geometry with internal loading of ϵ_r=14.9-j5.24, $\epsilon_{r,skin}$ = 6, 0° incidence.

Figure 4.32: Backscatter characteristics of the simple wedge geometry with internal loading of ϵ_r=11.8-j3.16, $\epsilon_{r,skin}$ = 6, 0° incidence.

Figure 4.33: TM Backscatter characteristics of the simple wedge geometry with internal loading of ϵ_r=11.8-j3.16, $\epsilon_{r,skin}$ = 6, 0° incidence, with 500Ω impedance on flat portion of conducting bulkhead.
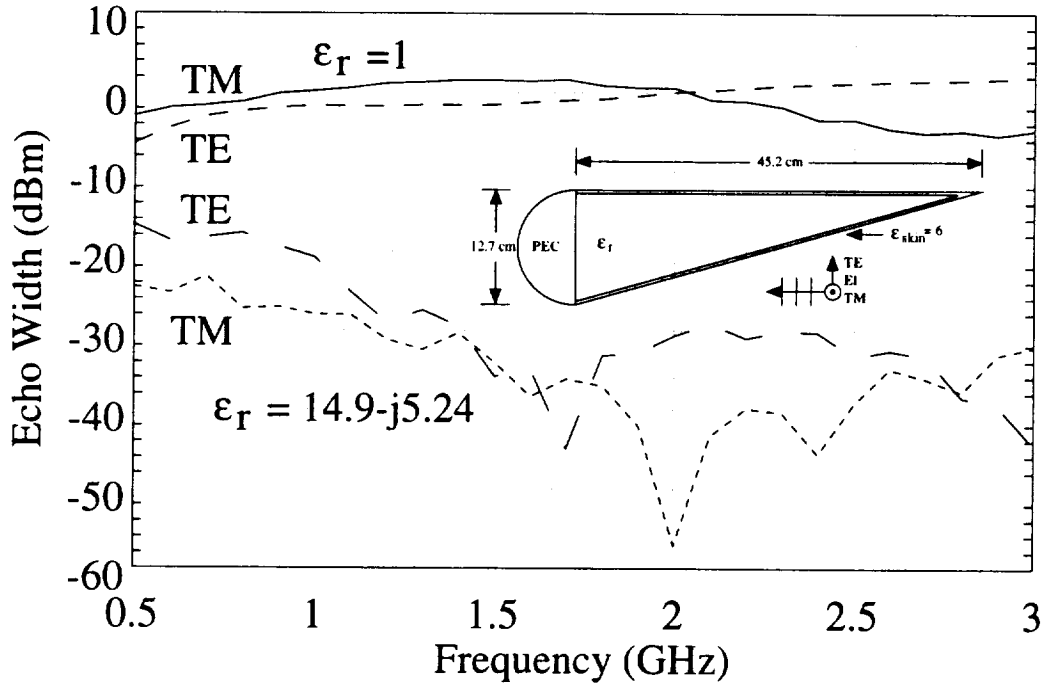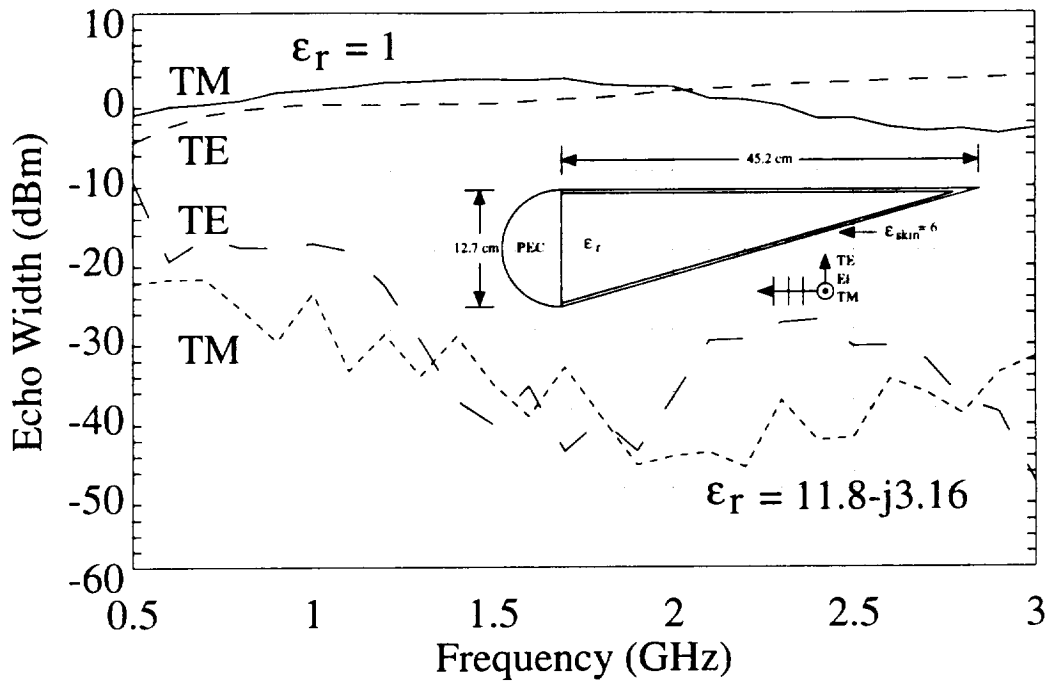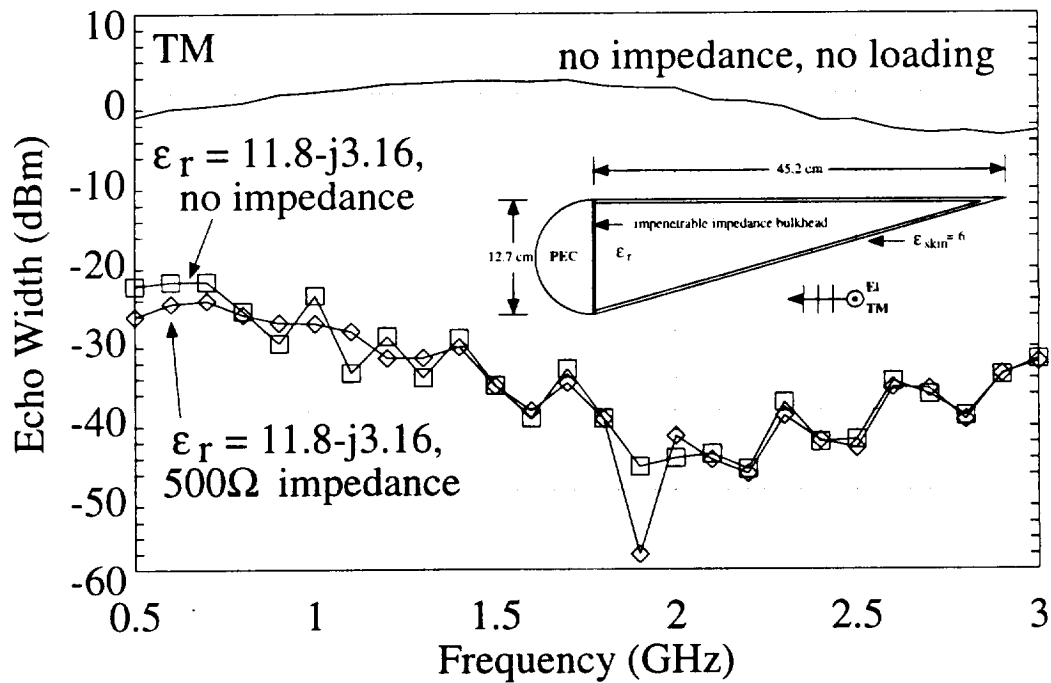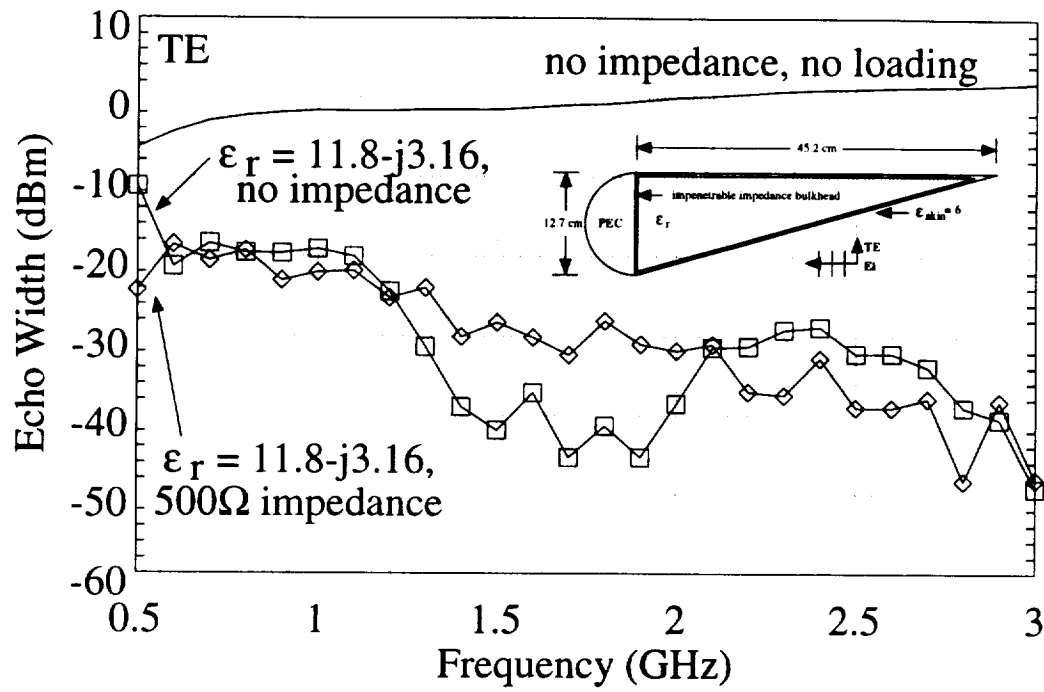
Figure 4.34: TE Backscatter characteristics of the simple wedge geometry with internal loading of ϵ_r=11.8-j3.16, $\epsilon_{r,skin}$ = 6, 0° incidence, with 500Ω impedance on flat portion of conducting bulkhead.

Secondly, the change in scattered field behavior caused by the loaded interior region is considered in the presence of the dielectric skin. The interior region's effects on the scattered field in the presence of the dielectric skin may be not be the same as when the interior region is considered independently.

4.3.3 Resistive Cards and Impedance Surfaces

Another method that can be used to influence the scattered field levels of a structure like that of Figure 4.19 is the placement of complex impedance surfaces. The simplest impedance surface would be a resistive (purely real) surface. Two possible locations for placement of such a surface are the conducting bulkhead or the exterior of the dielectric skin. The next sections address the effects of utilizing these surfaces.

Resistive Cards on External Surface of Dielectric Skin

Figures 4.35 and 4.36 compare the backscatter characteristics of a constant resistive card on the surface of the dielectric skin with that of a tapered resistive card for TM

TM

3-3k $\Omega/\square$

350 $\Omega/\square$

45.2 cm

3 $\Omega/\square$

3000 $\Omega/\square$

12.7 cm PEC $\varepsilon 0$

$\varepsilon_{skin} = 4$

tapered R-card

Ei
TM

Echo Width (dBm)

Frequency (GHz)
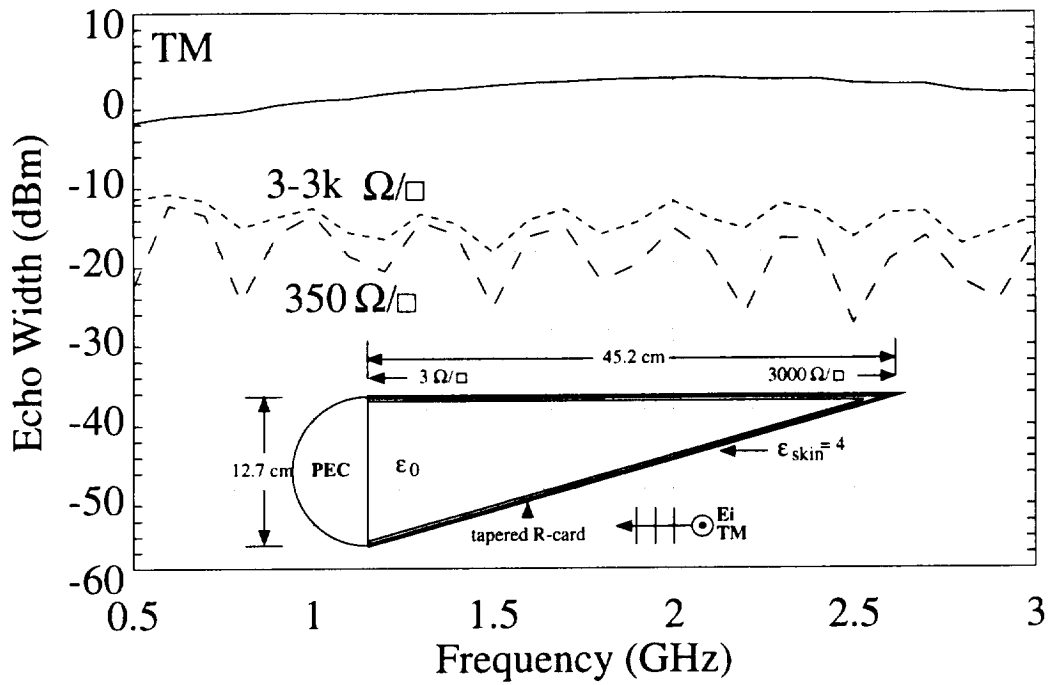
Figure 4.35: Backscatter characteristics of the simple wedge geometry, 0° incidence, TM polarization.

and TE polarizations, respectively. The tapered resistive card is modeled to have a low $\Omega/\square$ value at the conducting portion of the structure, tapered to a value of a few thousand $\Omega/\square$ at the tip.

A resistive card of constant value yields better performance than a tapered resistive card since the card of constant value allows less energy to penetrate the interior region. In contrast, a tapered resistive card provides less scattering at the wedge tip, but allows for greater internal scattering.

To interpret why a resistive card placed on the external surface of the dielectric skin is less effective when considering TE polarization, an infinite resistive card model can be used.

Infinite Resistive Card

Figures 4.37 and 4.38 illustrate the reflection and transmission properties, respectively, for an infinite R-card with 90° (grazing at 0°) being perpendicular to the plane of the card.
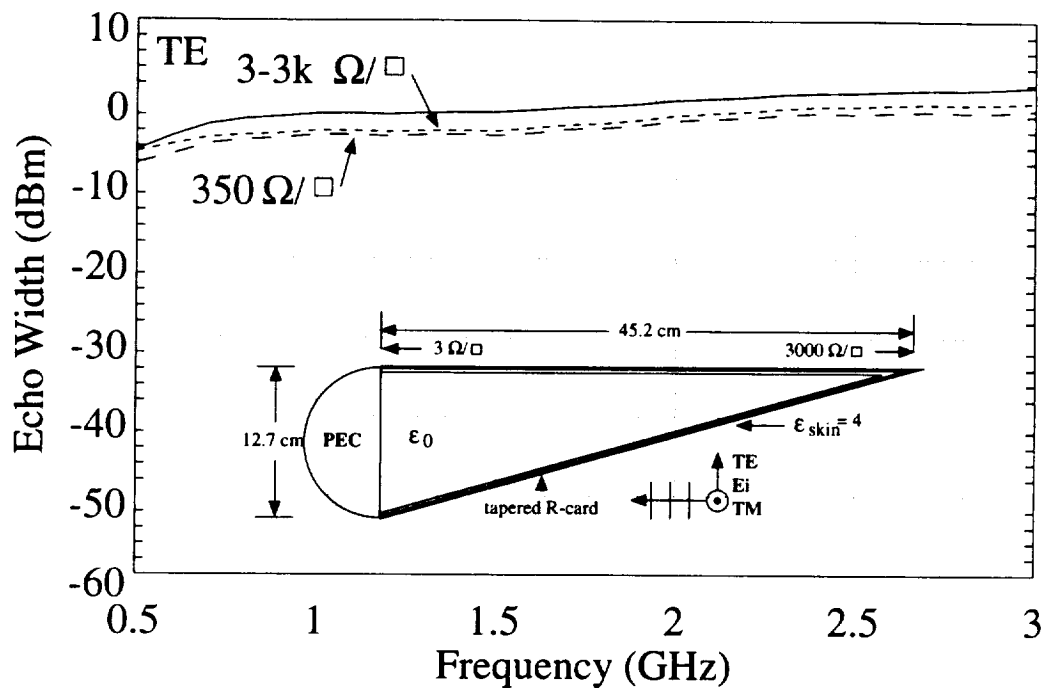
Figure 4.36: Backscatter characteristics of the simple wedge geometry, 0° incidence, TE polarization.
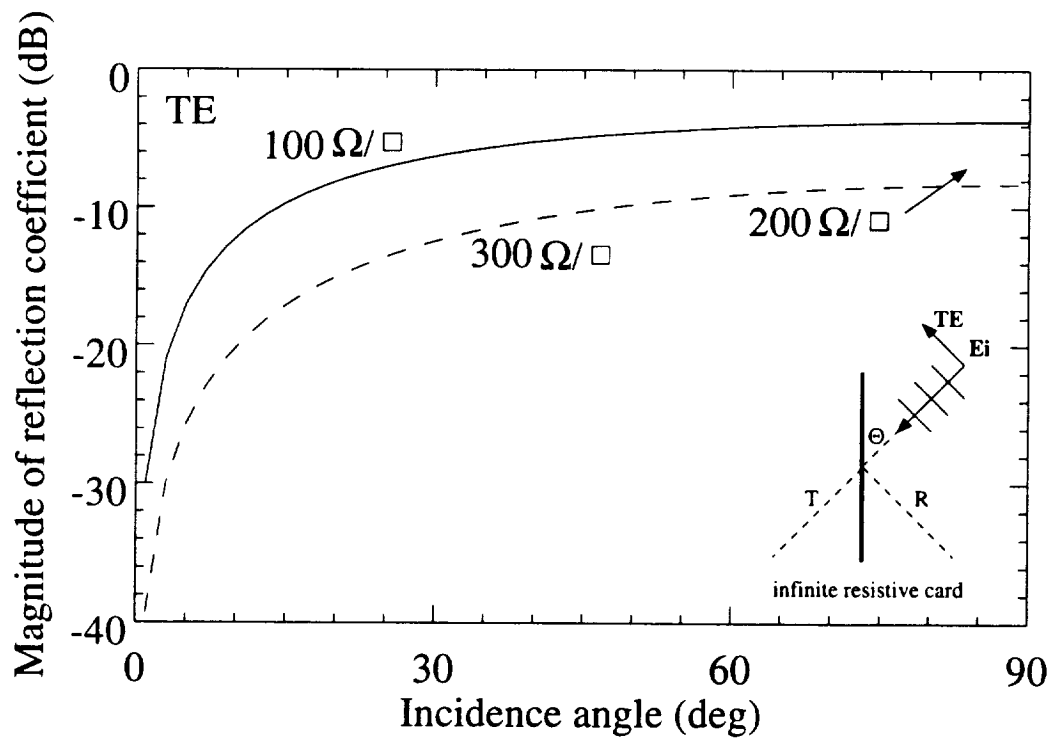
Figure 4.37: Magnitude of the reflection coefficient for an infinite resistive card, TE polarization.
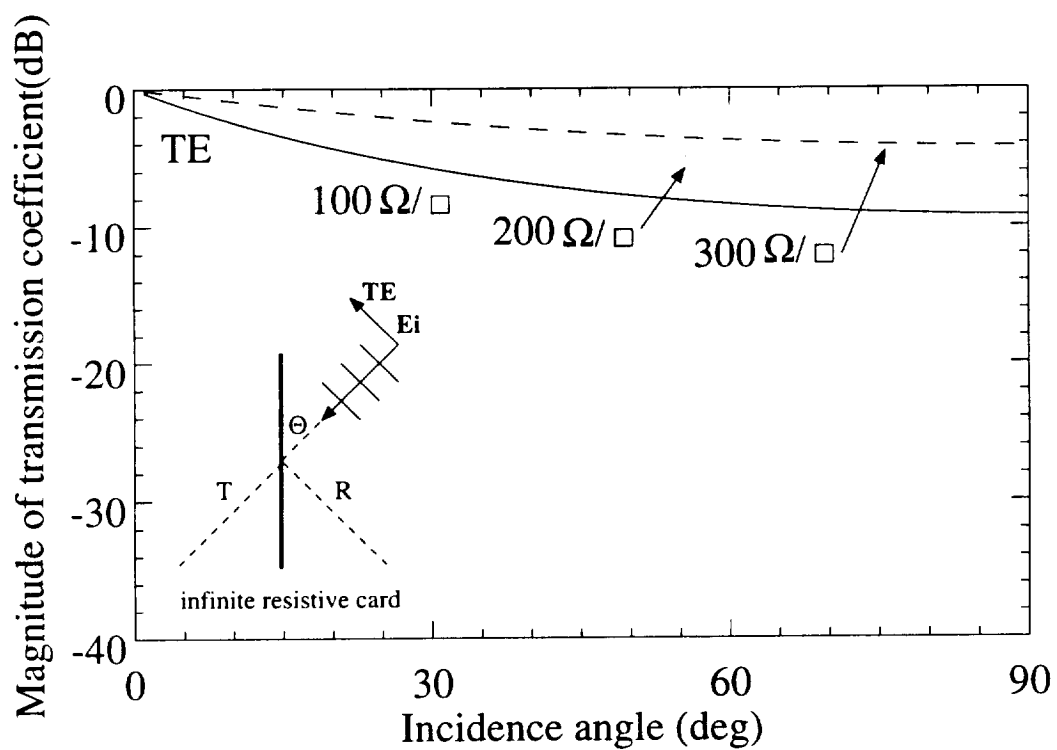
Figure 4.38: Magnitude of the transmission coefficient for an infinite resistive card, TE polarization.
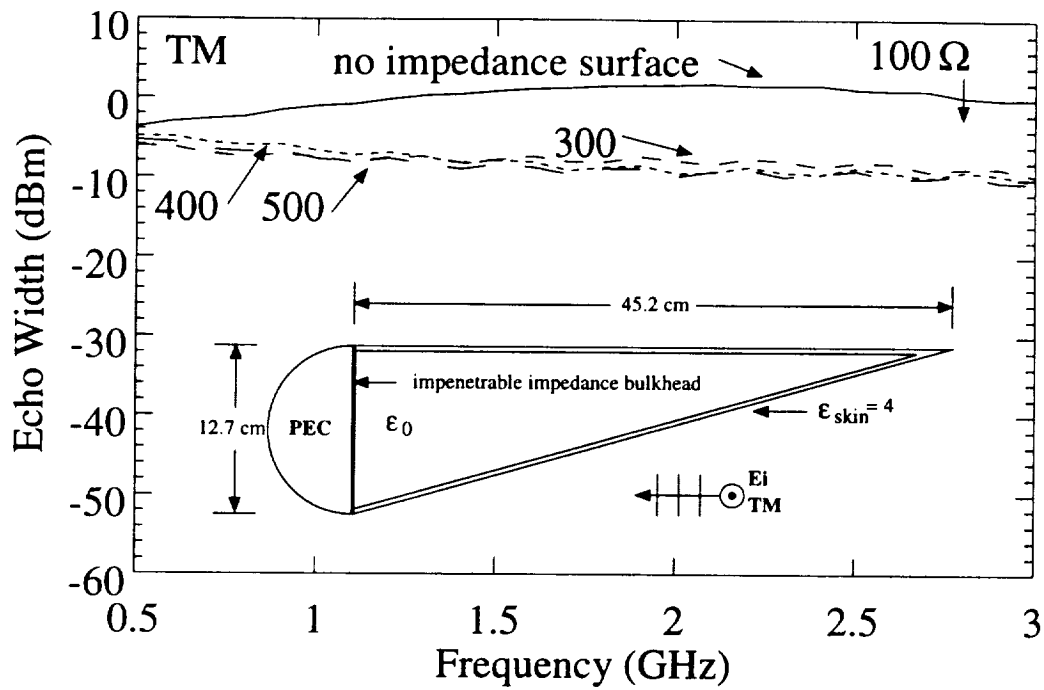
Figure 4.39: Backscatter characteristics of the simple **wedge** geometry with impedance bulkhead, TM polarization.

Figures 4.37 and 4.38 illustrate that as the angle of the incident TE wave approaches grazing (0°), the transmission coefficient is large allowing energy to pass through the card. Thus, both tapered and constant resistive cards placed externally to the dielectric skin have little effect on the scattered field levels when the geometry is illuminated with TE polarization (see Figure 4.36).

Impedance Bulkhead Surface

Figures 4.39 and 4.40 illustrate the behavior of an impedance surface placed on the flat face of the planar bulkhead for TM and TE polarizations, respectively. The results indicate that continuing to increase the value of the impedance surface does not guarantee lower backscatter levels.
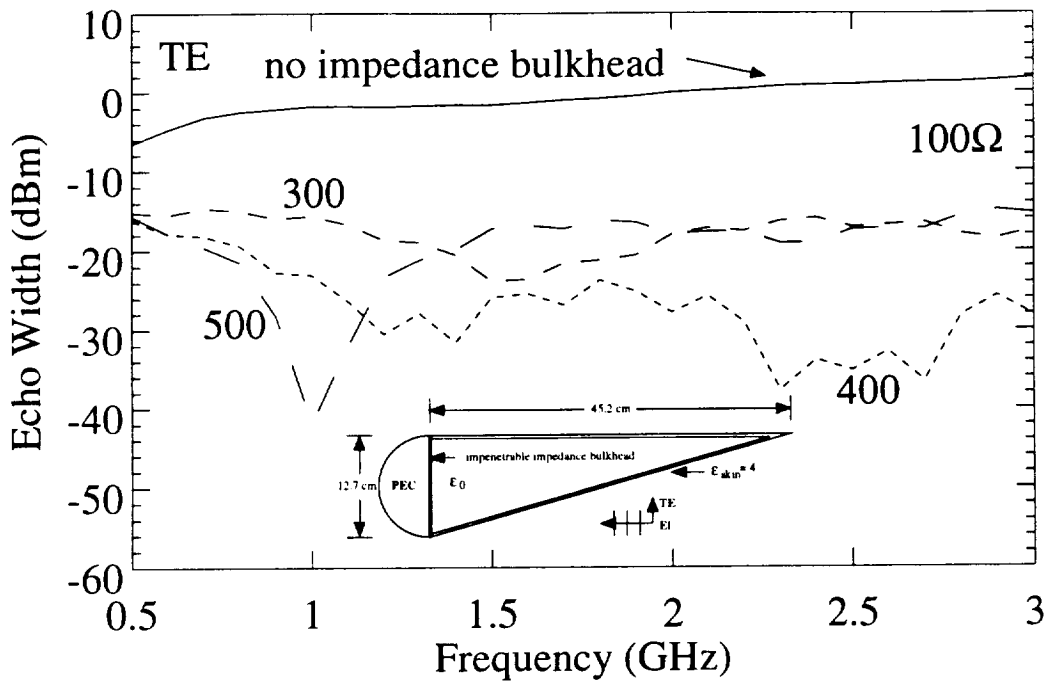
Figure 4.40: Backscatter characteristics of the simple wedge geometry with impedance bulkhead, TE polarization.

4.4 Material Rod Nulling

4.4.1 Dipole Arrays

A demonstrated scattering reduction method is that of dipole array nulling. Dipole array nulling is effective in reducing scattering levels over a substantial bandwidth [12] [13]. Figure 4.41 ([12]) illustrates one example of the reduction possible by placing two co-linear dipole arrays in front of a leading edge model as described by Figures 4.42 and 4.43.

The goal of the following sections is to study the possibility of emulating the effects of lossy dipole arrays using perfect electric conducting or material rods.

4.4.2 Perfect Electric Conducting Rods

An illustration of the geometry(s) under consideration is shown in Figure 4.44. Rectangular rods of various dimensions are placed in front of the conducting bulkhead as shown. There are an infinite number of combinations to explore when considering the number of rods, the rod dimensions, and the x and y location of the rods. As a
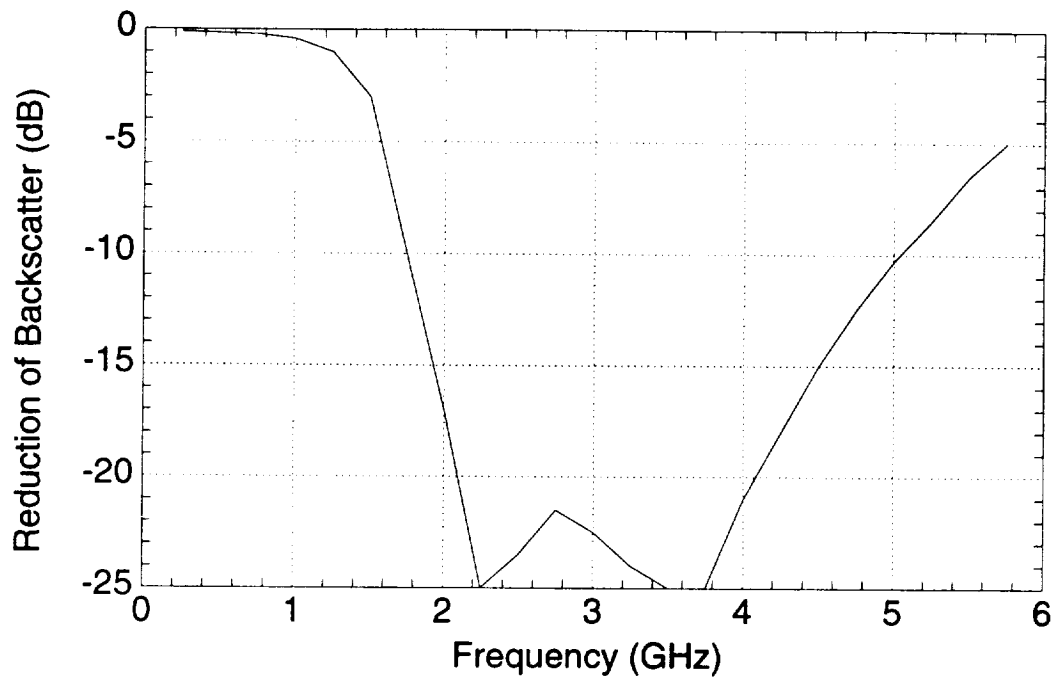
Figure 4.41: Backscatter reduction using loaded dipoles.

ALL DIMS. IN CM

lossy dipoles

4

d = 1

s = .2

"ground plate" rods

Dg = 2.25

FRONT VIEW

SIDE VIEW

"ground plate" rod

lossy dipoles

Dg = 2.25

Dz = 5

2L = 4.26

s = .2

$r_{dip} \sim .025$

TOP VIEW
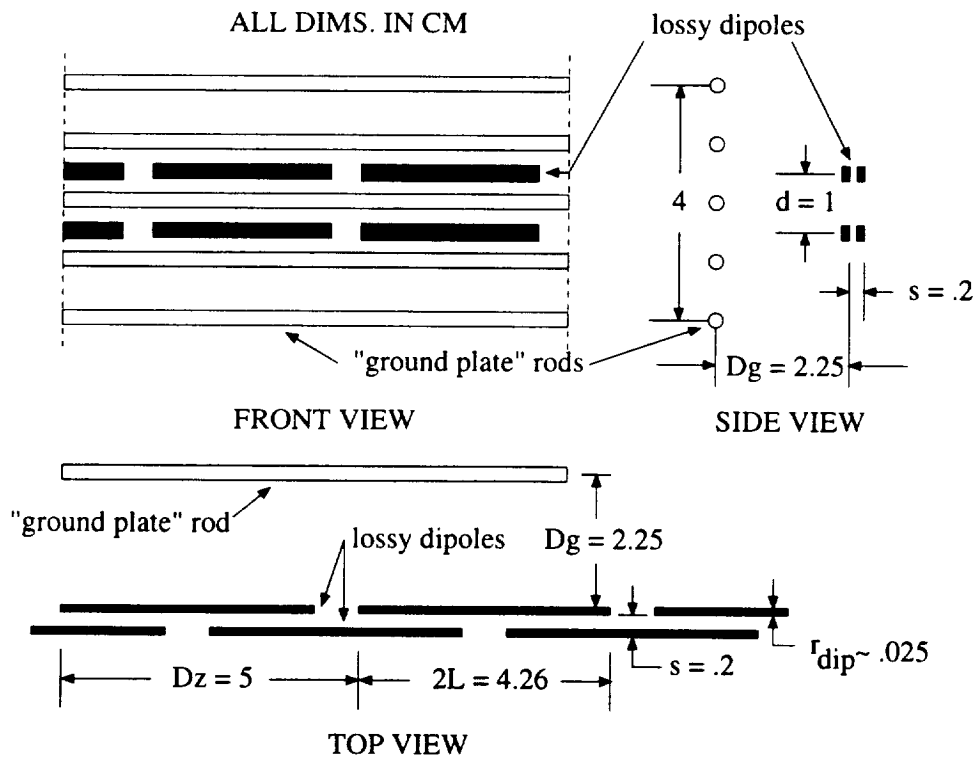
Figure 4.42: Dipole array geometry.

REFERENCE PLOT GEOMETRY

1. rods
   a. radius of rods r_{rod} = .2 cm
   b. length of simulated ground plate d_{gp} = 4 cm

2. dipoles in front of rods
   a. inter-element separation D_z = 5 cm
   b. length of elements 2L = 4.26 cm
   c. radius of elements r_{dip} = .025 cm
   d. resistance of elements R = 100 Ω/cm
   e. offset dipole separation distance s = .2 cm
   f. dipole pair separation distance d = 1 cm
   g. ground plate spacing D_g = 2.25 cm

Figure 4.43: Parameters of dipole array geometry.

starting point, two rectangular rods with the same dimensions and distance from the conducting bulkhead are used. To limit the number of rod location possibilities (and computation time), the center of the rods are constrained to be located a maximum of 10 cm from the bulkhead in the x direction and within ±6.35 cm in the y direction (Figure 4.44). Additionally, the dimensions of the rods are set between 1 and 2 cm in length and height.

Figure 4.44: Location and dimensions of material rods.

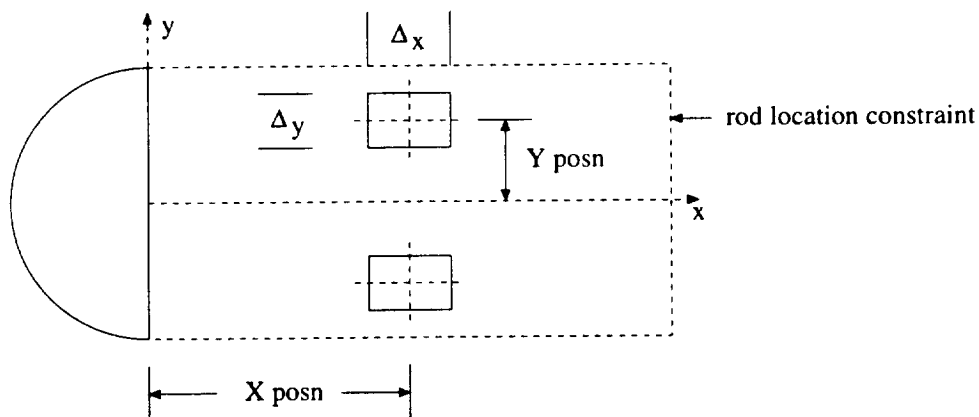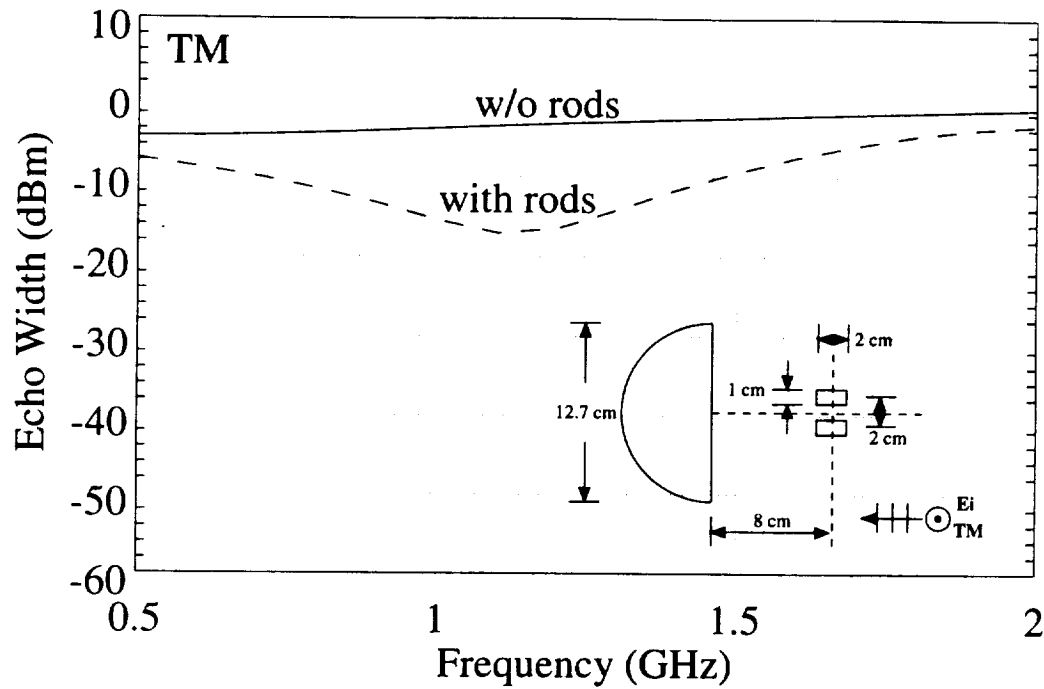Figure 4.45: Backscattered field from planar bulkhead with PEC rods placed in front of bulkhead, TM polarization. Solid - planar bulkhead alone, dashed - planar bulkhead with rods placed at $x_{posn}=8$ cm, $y_{posn}=\pm 1$ cm, with $\Delta_x=2$ cm, and $\Delta_y=1$ cm.

The dimensions of the rods and each rods' $\pm y$ location are held constant while varying the separation distance between the bulkhead and rods. The length, width, or $\pm y$ location of the rods are changed for each scan of separation distance as a means of systematically investigating the effects of each parameter combination. The scattering signature of one of the more desirable responses is shown in Figure 4.45. It is possible that other combinations of parameters (i.e. a greater number or rods, larger rod size, larger separation distance, etc.) exist that are more effective in lowering the scattered field levels at the necessary frequencies.

4.4.3   Lossy Dielectric Rods

TM Polarization

An initial consideration for this technique is the value of the dielectric constant used for the lossy dielectric rods. It is found that better nulling effects are obtained when the loss tangent of the material is large. An inspection of Table 4.1 shows that the
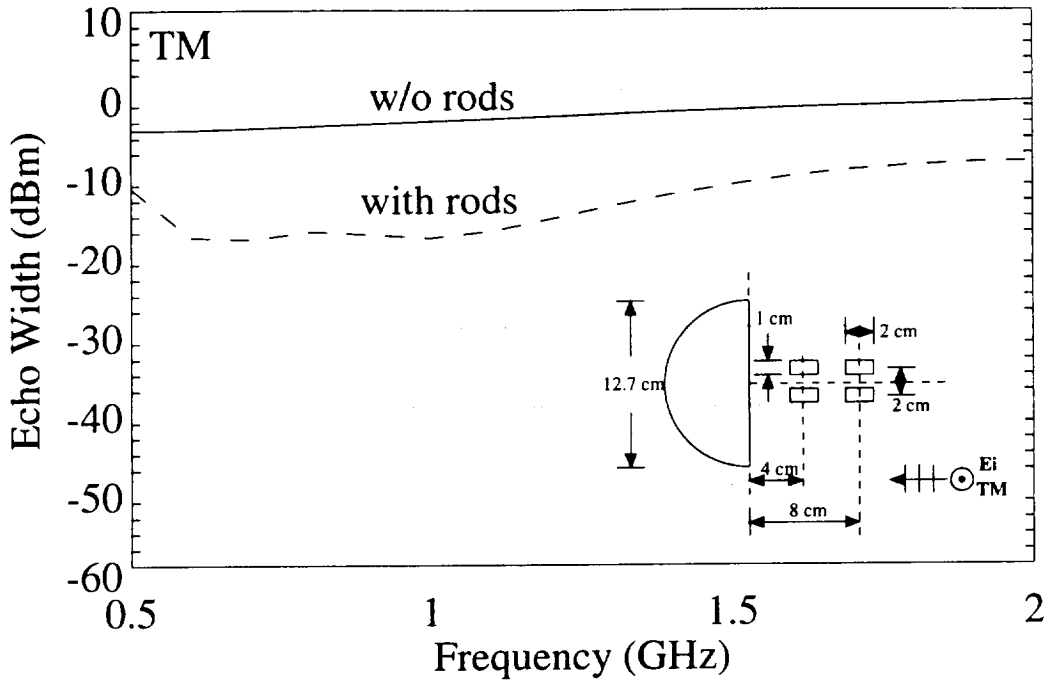
Figure 4.46: Backscattered field from planar bulkhead with four dielectric rods (ϵ_r=23.3-j16.3) placed in front of bulkhead, TM polarization. Planar bulkhead alone - solid; planar bulkhead with rods placed at x_{posn}=4 and 8 cm, y_{posn}=±1 cm, with Δ_x=2 cm, Δ_y=1 cm - dashed.

material under consideration with the largest loss tangent has a relative dielectric constant of ϵ_r=23.3-j16.3.

Using similar methods as described in the previous section to search for optimum rod placement and dimensions combined with results found in [13], a dielectric rod geometry is found that has desirable nulling effects. The scattering signature and dimensions of the geometry are given in Figure 4.46. Note that four dielectric rods are used to achieve the results. The first set of calculations are executed using two rods. Once the dual rod geometry with the best response is found, an additional two rods are added to investigate their effect. It is found that the two additional rods provide greater bandwidth.

For the previous calculations, dielectric rods were considered with relative permeability of μ_r=1. Figure 4.47 shows the effects of using the same configuration of dielectric rods as in Figure 4.46, but with μ_r=4.8-j.4. This value of μ_r is perhaps unrealistic, but it demonstrates that further reduction may be possible by altering
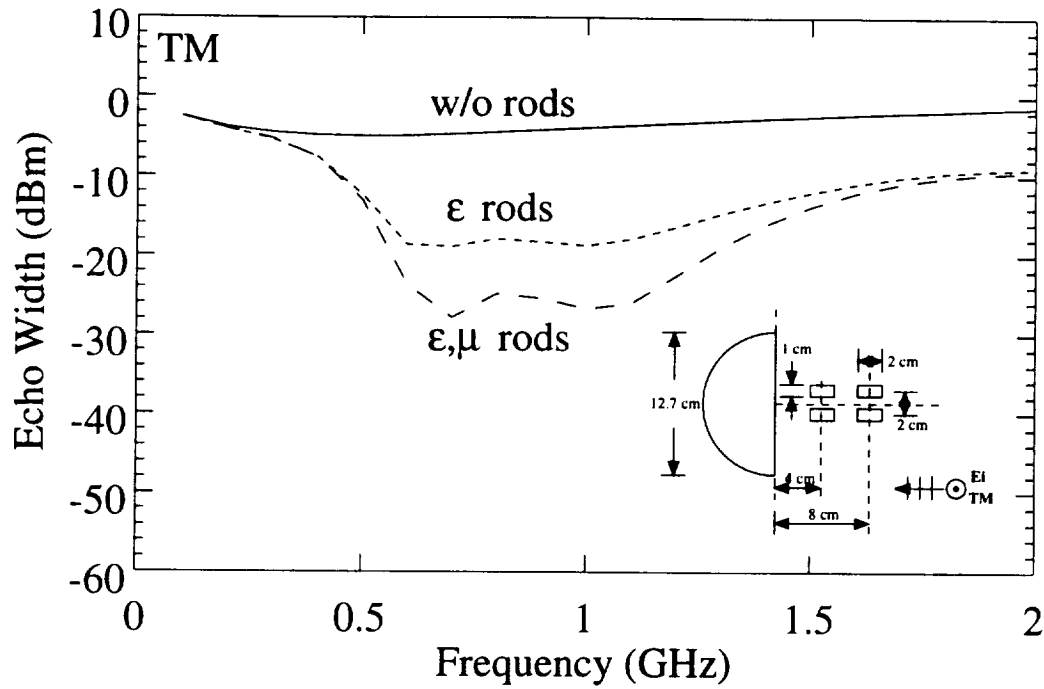
Figure 4.47: Backscattered field from planar bulkhead with four dielectric rods (ϵ_r=23.3-j16.3) placed in front of bulkhead, TM polarization. Planar bulkhead alone - solid; planar bulkhead with dielectric rods, μ_{rods}=1 - short dashed; planar bulkhead with dielectric rods, μ_{rods}=4.8-j.4 - long dashed.

the permeability of the rods. Note that a non-zero μ_r is used with ϵ_r=23.3-j16.3. It is found that varying μ_r with ϵ_r=1 is ineffective for this configuration.

TE Polarization

The desirable four rod configuration found in the previous section for TM polarization did little to reduce backscatter levels when considering TE polarization. Many combinations of the four rod geometry were experimented with by varying the rod dimensions and placement, with negligible effect. Several two rod geometries were also considered, but still did little to influence the scattered field.

Finally, a single material rod geometry was found to be effective. The resulting geometry is shown in Figure 4.48. The dimensions and location of the rod were found using values of ϵ_r=23.3-j16.3 and μ_r=1. Figure 4.49 illustrates the backscatter signature of the geometry, as well as the improvement obtained by changing the relative permeability from μ_r=1 to μ_r=4.8-j.4.
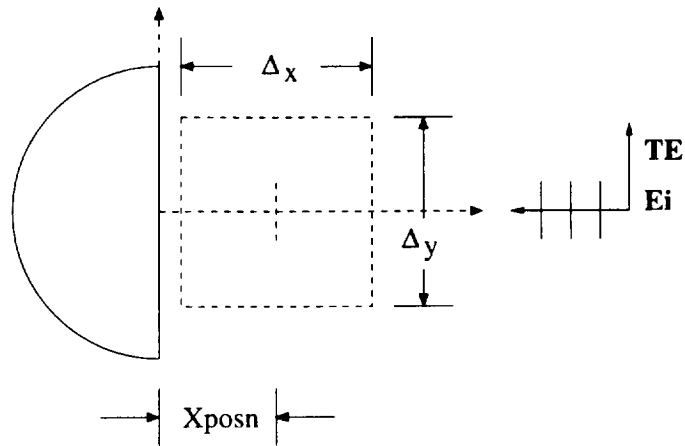
Figure 4.48: Location and dimensions of material rod for TE polarization.

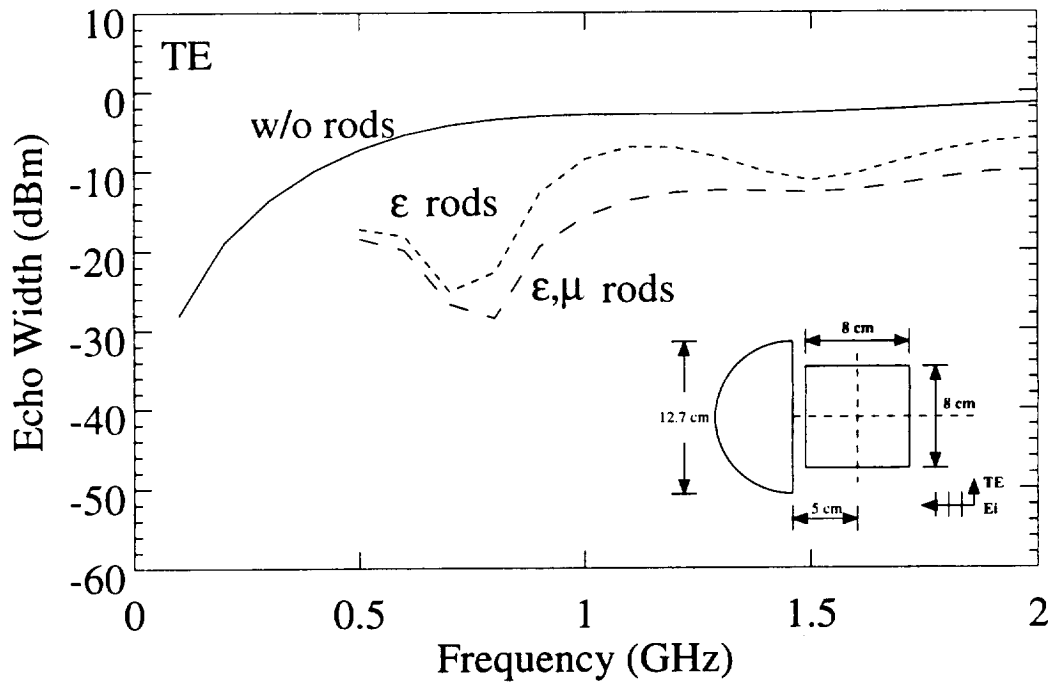Figure 4.49: Backscattered field from planar bulkhead with single dielectric rod (ϵ_r=23.3-j16.3) placed in front of bulkhead, TE polarization: x_{posn}=5 cm, Δ_x=Δ_y=8 cm. Planar bulkhead alone - solid; planar bulkhead with dielectric rod, μ_{rod}=1 - short dashed; planar bulkhead with dielectric rod, μ_{rod}=4.8-j.4 - long dashed.

Chapter 5

Composite Edge Termination Analysis

5.1 Introduction

Building upon the results of the previous chapter, the three planar bulkhead configurations of Figure 5.1 are considered for further analysis.

In the first configuration, internal material loadings are used in combination with resistive cards placed exterior to the dielectric skin. In the second configuration, the conducting bulkhead is shaped along with the use of resistive cards and internal loadings. The last configuration considers the nulling effects of material rods used in the presence of the dielectric skin and resistive cards. Both free space and lossy dielectric materials are considered for use in the region surrounding the material rods.

5.2 Case I: Simple Wedge Geometry

5.2.1 Resistive Cards Placed on Exterior Surface of Dielectric Skin

The geometry studied in this section is described by Case I of Figure 5.1. The relative dielectric constant of the skin is set to $\epsilon_{skin}=6$, with free space in the internal region. The value of the resistive cards external to the dielectric skin are varied from 100 to $500\Omega/\square$, with the signatures of the resulting geometries shown in Figures 5.2 and 5.3 for TM and TE polarization, respectively.
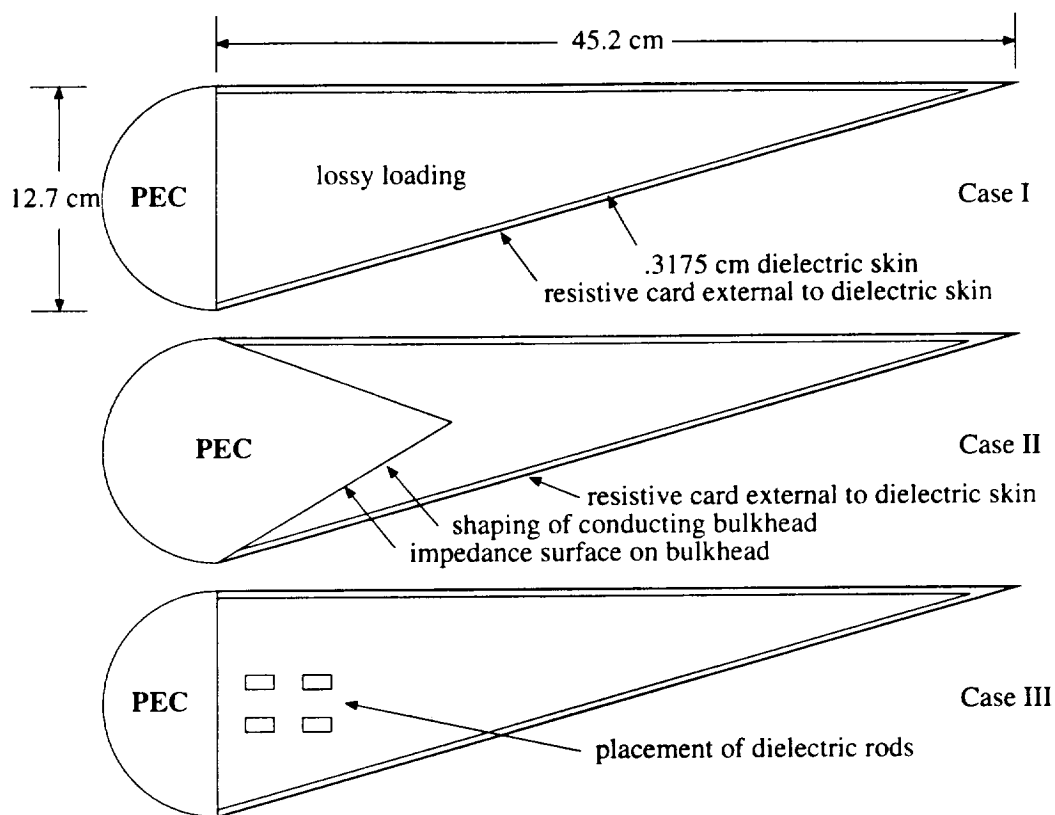
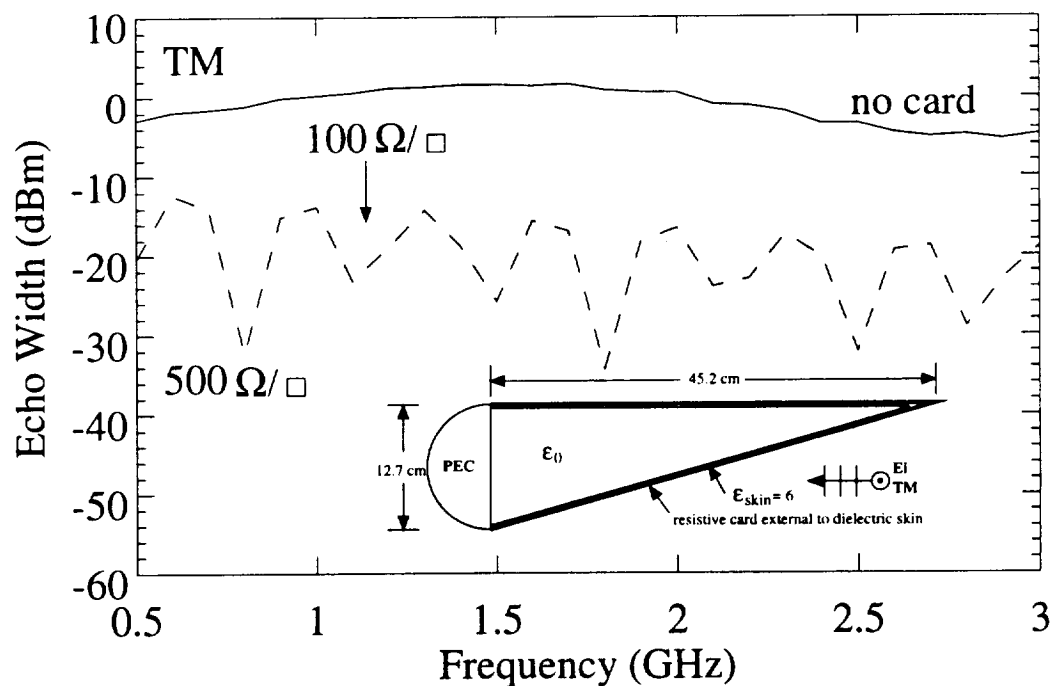Figure 5.1: Final geometries under consideration.

Figure 5.2: Echo widths for simple wedge geometry with resistive card, TM polarization.
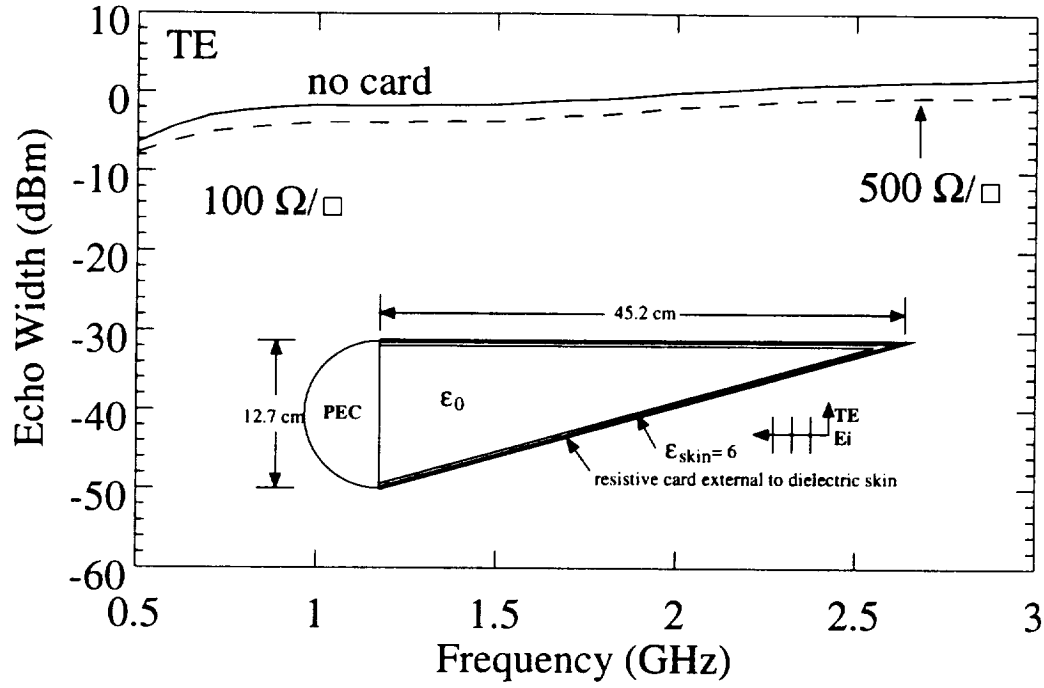
83

Figure 5.3: Echo widths for simple wedge geometry with resistive card, TE polarization.

Only the signatures for resistive card values of 100 and $500\Omega/\square$ are included in the curves for both polarizations, since the variation between $\Omega/\square$ values in this range is minimal. Resistive cards are more effective in reducing scattering levels for this configuration when illuminated with TM polarization. Additionally, the results of Section 4.3.3 help to illustrate this point.

5.2.2 Constant Resistive Card Combined with Various Lossy Internal Loadings

The previous section demonstrated that when considering TM polarization, the performance of a resistive card of $100\Omega/\square$ had similar behavior as a resistive card of $500\Omega/\square$. For TE polarization, the difference in response between the two resistive card values is more dramatic, with the $100\Omega/\square$ card having slightly better performance.

Based upon the results of the previous section, the geometry is altered by using a constant resistive card value of $100\Omega/\square$ while changing the internal region loading in accordance with the various ϵ_r values of Table 4.1.
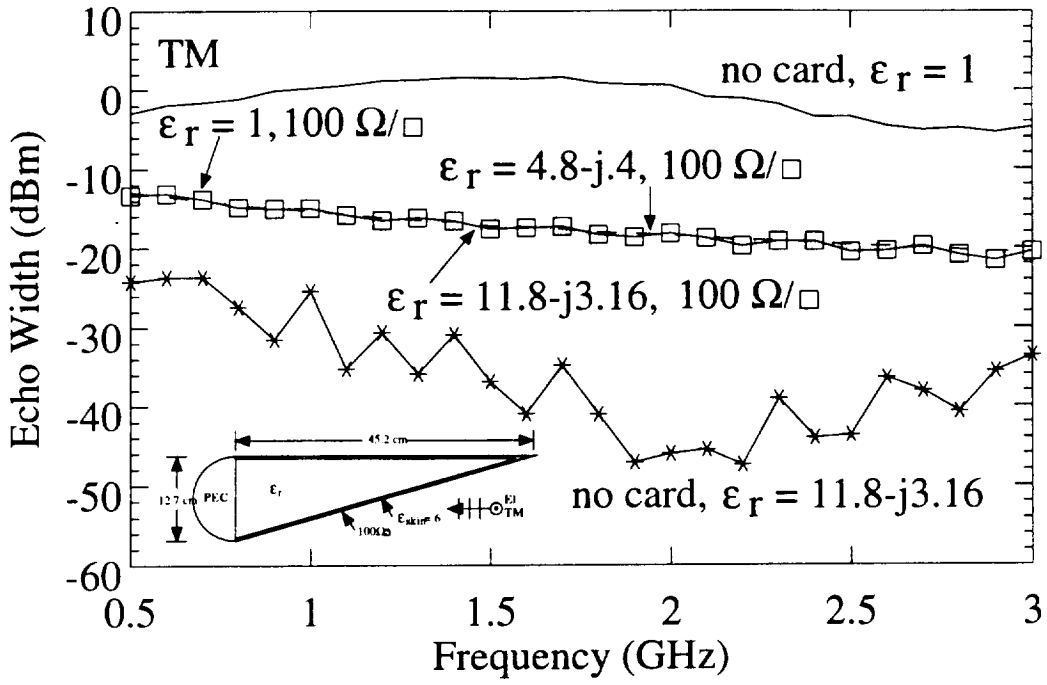
84

Figure 5.4: Echo widths for simple wedge geometry with $100\Omega/\square$ resistive card with internal loading (ϵ_r), TM polarization.

Figures 5.4 and 5.5 give selected results for TM and TE polarization, respectively. For TM polarization, a resistive card placed on the outer surface of the dielectric skin limits the effectiveness of loading the interior region. This point is illustrated in Figure 5.4 by providing the signature corresponding to an interior loading of $\epsilon_r=11.8$-j3.16 without the resistive card in place. For TE polarization, levels can be further reduced by loading the internal region. In addition, using an internal loading of $\epsilon_r=4.8$-j.4 is comparatively as effective as an internal loading of $\epsilon_r=11.8$-j3.16. Thus, an internal loading of $\epsilon_r=4.8$-j.4 will be used for calculations in the next section. Using a value of ϵ_r with smaller magnitude also reduces computation time as less unknowns are required to adequately describe the geometry.

5.2.3 Constant Internal Loading Combined with Various Resistive Card Values

Using the geometry of the previous section with an internal loading of $\epsilon_r=4.8$-j.4 and resistive card values in the range 100 - $500\Omega/\square$ yields the backscatter signatures shown in Figures 5.6 and 5.7 for TM and TE polarization, respectively. There is
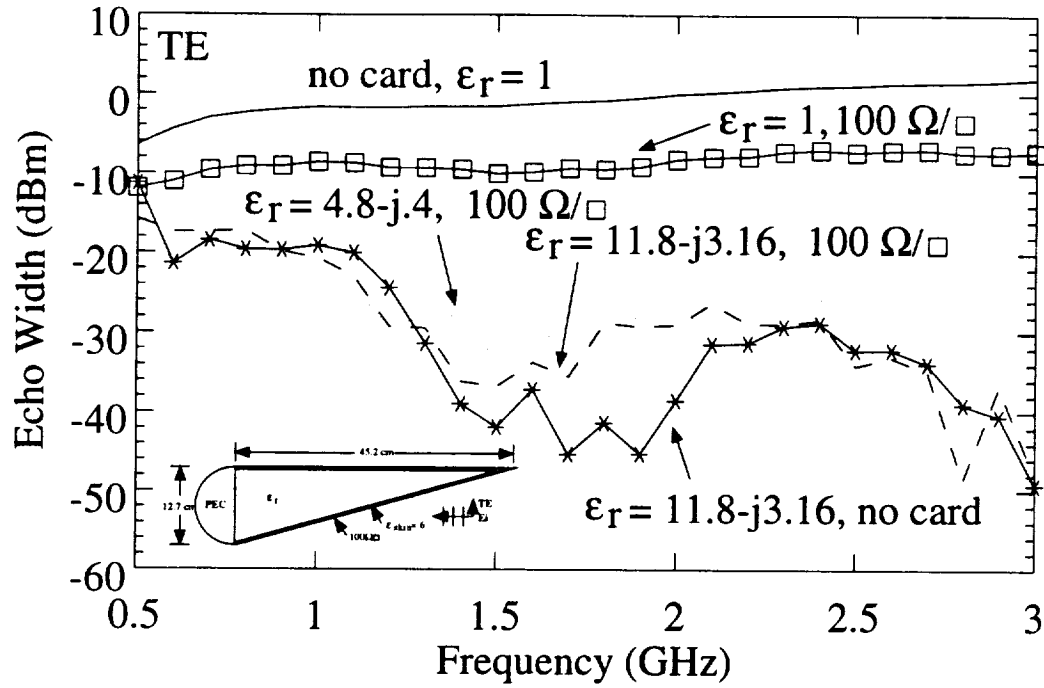
Figure 5.5: Echo widths for simple wedge geometry with $100\Omega/\square$ resistive card with internal loading (ϵ_r), TE polarization.

little deviation in scattering levels between resistive card values in this range with TM polarization. This result again confirms that placement of a resistive card on the external surface of the dielectric skin reduces the effectiveness of the internal loading. For TE polarization, a resistive card value of $200\Omega/\square$ is most effective in the frequency range from .5 to 1 GHz, with a value of $100\Omega/\square$ becoming most effective in the range 1 to 3 GHz.

5.3 Case II: Simple Wedge Geometry with Shaping of Conducting Bulkhead

5.3.1 Resistive Cards Placed on Exterior Surface of Dielectric Skin

The geometry examined in this section is described by Case II of Figure 5.1. The difference from Case I is in the shape of the conducting bulkhead. The front portion of the bulkhead is extended to form a wedge as shown, with the distance from the bulkhead junction set at 25.4 cm. Once again, the relative dielectric constant of
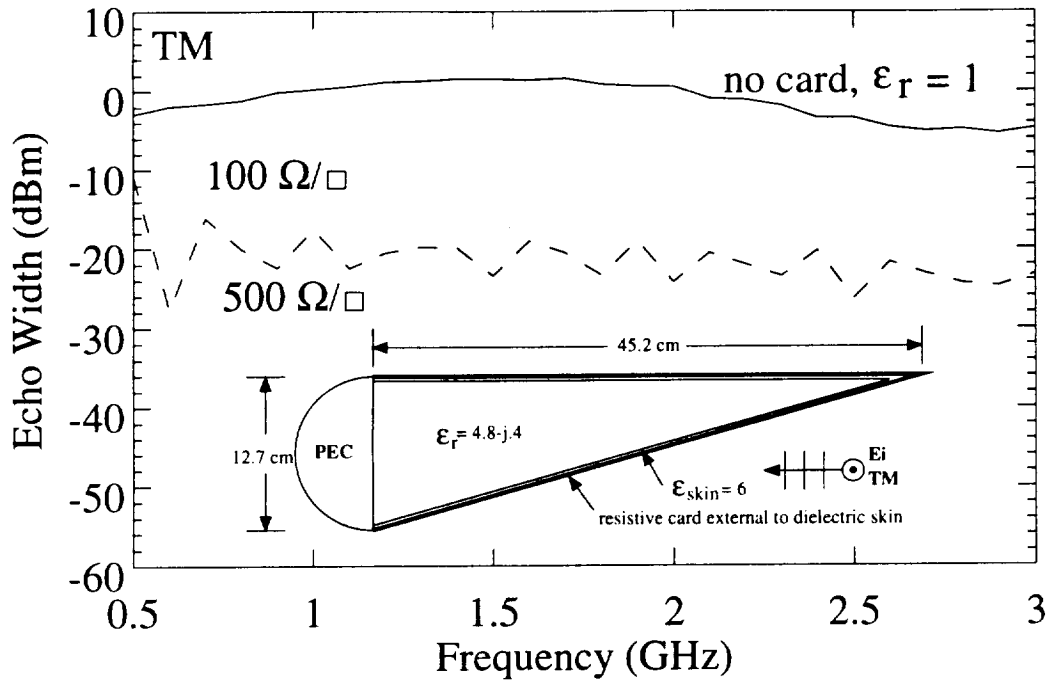
Figure 5.6: Echo widths for simple wedge geometry with resistive card, internal loading ϵ_r=4.8-j.4, TM polarization.

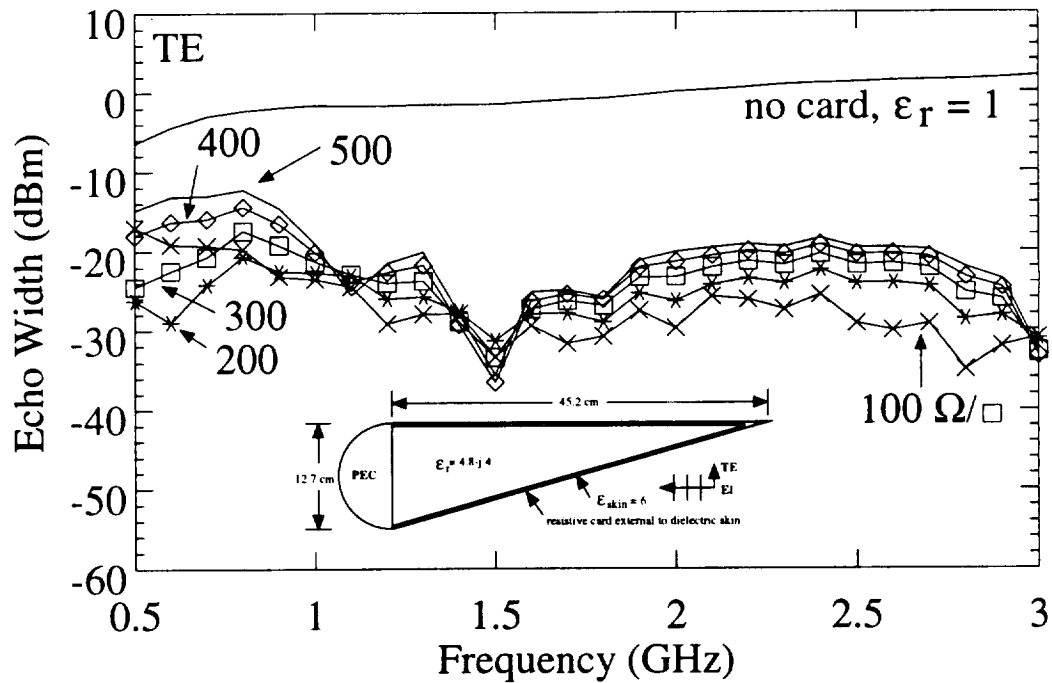
Figure 5.7: Echo widths for simple wedge geometry with resistive card, internal loading ϵ_r=4.8-j.4, TE polarization.
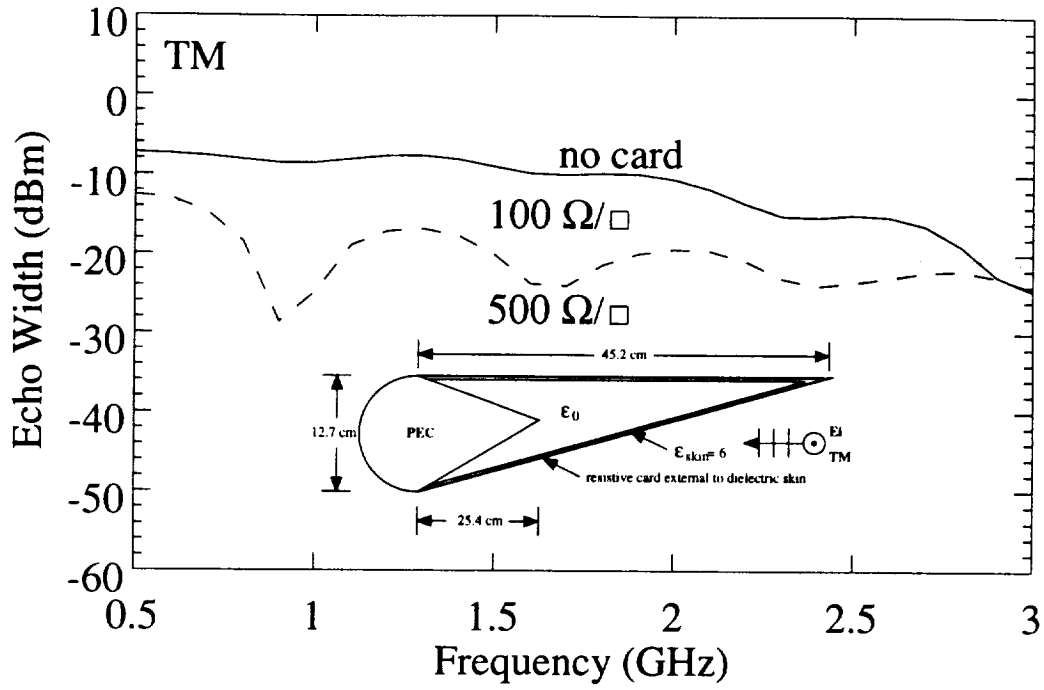
Figure 5.8: Echo widths for shaped conducting bulkhead geometry with resistive card, TM polarization.

the skin is set to $\epsilon_{skin}=6$, with free space in the internal region. The value of the resistive cards external to the dielectric skin are varied from 100 to $500\Omega/\square$, with the signatures of the resulting geometries shown in Figures 5.8 and 5.9 for TM and TE polarization, respectively.

For TE polarization, resistive cards in the specified range are largely ineffective when used in conjunction with a wedge shaped conducting bulkhead. For TM polarization, resistive cards help reduce scattering levels at low frequencies, with only slight signature variation between card values.

5.3.2 Constant Resistive Card Combined with Various Lossy Internal Loadings

The results of the previous section demonstrate that there is little difference in scattering signatures between resistive card values. The calculations performed in this section utilize a resistive card of $100\Omega/\square$ while varying the internal region loading. The results for TM and TE polarizations are given in Figures 5.10 and 5.11, respectively.
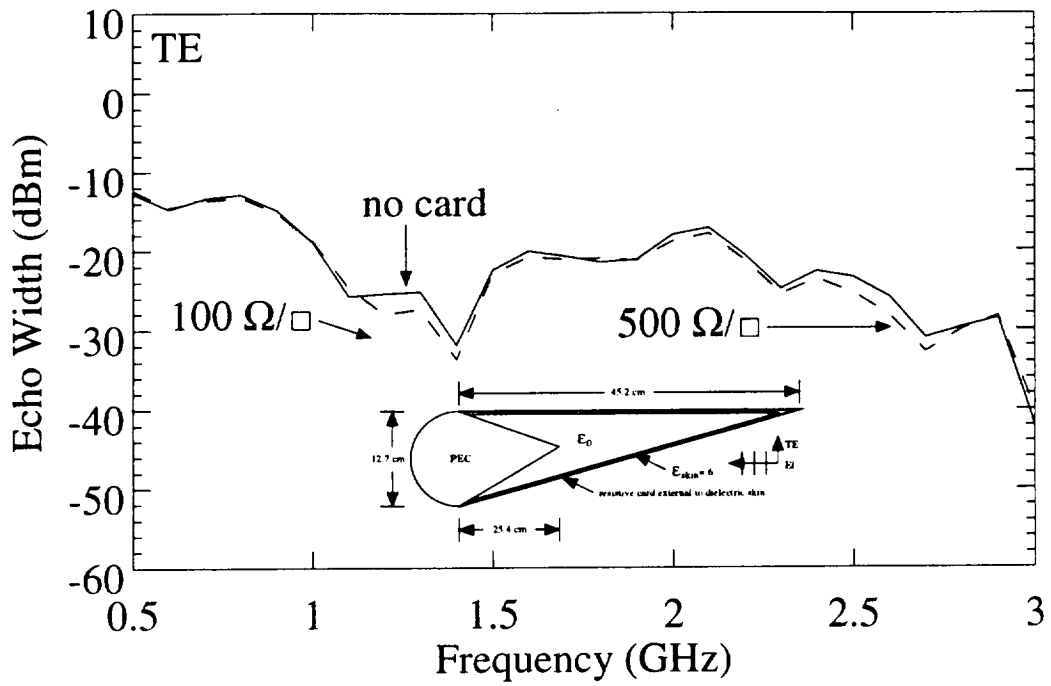
Figure 5.9: Echo widths for shaped conducting bulkhead geometry with resistive card, TE polarization.
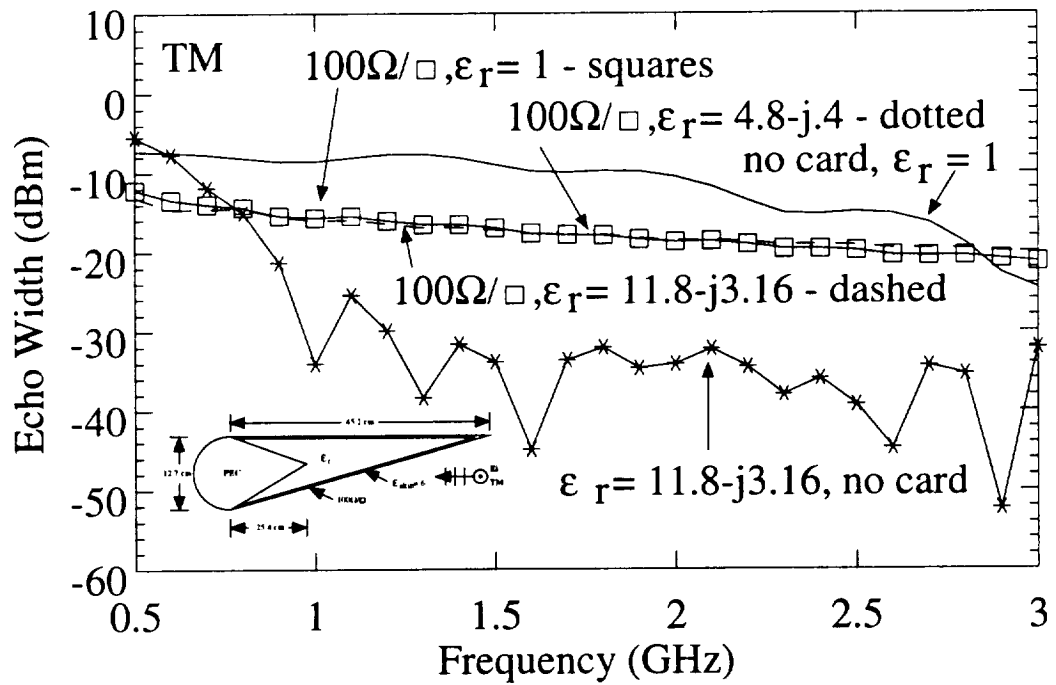

Figure 5.10: Echo widths for shaped conducting bulkhead geometry with $100\Omega/\square$ resistive card, TM polarization.
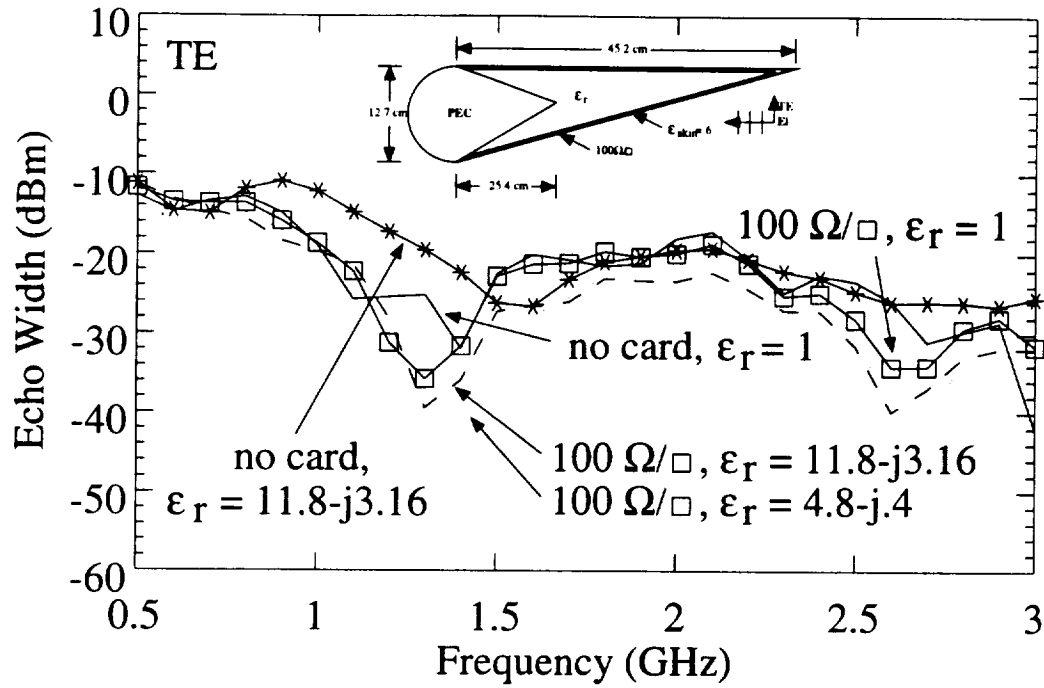
Figure 5.11: Echo widths for shaped conducting bulkhead geometry with $100\Omega/\square$ resistive card, TE polarization.

As was found for Case I, a resistive card placed on the outer surface of the dielectric skin limits the effectiveness of loading the interior region when considering TM polarization. There is, however, a small deviation between the TE signatures of the bulkheads in Cases I and II when considering a constant resistive card of $100\Omega/\square$ with various internal region loadings.

In Case I (TE), loading the interior region is effective in further influencing the backscattered fields when used in conjunction with a resistive card on the external surface of the dielectric skin. In contrast, loading the interior region of the geometry of Case II (TE) does not have as dramatic of an effect. A possible explanation for this behavior is that the wedge shaped bulkhead alone already provides significant reduction when compared to the signature of the planar bulkhead alone.

5.3.3 Impenetrable Impedance Bulkhead

Section 4.3.3 investigates the effects of placing an impedance surface on the flat portion of the planar conducting bulkhead. Applying the same concept to the wedge shaped portion of the conducting bulkhead and considering only the bulkhead in free
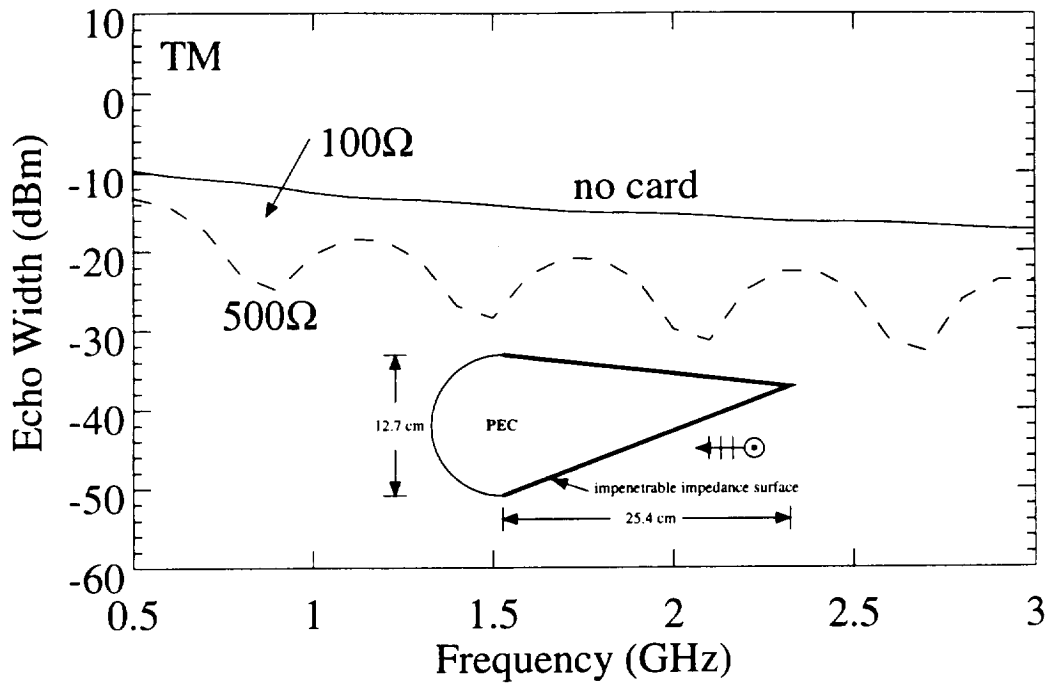
90

Figure 5.12: Echo widths for wedge shaped bulkhead with impenetrable impedance surface on wedge portion of bulkhead, TM polarization.

space yields the results shown in Figures 5.12 and 5.13 for TM and TE polarization, respectively. The bulkhead is considered in absence of the dielectric skin to illustrate that it is the shape of the bulkhead that limits the effectiveness of the impedance surface for both polarizations.

5.4 Case III: Simple Wedge Geometry with Placement of Dielectric Rods

5.4.1 Dielectric Rod Placement Analysis

This section builds upon the dielectric rod geometry of Figure 4.46 in Section 4.4.3. The difference between the geometry of Section 4.4.3 and the current geometry is that the bulkhead and rods are now considered in the presence of the dielectric skin, as shown in Figure 5.15.

In deciding what material should be used for the rods, swept frequency calculations are run for rod relative dielectric constants of Table 4.1. The results are shown in Figure 5.14 for TM polarization. Also included is a calculation using PEC
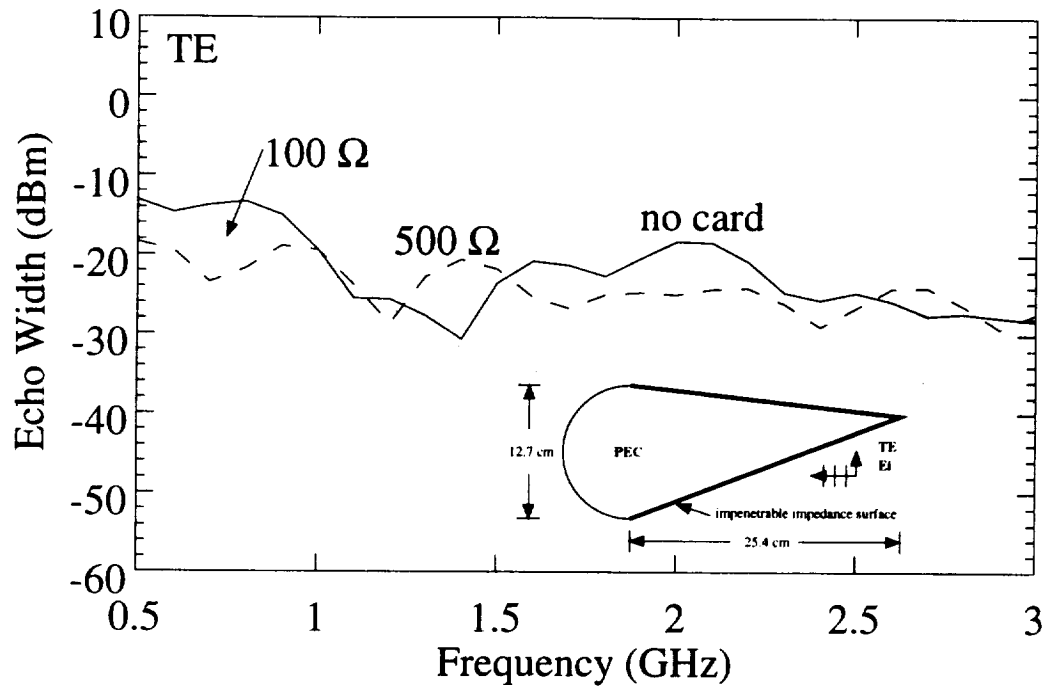
91

Figure 5.13: Echo widths for wedge shaped bulkhead with impenetrable impedance surface on wedge portion of bulkhead, TE polarization.

rods in place of lossy dielectric rods. The results illustrate that using dielectric rods with a high loss tangent (ϵ_r=23.3-j16.3) is more effective in reducing low frequency backscatter than using PEC rods.

The GA is applied to search for an optimum combination of X1, X2, and Y_{sep} (as shown in Figure 5.15) with discretizations given by the GA template file of Figure 5.16. The search is performed using three different fitness functionals corresponding to TM echo width at .5, .7, or 1 GHz.

The best results for the three GA runs are summarized in Tables 5.1 through 5.3. The signature for each of the three search cases have varying performance as shown in Figures 5.17 through 5.19.

As a means of lowering the TE return without largely affecting the TM return, a 500Ω impedance is applied to the flat portion of the conducting bulkhead with the resulting signatures shown in Figures 5.20 through 5.22. Unfortunately, as was noted in Section 4.3.2, this impedance surface may not be realistic.
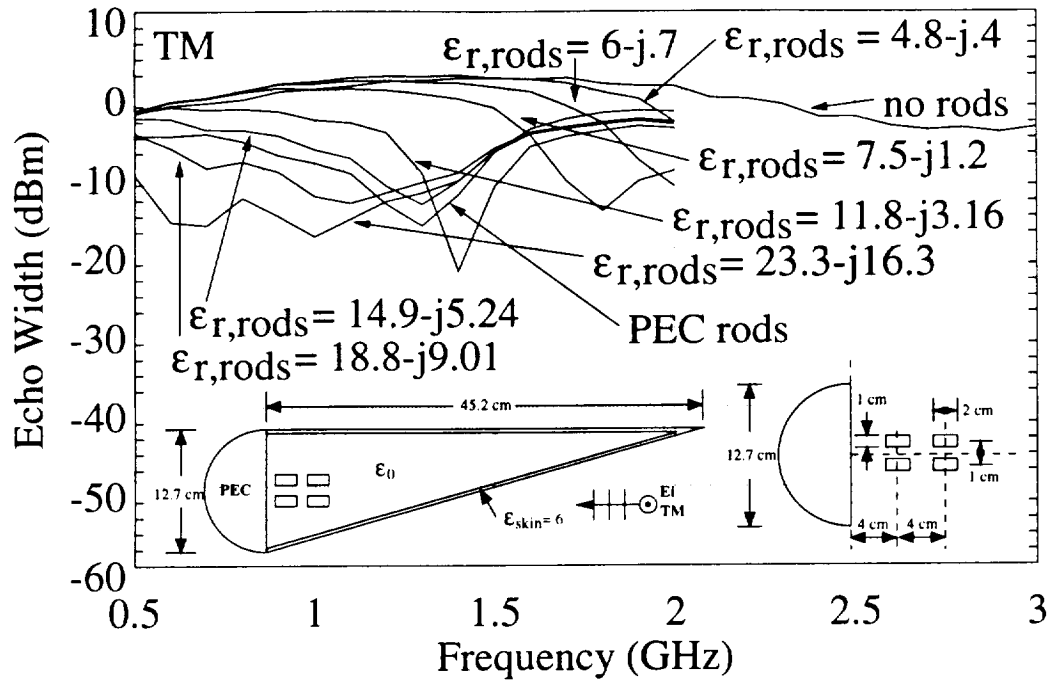
Figure 5.14: Echo widths for planar bulkhead with skin geometry with placement of dielectric rods.
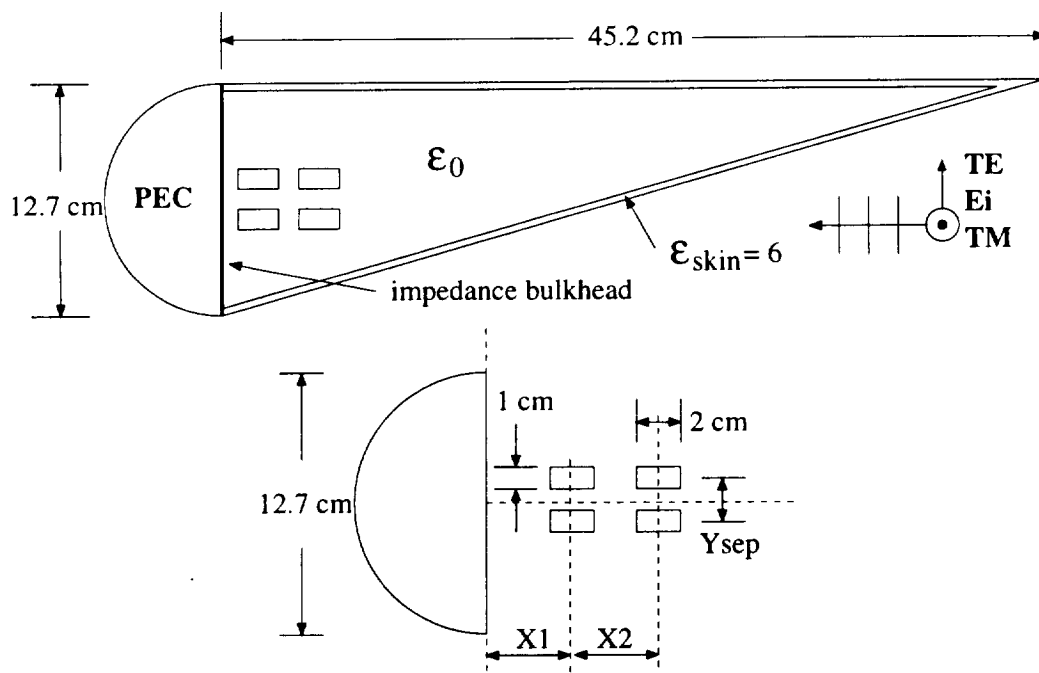

Figure 5.15: Planar bulkhead geometry with placement of material rods in presence of dielectric skin.

```
genes: 3

gene 0
min: 2
max: 5.75
values: 16
format: %9.3f

gene 1
min: 3
max: 6.75
values: 16
format: %9.3f

gene 2
min: 1
max: 4.75
values: 16
format: %9.3f
```

Figure 5.16: "template" file corresponding to the search for optimum dielectric rod placement.

Table 5.1: Search results for optimum combination of X1, X2, and Y_{sep} with Echo Width evaluated at .5 GHz, TM polarization.

X1 (cm)	X2 (cm)	Y_{sep} (cm)	Echo Width (dBm)	Generation	trial
4.500	3.000	1.000	-1.3004e+01	6	168
5.750	3.000	1.250	-1.2588e+01	15	262
5.250	3.000	1.000	-1.2926e+01	2	79
4.750	3.000	1.000	-1.2827e+01	8	193
5.500	3.250	1.000	-1.2912e+01	9	205
5.750	3.250	1.000	-1.2954e+01	10	221
5.500	3.000	1.000	-1.3218e+01	3	106
5.750	3.000	1.000	-1.3510e+01	2	84
4.500	3.250	1.000	-1.2637e+01	11	239
5.000	3.000	1.000	-1.2730e+01	1	61

Table 5.2: Search results for optimum combination of X1, X2, and Y_{sep} with Echo Width evaluated at .7 GHz, TM polarization.

X1 (cm)	X2 (cm)	Y_{sep} (cm)	Echo Width (dBm)	Generation	trial
2.500	3.250	1.250	-3.2803e+01	0	17
2.500	3.000	1.500	-3.0087e+01	5	147
2.250	3.500	1.500	-3.4257e+01	13	220
2.750	3.000	1.500	-3.8261e+01	12	211
2.500	3.500	1.250	-3.8599e+01	3	102
2.750	3.250	1.500	-3.0989e+01	0	43
2.750	3.250	1.250	-3.2524e+01	4	144
2.250	3.500	1.250	-3.1964e+01	12	209
2.500	3.500	1.000	-3.0920e+01	2	94
2.500	3.250	1.500	-3.4025e+01	1	62

Table 5.3: Search results for optimum combination of X1, X2, and Y_{sep} with Echo Width evaluated at 1 GHz, TM polarization.

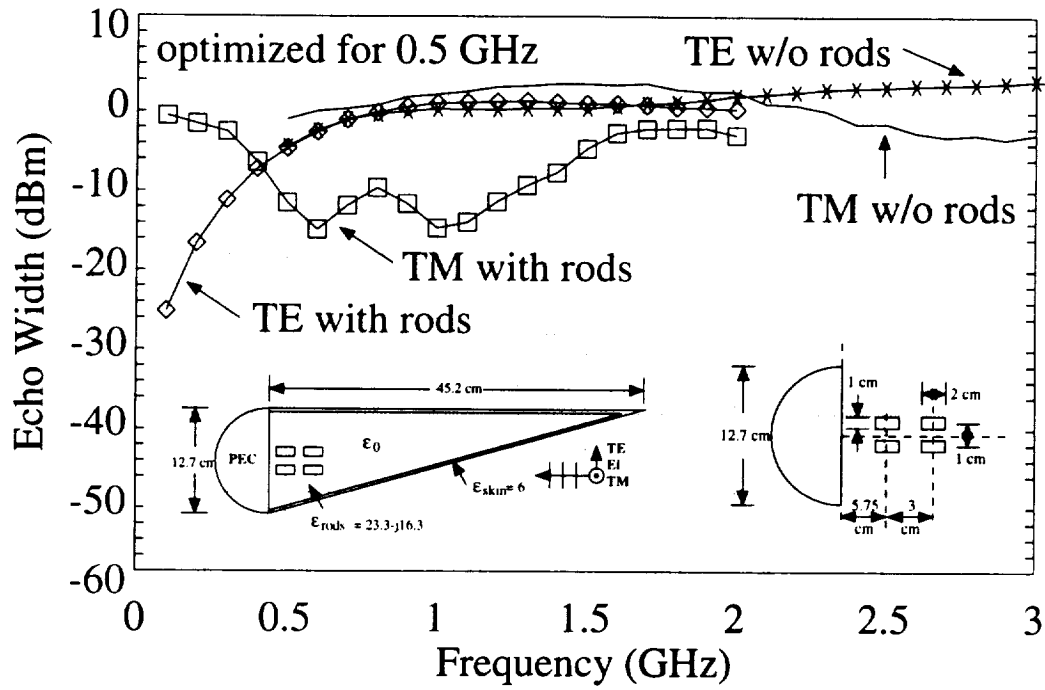| X1 (cm)	X2 (cm)	Y_{sep} (cm)	Echo Width (dBm)	Generation	trial
4.750	3.500	1.000	-1.8635e+01	10	241
4.500	3.750	1.000	-1.9272e+01	9	238
4.750	3.250	1.000	-1.8313e+01	3	109
3.500	4.000	1.000	-1.8340e+01	20	400
4.250	3.750	1.000	-1.8898e+01	12	281
3.750	4.000	1.000	-1.8575e+01	17	358
4.500	3.500	1.000	-1.9361e+01	12	286
4.000	3.750	1.000	-1.8373e+01	5	142
4.250	4.000	1.000	-1.8442e+01	20	387
4.000	4.000	1.000	-1.8476e+01	4	114

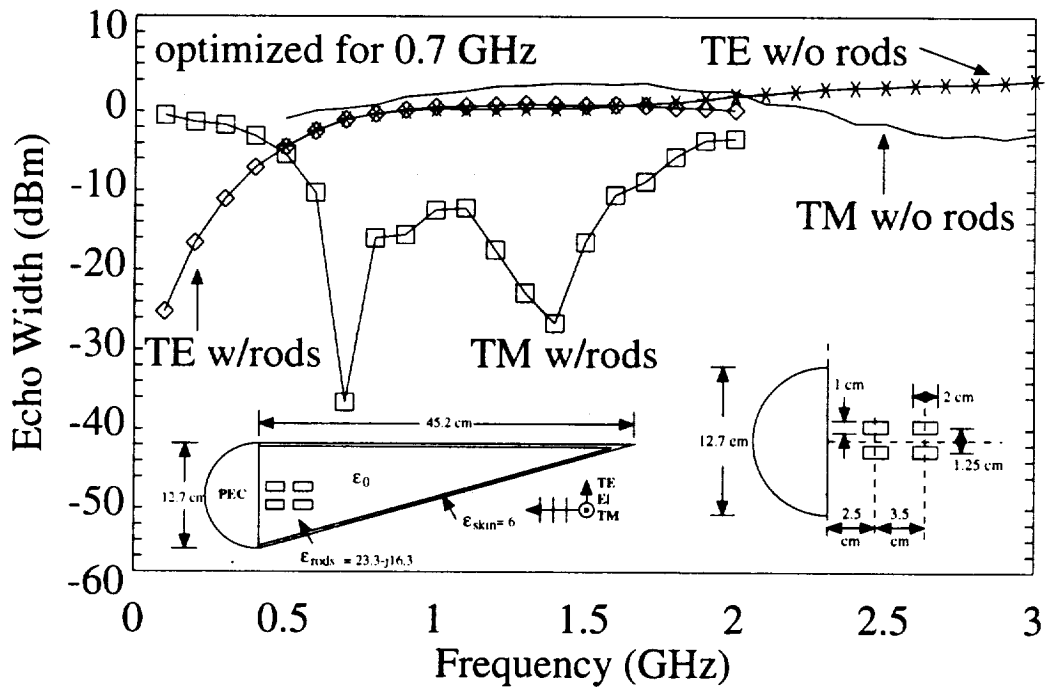Figure 5.17: Echo Widths for dielectric rod geometry optimized to 0.5 GHz.

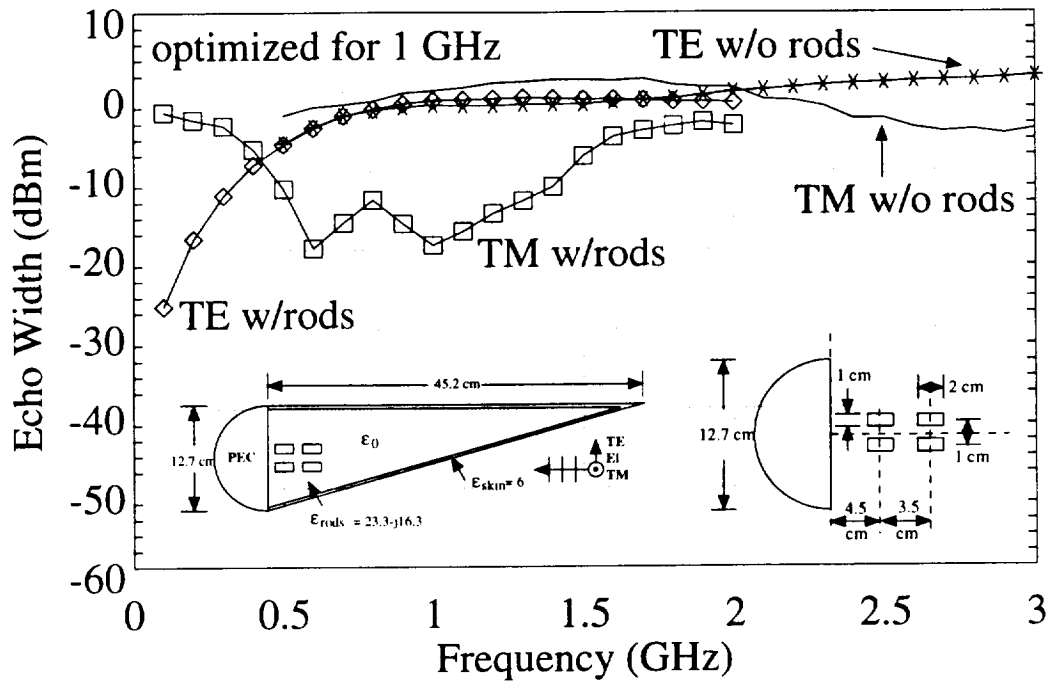Figure 5.18: Echo Widths for dielectric rod geometry optimized to 0.7 GHz.

Figure 5.19: Echo Widths for dielectric rod geometry optimized to 1.0 GHz.
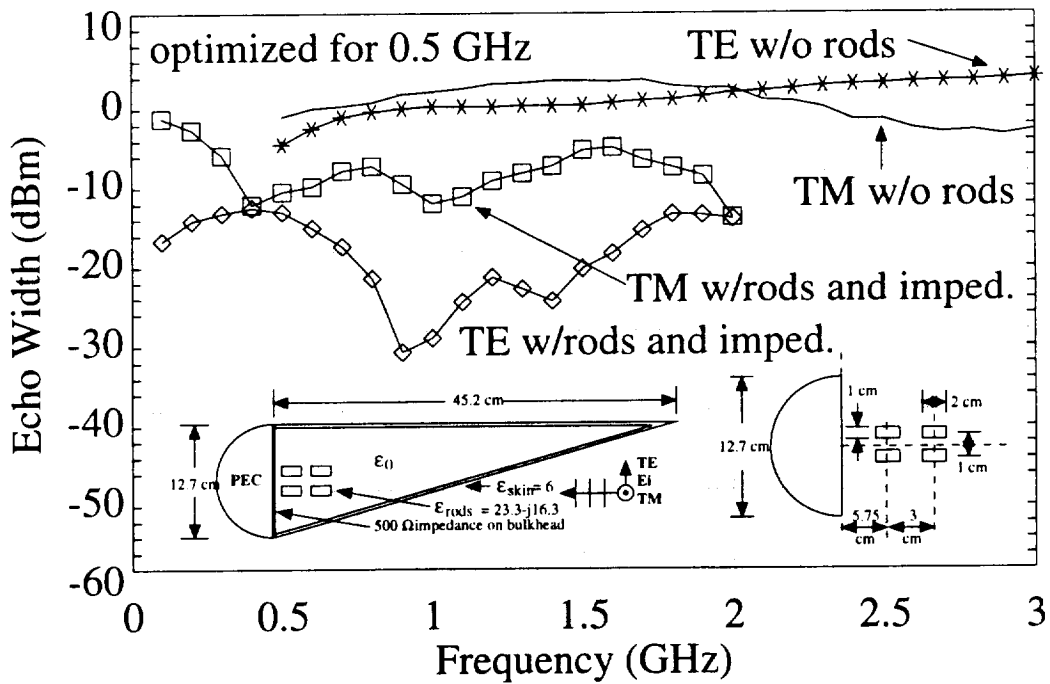

Figure 5.20: Echo Widths for dielectric rod geometry optimized to 0.5 GHz, with a 500Ω impedance placed on the flat portion of the conducting bulkhead.

Figure 5.21: Echo Widths for dielectric rod geometry optimized to 0.7 GHz, with a 500Ω impedance placed on the flat portion of the conducting bulkhead.
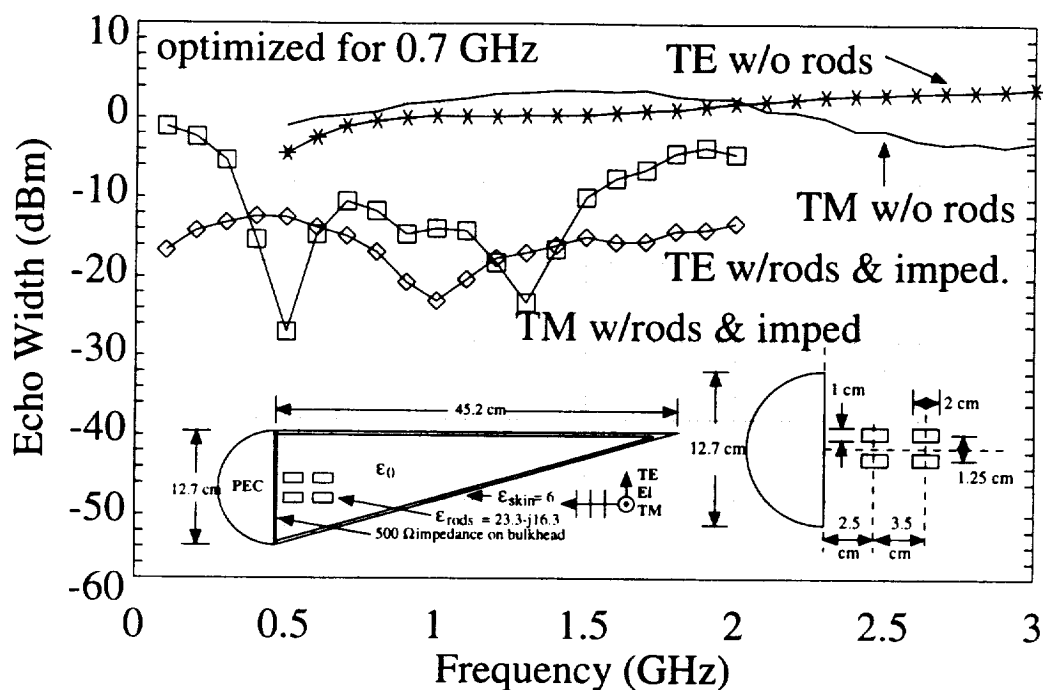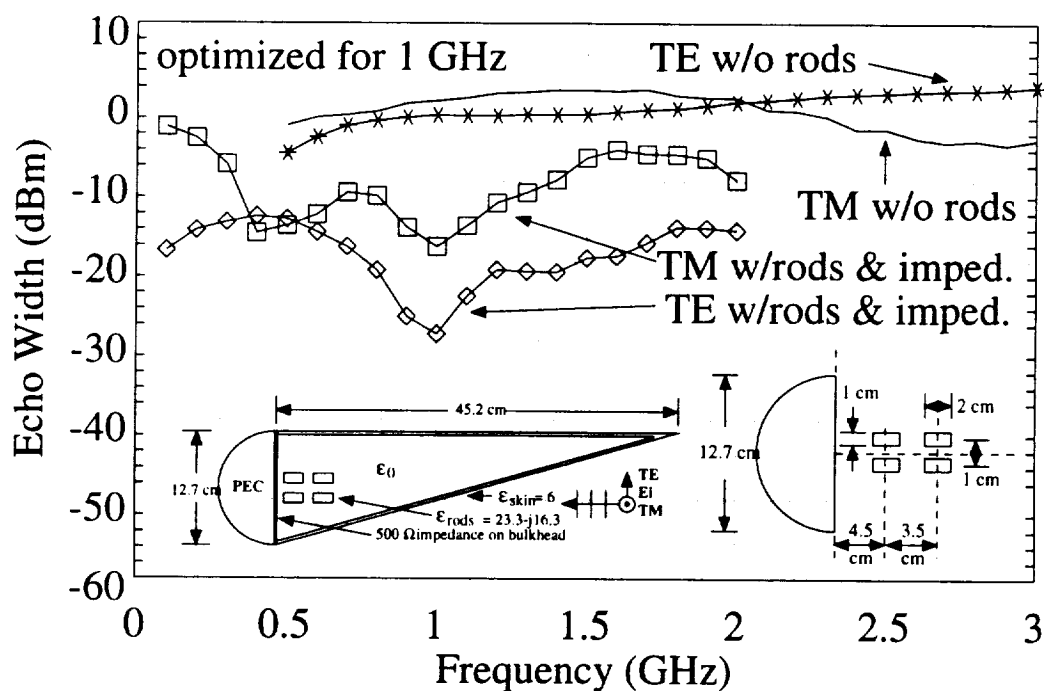

Figure 5.22: Echo Widths for dielectric rod geometry optimized to 1.0 GHz, with a 500Ω impedance placed on the flat portion of the conducting bulkhead.

5.4.2 Variation of Surrounding Dielectric Material

This section illustrates the effects of loading the (internal) region surrounding the dielectric rods with various lossy dielectric materials of Table 4.1. Figures 5.23 and 5.24 give the results for TM and TE polarization, respectively. The backscatter characteristics of the resulting geometry are similar to the performance obtained when loading the internal region with a homogeneous lossy dielectric material as described in Section 4.3.2.

Figure 5.23: Echo Widths for dielectric rod geometry, with various dielectric materials surrounding the rods. $\epsilon_{r,rods}=23.3\text{-}j3.16$, TM polarization.
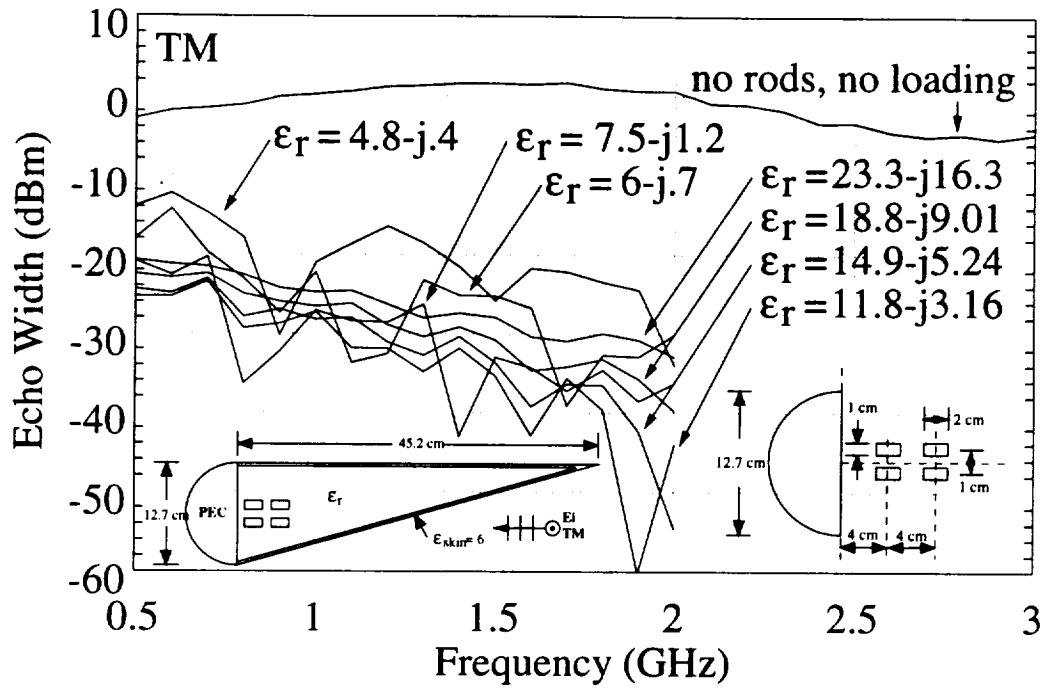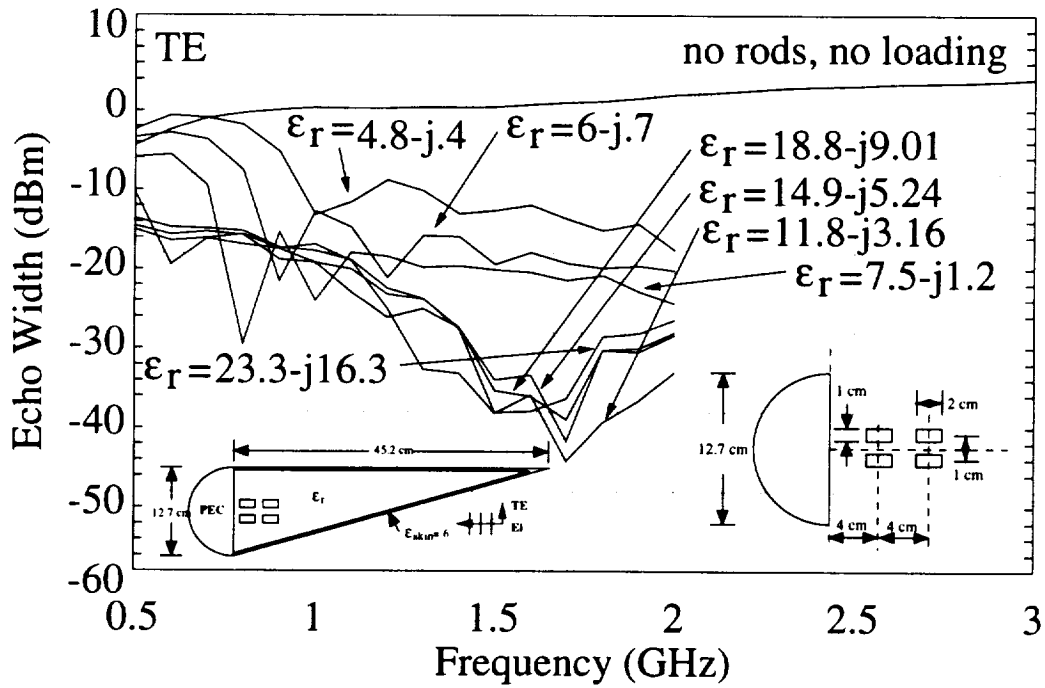

Figure 5.24: Echo Widths for dielectric rod geometry, with various dielectric materials surrounding the rods. $\epsilon_{r,rods}=23.3\text{-}j3.16$, TE polarization.

Chapter 6

Conclusions

In this report, a variety of edge termination methods were studied. It was found that the planar bulkhead with skin geometry has the most desirable backscatter characteristics for both polarizations provided the internal region is loaded with a sufficiently lossy dielectric material as shown in Figures 4.31 and 4.32. Placement of material rods also has desirable backscatter reduction characteristics for both polarizations if a surface impedance can be placed on the flat portion of the planar conducting bulkhead, as shown in Figures 5.20 through 5.22.

A method that did not work for both polarizations is the use of resistive cards. Resistive cards on the external surface of the dielectric skin were found to be an undesirable scattering reduction method since the presence of the card limits the effectiveness of loading the internal region for TM incidence as shown in Figure 5.4. Also, shaping of the internal conducting bulkhead reduced (TE) scattering from the tip and bulkhead junction, but did little to lower the overall backscatter levels of the bulkhead.

Bibliography

[1] M. Kragalott, "Method of Moments Solution for TM Scattering by a General Cylinder", The Ohio State University, Department of Electrical Engineering, M.S. Thesis, August, 1988.

[2] R. Andre, A. Dominek, J. Munk, and N. Wang, "A FEM/BEM Computer Code for Scattering Calculations of Lossy Composite Terminating Structures", Report No. 723224-4, ElectroScience Laboratory, The Ohio State University, December 1991.

[3] J.H. Holland, "Adaption in Natural and Artificial Systems", Ann Arbor: The University of Michigan Press.

[4] J. Grefenstette, "Genesis," Computer software, 1990.

[5] Watson, D.F., "Computing the n-Dimensional Delaunay Triangulation with Applications to Voronoi Polytopes", The Computer Journal, 24(2), 167 (1981).

[6] Sloan, S.W. and Houlsby, G. T., "An Implementation of Watson's Algorithm for Computing 2-Dimensional Delaunay Triangulations", Adv. Eng. Software, 4, 192-197 (1984).

[7] S.H. Lo, "A New Mesh Generation Scheme for Arbitrary Planar Domains", Int. J. Numer. Methods Eng., 21, 1403-1426 (1985).

[8] J. Peiro, J. Peraire, and K. Morgan, "FELISA System Version 1.1 Reference Manual", January 1995.

[9] D. Goldberg, "Genetic Algorithms in Search, Optimization and Machine Learning," Addison-Wesley Publishing Company, Inc., Reading Massachusetts, 1989.

[10] J. Grefenstette, "A User's Guide to GENESIS, Version 5.0", October 1990.

[11] C. Balanis, "Advanced Engineering Electromagnetics," John Wiley & Sons, New York, 1989.

[12] A. Dominek, B. Gray, B. Munk, and N. Wang, "Low Frequency Scattering Reduction Techniques using Nulling", Report No. 723224-17, ElectroScience Laboratory, The Ohio State University, June 1995.

[13] B. Munk and S. Schneider, "On Edge Absorbers in General,", Report No. 724988-1, ElectroScience Laboratory, The Ohio State University, October 1992.

731507-2, "A Numerical Analysis of Electromagnetic Scattering from Two-Dimensional Edge Terminations," Gray, Dominek and Wang, 12/95